



An atomistic view point of the chemical reactivity of modified carbon materials

José Luis Nuñez

A thesis presented for the joint Ph.D. degrees of:

Doctor en Química (Universidad Nacional del Litoral, Argentina)

Doctor of Sciences (Vrije Universiteit Brussel, Belgium)

Promotors:

Prof. Dr. Paola Quaino	–	Facultad de Ingeniería Química Universidad Nacional del Litoral Argentina
Prof. Dr. Frederik Tielens	–	Faculty of Sciences and Bioengineering Sciences Vrije Universiteit Brussel Belgium

Jury:

Prof. Dr. Mercedes Alonso Giner
Prof. Dr. Frank de Proft
Prof. Dr. Pablo Guillermo Bolcatto
Prof. Dr. Alfredo Juan

Abstract (in English)

One of the ways to achieve a reduction in the use of high-cost catalysts is through the synthesis of new compounds with low proportions of these catalysts, which maintain or enhance their desirable characteristics. Conversely, carbonaceous materials offer large surface areas with diverse geometries and compositions that can serve as supports at a significantly reduced cost. However, a better understanding of the synthesis conditions of these systems is still required in order to control their preparation and characteristics and, in particular, the changes in their catalytic properties that may arise from the synergistic effect of the combination of these materials.

This thesis aims to address theoretical studies that provide insight into the behavior of carbonaceous materials modified with nanoparticles of a metal or oxide in different structural configurations and compositions. The objective is to develop a comprehensive understanding of how changes in the material properties after modification impact water adsorption and dissociation. Based on these findings, the goal is to establish a solid foundation for the design of new materials with enhanced performance for the studied processes. For this matter, a series of chemical models of hybrid materials have been suggested and investigated through the use of *ab-initio* methods. In particular, two forms of carbon surfaces, namely carbon nanotubes (CNT) and graphene oxide (GO), have been proposed as substrates for the deposition of different platinum and iridium oxide nanoparticles.

As a result of this investigation, it is found that the proposed carbon surfaces can stabilize platinum (Pt_n , $n = 1 - 10, 13$) and stoichiometric iridium oxide ($(\text{IrO}_2)_n$, $n = 1 - 6$) nanoparticles. The small diameter of the CNT clearly limits the interaction area between the particles and the carbon surface. Moreover, iridium oxide "core-shell-like" structures are found to be more suitable for interacting with polar surfaces as that of the GO. Furthermore, water adsorption and further dissociation were analyzed on selected Pt_n/CNT and $(\text{IrO}_2)_n/\text{CNT}$ systems. Both types of systems presented outstanding results regarding activation energies for the dissociation step. The results of this study encourage experimentalists to synthesize stable triangular-shaped Pt nanoparticles and nanoscaled iridium oxide particles on a CNT surface to promote polarization and increase the efficiency of catalysis.

Lastly, this thesis further examines M_{13} monometallic nanoparticles and their reactivity (by using simple molecules, such as O_2 and N_2), with the aim of developing a comparable analysis for M_{13} clusters on carbon-based surfaces in the future.

Abstract (in Nederlands)

Een van de manieren om het gebruik van dure katalysatoren te verminderen is de synthese van nieuwe verbindingen met een laag aandeel van deze katalysatoren, die hun gewenste eigenschappen behouden of verbeteren. Omgekeerd bieden koolstofhoudende materialen grote oppervlakken met diverse geometrieën en samenstellingen die als drager kunnen dienen tegen aanzienlijk lagere kosten. Een beter begrip van de synthesecondities van deze systemen is echter nog steeds nodig om hun bereiding en eigenschappen te controleren en, in het bijzonder, de veranderingen in hun katalytische eigenschappen die kunnen ontstaan door het synergetische effect van de combinatie van deze materialen.

Dit proefschrift richt zich op theoretische studies die inzicht geven in het gedrag van koolstofhoudende materialen gemodificeerd met nanodeeltjes van een metaal of oxide in verschillende structurele configuraties en samenstellingen. Het doel is om een uitgebreid begrip te ontwikkelen van hoe veranderingen in de materiaaleigenschappen na modificatie de adsorptie en dissociatie van water beïnvloeden. Op basis van deze bevindingen is het de bedoeling om een solide basis te leggen voor het ontwerp van nieuwe materialen met verbeterde prestaties voor de bestudeerde processen. Hiervoor is een reeks chemische modellen van hybride materialen voorgesteld en onderzocht met behulp van ab-initio methoden. In het bijzonder zijn twee vormen van koolstofoppervlakken, namelijk koolstofnanobuizen (CNT) en grafeenoxide (GO), voorgesteld als substraten voor de afzetting van verschillende platina- en iridiumoxide nanodeeltjes.

Het resultaat van dit onderzoek is dat de voorgestelde koolstofoppervlakken platina (Pt_n , $n = 1 - 10, 13$) en stoichiometrisch iridiumoxide ($(\text{IrO}_2)_n$, $n = 1-6$) nanodeeltjes kunnen stabiliseren. De kleine diameter van de CNT beperkt duidelijk het interactiegebied tussen de deeltjes en het koolstofoppervlak. Bovendien blijken iridiumoxide "core-shell-achtige" structuren geschikter te zijn voor interactie met polaire oppervlakken zoals dat van GO. Verder werden wateradsorptie en verdere dissociatie geanalyseerd op geselecteerde Pt_n/CNT en $(\text{IrO}_2)_n/\text{CNT}$ systemen. Beide soorten systemen gaven uitstekende resultaten wat betreft activeringsenergieën voor de dissociatiestap. De resultaten van dit onderzoek moedigen experimentalisten aan om stabiele driehoekige Pt nanodeeltjes en nano-geschaalde iridiumoxide deeltjes op een CNT oppervlak te synthetiseren om polarisatie te bevorderen en de efficiëntie van katalyse te verhogen.

Tot slot onderzoekt dit proefschrift verder M_{13} monometallische nanodeeltjes en hun reactiviteit (door eenvoudige moleculen te gebruiken, zoals O_2 en N_2), met als doel om in de toekomst een vergelijkbare analyse te ontwikkelen voor M_{13} clusters op koolstofgebaseerde oppervlakken.

Dedicated to my wife, Inés

Contents

1	Introduction	5
1.1	Basics and motivations	5
1.1.1	Relevance of the problem	5
1.1.2	Carbonaceous materials	6
1.1.3	Water dissociation reaction	10
1.1.4	Group preliminary work	11
1.2	Objectives	13
2	Theoretical background	19
2.1	The Schrödinger equation and the Hamiltonian	19
2.2	Approximations and Corrections	21
2.2.1	Born–Oppenheimer Approximation	21
2.2.2	Hartree–Fock Theory	22
2.2.3	Density Functional Theory	24
2.2.4	Pseudopotentials	27
2.2.5	van der Waals Corrections	27
2.3	Minimum Energy Path and Nudged Elastic Band Method	28
3	Methodology	33
3.1	DFT calculations	33
3.1.1	Hubbard correction	34
3.2	Bond length distribution	34
3.3	Electrostatic potentials	35
3.4	Fermi softness analysis	35
3.5	Charge population analysis	36
3.6	Genetic algorithm method	36
3.7	Nudged Elastic Band method	36
4	Carbon surfaces	40
4.1	Introduction	40
4.2	Modeling	41

4.2.1	Carbon nanotube surface	41
4.2.2	Graphene oxide surface	41
4.3	Discussion	43
4.4	Summary	45
5	Platinum and iridium oxide nanoparticles	47
5.1	Platinum nanoparticles	47
5.1.1	Introduction	47
5.1.2	Results and discussion	47
5.2	Iridium oxide nanoparticles	54
5.2.1	Introduction	54
5.2.2	Results and discussion	56
5.3	Summary	64
6	Carbon nanotube surface modified with platinum	68
6.1	Introduction	68
6.2	Results and discussion	69
6.3	Summary	72
7	Carbon nanotube surface modified with iridium oxide	77
7.1	Introduction	77
7.2	Results and discussion	78
7.3	Summary	82
8	Graphene oxide modified with iridium oxide	86
8.1	Introduction	86
8.2	Results and discussion	87
8.3	Summary	88
9	Water adsorption and dissociation on Pt_n/CNT	91
9.1	Introduction	91
9.2	Results and discussion	93
9.2.1	Water molecule adsorption	93
9.2.2	Water molecule dissociation	94
9.3	Summary	97
10	Water adsorption and dissociation on (IrO₂)_n/CNT	102
10.1	Introduction	102
10.2	Results and discussion	102
10.2.1	Water molecule adsorption	102
10.2.2	Water molecule dissociation	104
10.3	Summary	108
11	Study of monometallic M₁₃ nanoparticles	110
11.1	Introduction	110

11.2 Results and discussion	112
11.2.1 M_{13} nanoparticles: energetic and geometric considerations	112
11.2.2 O_2 on M_{13} nanoparticles	114
11.2.3 N_2 on M_{13} nanoparticles	124
11.2.4 Discussion	127
11.3 Summary	134
Concluding remarks	141
Annexes	143
A.I Molecular adsorption of O_2 and N_2 on M_{13} : energies and bond lenght values	143
A.II Hubbard correction on Ir-related systems	145

Introduction

1.1 Basics and motivations

1.1.1 Relevance of the problem

There is no doubt that the search for new catalysts has been the heart of materials science in the last decades. Different areas have been focused in the design of materials trying to find a better catalyst for a specific reaction. Among these reactions, the dissociation of water molecules into adsorbed species, hydroxyl ($\text{OH}_{(\text{ads})}$) and hydrogen ($\text{H}_{(\text{ads})}$), is one of paramount importance in technological applications. As an example, the water dissociation process is an essential step in the water-gas shift reaction (WGS) [1, 2]. Various mechanisms have been proposed for WGS [3–5], where the generation of surface $\text{OH}_{(\text{ads})}$ species allows the subsequent oxidation of the adsorbed CO. Within these mechanisms, the dissociation of $\text{H}_2\text{O}_{(\text{ads})}$ into $\text{H}_{(\text{ads})}$ and $\text{OH}_{(\text{ads})}$ exhibits one of the highest energy barriers to overcome when the WGS reaction takes place in Cu-based catalysts [6, 7] commonly found in industry, as well as in other catalysts such as Pt and Pd [5].

Precious metal catalysts such as platinum and iridium, along with their derivatives, are widely used in numerous scientifically and technologically relevant reactions [1, 8–15]. However, their high cost, low stability, and limited availability of noble metals restrict their practical application on a large scale. Consequently, there is currently a strong motivation for the study and development of materials with potential application as catalysts that can serve as sustainable, efficient, and low-cost alternatives to traditional catalysts.

Considering their abundance and stability, various carbonaceous materials have been investigated for possible application as catalysts, both individually and modified with species of different chemical nature [16–18]. Among these carbonaceous materials, graphene, graphene oxide (GO), and carbon nanotubes (CNTs) can be distinguished by the unique physical and chemical properties derived from their structures. However, the discovery of these materials is relatively recent [19, 20], and despite much research conducted on them, there is still much to be explored regarding their properties and applications. Therefore, to optimize their application, we consider essential to generate new

knowledge about the properties and various surface processes involved at the atomic scale of hybrid materials that present novel adsorbate/surface carbon interfaces.

One way to achieve a reduction in the use of high-cost catalysts is through the synthesis of new compounds with low proportions of these metals or oxides, which maintain or enhance their desirable characteristics. In this regard, carbonaceous materials present large surface areas, with different geometries and compositions, that can act as supports for these metal and oxide clusters. While graphene exhibits a surface mostly composed of sp^2 carbons, graphene oxide (GO) tends to distribute in aromatic regions (where carbons have predominantly sp^2 hybridization) and hydrophilic regions (with atoms of variable hybridization, and rich areas in oxidized groups: hydroxyl, epoxide, carboxyl, etc.).

On the other hand, the tubular structures of CNTs imply surface configurations different from the aforementioned materials, due to chirality and curvature factors that vary according to their sizes and atomic arrangements. Each of these different substrates poses interesting possibilities for interaction with other species, such as metal nanoparticles or metal oxide nanoparticles, and in turn, new paths of chemical reactions of interest can be envisioned on these surfaces. However, further understanding of the synthesis conditions of these systems is still required to have control over their production and characteristics, especially regarding the changes in their catalytic properties that may arise from the synergistic effect of combining these materials.

Although the modification of carbonaceous materials with Pt and Ir oxides has been the subject of various theoretical studies [21–24], there are currently no works that systematically analyze the surface modification of the proposed carbonaceous materials with Pt and Ir oxide clusters containing a low number of atoms. In this sense, little is reported about the structural and electronic properties of these systems, and their possible activity as catalysts for simple reactions. Therefore, understanding the nature of catalytic sites at the atomic scale, identifying the causes of instability, and designing catalysts with optimal activity and stability towards reactions of interest remain pending challenges.

1.1.2 Carbonaceous materials

Carbon Nanotubes (CNTs)

Carbon nanotubes (CNTs) are a fascinating material for electrochemistry [25]. Because of their large surface area and chemical stability electrodes composed of CNTs have an extremely high and stable capacitance, which makes them very suitable for supercapacitors [26] capacitors with a high energy density, which can be discharged rapidly. In addition, their capability to store ions holds great promises for batteries [27], and chemically modified CNTs have proved to be good catalysts for the oxygen reduction reaction in fuel cells [15, 28].

Carbon nanotubes (CNTs) have shown interesting and unique physical and chemical properties (tubular structure, high chemical stability, low resistivity, high thermal and electrical conductivity, and enormous surface area) [29, 30] that allow them to be considered excellent materials, both individually [15, 28, 31] and modified with other types of atoms, molecules, or ions forming new hybrid compounds [32, 33].

Many of the properties of CNTs depend sensitively on their structure, characterized by their chirality

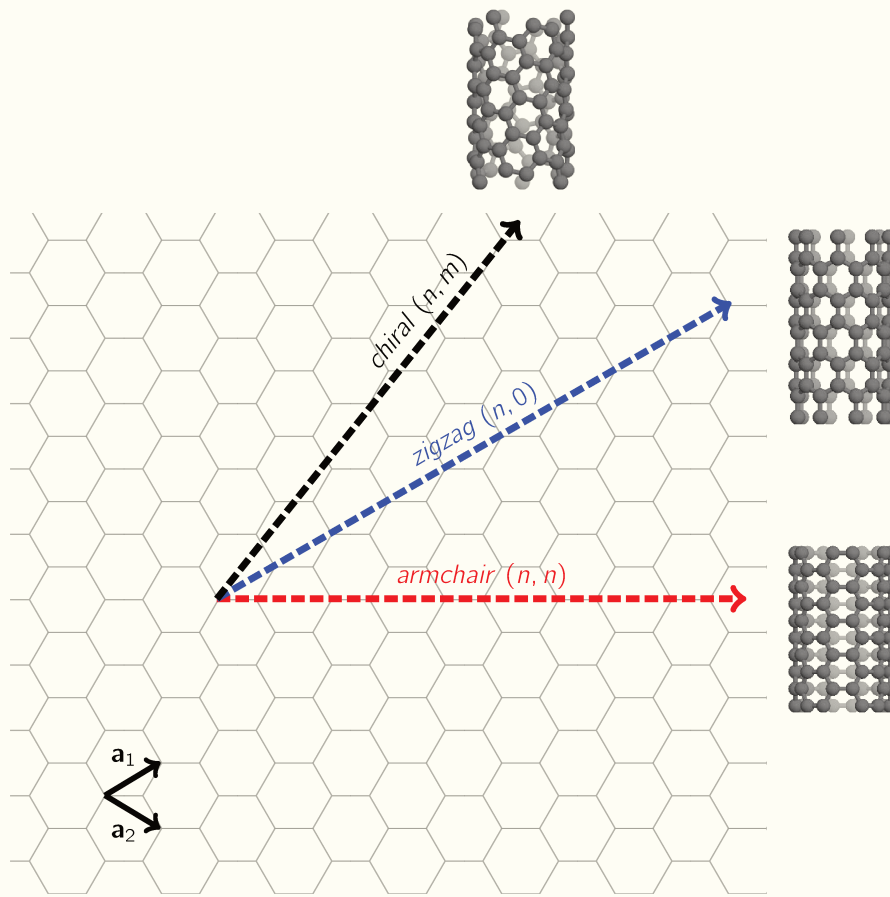


Figure 1.1: Depending on the direction in which a graphene layer is cut and rolled, single-walled carbon nanotubes (SWCNTs) can be classified into three types based on their chirality: *zigzag*, *armchair*, and *chiral*.

index (n, m) , which determines how the graphene layer used to form the nanotube is rolled, as shown in Fig. 1.1. Thus, three main groups are distinguished: *zigzag* $(n, 0)$, *armchair* (n, n) , and *chiral* $[(n, m), \text{ with } n \neq m \text{ and } m \neq 0]$. Depending on their structure, the electronic properties are strongly affected, allowing them to be classified as metallic or semiconductors with different band gaps.

The presence of an internal cavity within CNTs enables the creation of new hybrid materials by filling CNTs with different types of molecules or ions [18]. Several experimental and theoretical studies have demonstrated the potential to modify the electronic and magnetic properties of CNTs by inserting 3d transition metal nanostructures, such as Fe, Co, and Ni [34]. These insertions generate unique properties in the hybrid material. Numerous theoretical works report CNTs with single atoms inside, dimers, and even metallic chains, mainly analyzing variations according to the CNT diameter, energetics, electronic properties, and magnetic behavior. For single atoms inside CNTs, preferential adsorption of transition metals mainly occurs at hollow positions. On the other hand, including linear chains of Fe or Co in *zigzag* and *armchair* CNTs has shown that they possess high magnetic moments and spin polarization, especially with Co, transforming the behavior of the hybrid material into a semimetallic one with potential applications in spintronics.

CNTs are also important due to their external walls, which can serve as promising supports for

catalysts in various chemical reactions. Their curvature, diameter, and chirality can be exploited to tune the catalytic properties of the adsorbed particles to enhance performance. Tavakkoli et al. demonstrated experimentally and theoretically that it is possible to synthesize single-walled CNTs with ultra-low amounts of Pt (i.e., pseudo-atomically dispersed Pt). This material showed extraordinary electrocatalytic properties for the hydrogen evolution reaction (HER), reaching or even surpassing those of Pt/C electrodes [35]. Similarly, Kim et al. reached similar conclusions about Pt/CNT type catalysts, considering the hydrogen oxidation reaction (HOR) of a fuel cell anode of a PEMFC, highlighting their excellent durability, higher electrochemical active area, and higher and more stable current density [36].

These types of systems were also addressed through theoretical studies based on DFT calculations. It is reported that the adsorption of small Pt clusters, containing 1, 3, 4, 5, 7, 9, and 13 atoms, on CNTs of different chiralities is energetically favorable [23, 24, 36–39]. The interaction between the metal and the carbon surface usually involves electronic charge transfer, as well as significant charge delocalization and modification of the metal d-band, factors that affect the electrocatalytic properties of the hybrid material [37]. Metal nanoclusters, on the other hand, appear as novel active sites in catalysis due to their quantized electronic states and the structures they can exhibit, different from those known in their corresponding "bulk" states [21, 40].

The interaction of these systems with various chemical species has also been modeled and reported by different authors. It can be noted that the adsorption of molecules such as H_2 and H_2O on the outer surface of pristine CNTs is not favored [41, 42], while this interaction improves significantly in the presence of metallic clusters, according to reports for simple molecules such as H_2S , NH_3 , NO_2 , H_2O , CO , and O_2 [23, 38, 39]. Additionally, besides reducing the use of precious metal, Pt nanostructures have a higher number of low-coordination metal sites, which have been shown to be of great importance for catalytic phenomena, as they can stabilize reaction intermediates such as H, OH, and O [43].

Furthermore, there are other materials with excellent catalytic activity, such as IrO_2 among others, which share the negative characteristics of Pt in terms of cost, availability, and stability. However, experimental studies show that modifying CNTs with IrO_2 nanoclusters is feasible and considerably improves their catalytic activity towards reactions such as HER, OER, and ORR [44–47].

Ultrafine iridium oxide was experimentally investigated on multiwalled carbon nanotubes (MWCNTs). The material demonstrated efficiency for water oxidation and exhibited good stability in both alkaline and acidic media. The authors reported that the superior electrochemical performance might be attributed to the synergistic effect between IrO_2 and MWCNTs [46]. Similarly, an interesting theoretical-experimental study on subnanometric iridium dioxide clusters supported on MWCNTs also confirmed the high effectiveness of the material for water oxidation. The excellent performance of the iridium dioxide is proposed to originate from an enhanced number of unsaturated surface Ir atoms and a change in the local coordination environment [48]. Moreover, another study revealed the formation of a strong electronic interaction between IrO_2 nanoparticles and CNTs by XPS measurement [45].

Graphene oxide

Since its rediscovery around 2004, graphene has been widely investigated due to its unusual electronic and structural properties. Its applications vary from spintronics to solar cells, storage systems, redox enzyme encapsulation, sensors, and catalysts, among others. Although graphene can be studied from different perspectives, several articles focus mainly on the description of its physical characteristics, such as its electronic and magnetic behavior [49–51].

The ideal 2D periodic structure of pristine graphene is constituted by a hexagonal monolayer network of sp^2 hybridized carbon atoms. An interesting aspect of graphene is its ability to reconstruct the network due to intrinsic defects, leading to remarkable effects with potential applications. Both chemical and geometric modifications can lead to new behaviors, making it possible to tailor its local properties. Graphene shares many desirable characteristics of CNTs in terms of electronic and thermal conductivity, surface area, and chemical stability, among others.

Similarly, the pristine sheet is a relatively inert structure, remaining unreactive under most reaction conditions, as a desirable host should. Taking this into account, its oxidized form presents promising alternatives as a proactive support for different nanostructures due to its higher partial reactivity and localized oxidized groups, which serve as anchors for these particles. To achieve that, the use of graphene oxide with controlled characteristics and high purity is highly recommended.

Graphene oxide (GO), an experimental precursor of graphene [52, 53], is a non-stoichiometric compound composed of C, O, and H. Its variable proportions largely depend on synthesis conditions [54], which in turn define its structure and properties. GO is typically distributed in aromatic regions and hydrophilic regions. The presence of oxidized groups on its surface allows GO to form stable colloidal dispersions in aqueous solutions [55], making it a more practical support material and/or electrocatalyst compared to pristine graphene. However, although GO has been the main focus of research on the solution behavior of graphene derivatives [56], methods for suspending pure graphene in various media, including water [57–59], have also been developed. This makes it worthwhile to further study both materials for their potential applications in electrocatalysis and catalysis.

It is well known that advanced applications, such as green hydrogen production by water splitting, require the help of electrocatalysts for reactions to occur efficiently. In this regard, iridium derivatives show promising performance. Recently, a graphene oxide–iridium hybrid material was synthesized and tested by evaluating the oxygen evolution reaction, yielding good activity [60]. In addition, experimental studies on graphene oxide–iridium complexes demonstrate that this material is a highly active catalyst for redox reactions, such as the reduction of carbon dioxide to carbon monoxide [61].

Specifically, iridium has become popular for water reduction and oxidation due to its stability in both acidic and alkaline media. To clarify the behavior of iridium, Roy et al. [62] propose the synthesis of a highly active bifunctional catalyst for overall water splitting in both acidic and alkaline media. The material is based on iridium and vertical graphene, with a low catalyst loading that maintains performance in both electrolytes. Studies about the stability and catalytic activity of Ru, RuO_2 , Ir, and IrO_2 have been carried out to evaluate oxygen (OER) and hydrogen (HER) evolution reactions [63]. The authors found that independent of the electrolyte, OER activity decreases as $Ru > Ir \approx RuO_2 > IrO_2$, while dissolution increases as $IrO_2 \ll RuO_2 \ll Ir \ll Ru$. In addition, it was

reported that IrO_2 was more stable than RuO_2 , with a difference in dissolution amounts of ca. 30 times under similar conditions. For the HER, the metals were more active while the oxides were blocked by hydrogen bubbles, but no dissolution was detected.

Taking into account that graphene is an excellent support for hosting active nanomaterials, Kong et al. investigated IrO_2 nanoparticles supported on graphene using the hydrothermal method [64]. The hybrid material demonstrated higher activity for the OER compared to commercial IrO_2 and also showed good stability. On the other hand, IrO_2 was deposited on defects of the graphene sheet, and the morphology of the carbon monolayer and IrO_2 nanoparticles was characterized in detail at the nano level using atomic force microscopy (AFM) [65]. It was found that the IrO_2 nanoparticles were anchored on the edges of hole-like defects in the carbonaceous network, and the nanoparticle size was controlled by the extent of modification in the graphene. According to Mazanek et al., graphene-derived materials are not inherently good catalysts. However, metallic impurities can significantly improve the electrocatalytic activity of these substrates [66].

Although the modification of carbonaceous materials with Ir oxides has been explored in some theoretical research [21, 22], there are currently no studies analyzing the surface modification of GOs with Ir oxide clusters. In this regard, it is important to systematically and comprehensively investigate the structural and electronic properties of these systems, as well as their potential activity as catalysts for simple reactions. Understanding the nature of the catalytic sites at the atomic scale, identifying the causes of instability, and designing catalysts with optimal activity and stability for reactions of interest remain significant challenges.

1.1.3 Water dissociation reaction

For years, different groups around the world have focused on material design trying to find a better catalyst for a specific reaction. Among these reactions, the dissociation of water molecules into adsorbed species, hydroxyl ($\text{OH}_{(\text{ads})}$) and hydrogen ($\text{H}_{(\text{ads})}$), is of utmost importance in technological applications. For example, the water dissociation process is an essential step in the water–gas shift reaction (WGS) [1, 2]. Several mechanisms have been proposed for the WGS reaction [3–5], where the generation of surface $\text{OH}_{(\text{ads})}$ species allows for the subsequent oxidation of adsorbed CO. Within these mechanisms, the dissociation of $\text{H}_2\text{O}_{\text{ad}}$ into $\text{H}_{(\text{ads})}$ and $\text{OH}_{(\text{ads})}$ exhibits one of the highest energy barriers to overcome when the WGS reaction takes place on Cu–based catalysts [6, 7], which are commonly found in the industry, as well as on other catalysts such as Pt and Pd [5], and IrO_2 [14].

A quick search shows that there is a host of literature about Pt, its geometries, its reactivity as well as its performance as catalyst for reactions of technological interests. Phatak et al. [67] investigated the dissociation of water on (111) surfaces of five metals (Cu, Au, Ni, Pd and Pt). The authors found the lowest barrier for Pt(111) (0.75 eV). Other authors also analyzed this reaction on noble metal surfaces such as Pt and Pd. Similarly, they found high activation energies for flat surfaces [5, 68], while on stepped and kinked surfaces, the presence of low coordinated atoms suggests a decrease in the energy barrier of the process [68].

In addition, Fajin et al. [69] studied the reaction theoretically on platinum nanoparticles ranging from 13 to 40 atoms in gas phase. The authors reported that a water molecule prefers to adsorb at the

low coordinated atoms at the edges of the particle. Furthermore, the authors suggest that only small Pt nanoparticles can promote water dissociation under working conditions, since for all the analyzed cases, the activation energies were lower than those for a Pt(111) surface. Moreover, Bazhenov et al. [9] developed theoretical models for two types of nanoparticles, Pt₅₅ and Pt₁₄₇, where the water adsorption found to be strongly dependent on the nature of the surface sites, in terms of coordination and d-band structure. Specifically, they report that the energy of the transition state increases linearly with the coordination number of the surface sites in the nanoparticle and with the water adsorption energy, while it decreases linearly with the increase in the *d*-band center of the site.

In order to improve the design of materials, researchers have studied not only pure metals but also oxides that can enhance the catalytic activity of chemical reactions. Consequently, metal oxides have been investigated for their roles in energy conversion and storage, particularly in photochemical and electrochemical water oxidation. In general, these processes involve a catalyst–water interface, whose understanding is crucial for rationalizing the overall phenomenon. In water–dissociation various intermediates (i.e., H_(ads), OH_(ads), and H₂O_(ads)) are involved. Therefore, in alkaline media specifically, the water-dissociation process involves multistep reactions. This indicates that the adsorption-desorption behaviors of these intermediates should be considered when designing the active centers of the oxides. Among several metals, IrO₂ is the least studied compared to Ru- and Ti-oxides. Water adsorption on the (110) IrO₂ facet has been addressed by DFT calculations, suggesting a strong H₂O–IrO₂ interaction with a tentative dissociation of the molecules [70].

Moreover, thermal effects and hydrogen species mobility on the (110) and (011) IrO₂ surfaces were analyzed using ab initio molecular dynamics (AIMD) [71]. Results indicate that the adsorption of a water molecule occurs in its dissociative form on the (110) IrO₂ surface and in its molecular form on the (011) IrO₂ surface. Meanwhile, on (110) IrO₂, the main water monolayer is fully dissociated, whereas on (011) IrO₂, it exhibits a degree of dissociation ranging from 50 % to 75 %. The authors argue that several factors, in addition to intrinsic water adsorption, are responsible for the degree of dissociation of adsorbed water on various metal oxides, with IrO₂ being the most likely to induce dissociation.

Finally, it has been suggested that two main factors govern the way water adsorption occurs (molecular or dissociative) on small nanoparticles of IrO₂: metal coordination and hydrogen bonding with the oxygen bridge atoms of the IrO₂ particle. Results show that IrO₂ nanoparticle models are somewhat more ionic than extended surfaces and this favors the direct H₂O–metal interaction. Adsorption at iridium nanoparticle axial vacant sites implies stronger Ir–H₂O interactions, which favor water dissociation [12].

1.1.4 Group preliminary work

Our group began studying ion-embedded carbon nanotubes using Density Functional Theory (DFT) with the intention of describing such systems from an atomistic point of view. From W. Schmickler's work on the properties of pure and nitrogen-doped carbon double layers [72, 73], it is known that metals screen charge much better than carbonaceous materials. In this context, exploratory calculations were performed for both carbon nanotubes and gold nanotubes with diameters varying in the range of 6 – 10 Å. The (8,0) and (10,0) carbon tubes we selected were actually rings of 5 Å

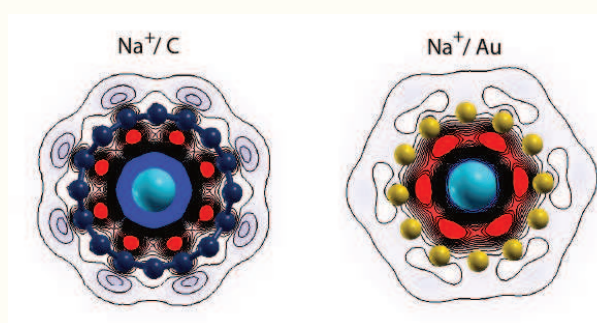


Figure 1.2: Charge difference plots for a sodium ion in a (8,0) carbon ring with 8 hexagons (left) and in a gold tube (right). Red (blue) indicates an excess of negative (positive) charge. Figure taken from ref. [74]

length. Since it is important to obtain an ion with unit charge, a cesium atom was chosen as our first test particle because Cs has the lowest ionization energy. In fact, the Cs atom was completely ionized: both Bader and Voronoi analyses gave a unitary positive charge in all cases investigated. Encouraged by these results, calculations were carried out for Na and Li, and always observed full ionization. The optimum position of the ion was always at the center of the tube [74].

In all cases, an image charge on the walls of the tubes was observed —see Fig. 1.2 [74]. The image charge (red in the figure) is always closer to the cation than the gold or carbon cores. Since gold is a much better conductor than carbon, the separation between the charge on the cation and the image charge is smaller for the gold rings. For all systems considered the energies of insertion were determined. With the exception of Cs in the gold nanotube, which is too big to fit in, insertion is exothermal. Since the ions are in the center of the tube and fully charged, the interaction seems to be dominated by electrostatics.

For ion-ion interactions the potential generated by the ions along the axis of the tube is important. As predicted by the work of Kondrat and Kornyshev [75], the Coulomb potential of the ions is strongly screened by the image charge on the tube. As may be expected, gold, as a metal, screens the charge better than the semiconducting nanotubes; in the case of the latter, the narrow tube screens better than the wider one. All tubes screen better than a perfect classical metal with the diameter of the carbon tubes, which shows that the work of Kondrat and Kornyshev underestimates the screening effect severely. In all cases, the difference with the unscreened Coulomb potential is enormous.

Thus, ion-ion interactions within the tubes are severely reduced, which makes it possible to store more ions of the same sign into the tubes. The thinner the tubes, the better is the screening. This explains why narrow tubes store charge so well.

Additionally, the behavior of some anions: Cl^- , Br^- , and I^- was investigated by Mohammadzadeh et al. [76]. All ions investigated, no matter if anions or cations, produce the same screened Coulomb potential along a (10,0) carbon tube. Differences at short distances are caused by the extension of the p orbitals of the halides, which increase down the periodic table. There may be small systematic differences between anions and cations at very large distances, possibly due to the polarizability of the anions. In any case, this indicates that the anions carry a full negative charge. This conclusion

is supported by an examination of the electronic density of states, which shows that the p orbitals of the halides are occupied.

1.2 Objectives

The doctoral thesis work aims to address theoretical studies that allow for the understanding of the behavior of carbonaceous materials (carbon nanotubes and graphene oxides) modified with nanoparticles of a metal or oxide in different structural configurations and compositions. The goal is to rationalize how changes in the material properties after modification would influence the water adsorption and dissociation. It is expected that, based on these findings, rational foundations can be established for the design of new materials with superior performance for the studied processes.

In this context, the specific objectives are:

- to develop theoretical models, based on first principles, of carbonaceous systems such as carbon nanotubes and graphene oxide sheets, modified with platinum and iridium oxide nanoparticles in different sizes and configurations;
- to analyze the characteristics of the resulting geometries and identify any modifications to their electronic properties;
- to evaluate the impact of the modifications generated in the most stable systems with respect to chemical reactions of interest, such as water molecule adsorption and dissociation, by identifying the optimal interaction sites and modes for the different species, and obtaining the minimum energy pathways and activation energies.

References for Chapter 1

- [1] M. M. Kauppinen, V. Korpelin, A. M. Verma, M. M. Melander, and K. Honkala, "Escaping scaling relationships for water dissociation at interfacial sites of zirconia-supported Rh and Pt clusters," *The Journal of Chemical Physics*, vol. 151, no. 16, p. 164 302, 2019.
- [2] A. Chutia, A. Thetford, M. Stamatakis, and C. R. A. Catlow, "A DFT and KMC based study on the mechanism of the water gas shift reaction on the Pd (100) surface," *Physical Chemistry Chemical Physics*, vol. 22, no. 6, p. 3620, 2020.
- [3] J. Nakamura, J. M. Campbell, and C. T. Campbell, "Kinetics and mechanism of the water-gas shift reaction catalysed by the clean and Cs-promoted Cu (110) surface: A comparison with Cu (111)," *Journal of the Chemical Society, Faraday Transactions*, vol. 86, no. 15, p. 2725, 1990.
- [4] C. Ovesen, P. Stoltze, J. Nørskov, and C. Campbell, "A kinetic model of the water gas shift reaction," *Journal of Catalysis*, vol. 134, no. 2, p. 445, 1992.
- [5] J. P. Clay, J. P. Greeley, F. H. Ribeiro, W. N. Delgass, and W. F. Schneider, "DFT comparison of intrinsic WGS kinetics over Pd and Pt," *Journal of Catalysis*, vol. 320, p. 106, 2014.
- [6] C. Ovesen *et al.*, "A microkinetic analysis of the water-gas shift reaction under industrial conditions," *Journal of Catalysis*, vol. 158, no. 1, p. 170, 1996.
- [7] A. A. Gokhale, J. A. Dumesic, and M. Mavrikakis, "On the mechanism of low-temperature water gas shift reaction on copper," *Journal of the American Chemical Society*, vol. 130, no. 4, p. 1402, 2008.
- [8] C. F. Dickens, J. H. Montoya, A. R. Kulkarni, M. Bajdich, and J. K. Nørskov, "An electronic structure descriptor for oxygen reactivity at metal and metal-oxide surfaces," *Surface Science*, vol. 681, p. 122, 2019.
- [9] A. S. Bazhenov, L. Lefferts, and K. Honkala, "Adsorption and activation of water on cuboctahedral rhodium and platinum nanoparticles," *The Journal of Physical Chemistry C*, vol. 121, no. 8, p. 4324, 2017.
- [10] W. T. Cahyanto, S. Zulaehah, W. Widanarto, F. Abdullatif, M. Effendi, and H. Kasai, "Theoretical study of an almost barrier-free water dissociation on a platinum (111) surface alloyed with ruthenium and molybdenum," *ACS Omega*, vol. 6, no. 16, p. 10 770, 2021.
- [11] S. Liu and S. Huang, "The role of interface charge transfer on Pt based catalysts for water splitting," *International Journal of Hydrogen Energy*, vol. 43, no. 32, p. 15 225, 2018.

- [12] D. González, M. Sodupe, L. Rodríguez-Santiago, and X. Solans-Monfort, "Surface morphology controls water dissociation on hydrated IrO₂ nanoparticles," *Nanoscale*, vol. 13, no. 34, p. 14480, 2021.
- [13] Y. Ping, R. J. Nielsen, and W. A. Goddard III, "The reaction mechanism with free energy barriers at constant potentials for the oxygen evolution reaction at the IrO₂ (110) surface," *Journal of the American Chemical Society*, vol. 139, no. 1, p. 149, 2017.
- [14] D. González, M. Sodupe, L. Rodríguez-Santiago, and X. Solans-Monfort, "Metal coordination determines the catalytic activity of IrO₂ nanoparticles for the oxygen evolution reaction," *Journal of Catalysis*, vol. 412, p. 78, 2022.
- [15] Z. Chen, X. Duan, W. Wei, S. Wang, and B.-J. Ni, "Iridium-based nanomaterials for electrochemical water splitting," *Nano Energy*, vol. 78, p. 105270, 2020.
- [16] A. L. Dicks, "The role of carbon in fuel cells," *Journal of Power Sources*, vol. 156, no. 2, p. 128, 2006.
- [17] P. Serp and J. L. Figueiredo, *Carbon materials for catalysis*. John Wiley & Sons, 2008.
- [18] P. Serp and B. Machado, *Nanostructured carbon materials for catalysis*. Royal Society of Chemistry, 2015.
- [19] S. Iijima, "Helical microtubules of graphitic carbon," *Nature*, vol. 354, no. 6348, p. 56, 1991.
- [20] K. S. Novoselov *et al.*, "Electric field effect in atomically thin carbon films," *Science*, vol. 306, no. 5696, p. 666, 2004.
- [21] I. I. Aysan, T. Gorkan, I. Ozdemir, Y. Kadioglu, G. Gökolu, and E. Aktürk, "Electronic structure, cohesive and magnetic properties of iridium oxide clusters adsorbed on graphene," *Journal of Molecular Graphics and Modelling*, vol. 101, p. 107726, 2020.
- [22] B. A. Barker *et al.*, "Geometry and electronic structure of iridium adsorbed on graphene," *Physical Review B*, vol. 99, no. 7, p. 075431, 2019.
- [23] P. Pannopard, P. Khongpracha, M. Probst, and J. Limtrakul, "Gas sensing properties of platinum derivatives of single-walled carbon nanotubes: A DFT analysis," *Journal of Molecular Graphics and Modelling*, vol. 28, no. 1, p. 62, 2009.
- [24] D. H. Chi *et al.*, "Electronic structures of Pt clusters adsorbed on (5,5) single wall carbon nanotube," *Chemical Physics Letters*, vol. 432, no. 1-3, p. 213, 2006.
- [25] E. Frackowiak, S. Gautier, H. Gaucher, S. Bonnamy, and F. Beguin, "Electrochemical storage of lithium in multiwalled carbon nanotubes," *Carbon*, vol. 37, no. 1, p. 61, 1999.
- [26] R. H. Baughman, A. A. Zakhidov, and W. A. De Heer, "Carbon nanotubes—the route toward applications," *Science*, vol. 297, no. 5582, p. 787, 2002.
- [27] P. Sehrawat, C. Julien, and S. Islam, "Carbon nanotubes in Li-ion batteries: A review," *Materials Science and Engineering: B*, vol. 213, p. 12, 2016.
- [28] Y. Li *et al.*, "An oxygen reduction electrocatalyst based on carbon nanotube-graphene complexes," *Nature Nanotechnology*, vol. 7, no. 6, p. 394, 2012.
- [29] K. S. Ibrahim, "Carbon nanotubes? properties and applications: A review," *Carbon Letters*, vol. 14, no. 3, p. 131, 2013.
- [30] Y. R. Poudel and W. Li, "Synthesis, properties, and applications of carbon nanotubes filled with foreign materials: A review," *Materials Today Physics*, vol. 7, p. 7, 2018.

- [31] J. Stacy, Y. N. Regmi, B. Leonard, and M. Fan, "The recent progress and future of oxygen reduction reaction catalysis: A review," *Renewable and Sustainable Energy Reviews*, vol. 69, p. 401, 2017.
- [32] Q. Zhang and J. Guan, "Atomically dispersed catalysts for hydrogen/oxygen evolution reactions and overall water splitting," *Journal of Power Sources*, vol. 471, p. 228446, 2020.
- [33] Y. Wang, X. Huang, and Z. Wei, "Recent developments in the use of single-atom catalysts for water splitting," *Chinese Journal of Catalysis*, vol. 42, no. 8, p. 1269, 2021.
- [34] U. K. Gautam *et al.*, "Recent developments in inorganically filled carbon nanotubes: Successes and challenges," *Science and Technology of Advanced Materials*, vol. 11, no. 5, p. 054501, 2010.
- [35] M. Tavakkoli *et al.*, "Electrochemical activation of single-walled carbon nanotubes with pseudo-atomic-scale platinum for the hydrogen evolution reaction," *ACS Catalysis*, vol. 7, no. 5, p. 3121, 2017.
- [36] T. Kim, Y. Kwon, S. Kwon, and J. G. Seo, "Substrate effect of platinum-decorated carbon on enhanced hydrogen oxidation in PEMFC," *ACS Omega*, vol. 5, no. 41, p. 26902, 2020.
- [37] N. T. Cuong, A. Fujiwara, T. Mitani, and D. H. Chi, "Effects of carbon supports on Pt nano-cluster catalyst," *Computational Materials Science*, vol. 44, no. 1, p. 163, 2008.
- [38] N. T. Cuong, A. Sugiyama, A. Fujiwara, T. Mitani, and D. H. Chi, "Density functional study of Pt₄ clusters adsorbed on a carbon nanotube support," *Physical Review B*, vol. 79, no. 23, p. 235417, 2009.
- [39] X. Zhang, H. Cui, D. Chen, X. Dong, and J. Tang, "Electronic structure and H₂S adsorption property of Pt₃ cluster decorated (8,0) SWCNT," *Applied Surface Science*, vol. 428, p. 82, 2018.
- [40] K. Klyukin, A. Zagalskaya, and V. Alexandrov, "Ab initio thermodynamics of iridium surface oxidation and oxygen evolution reaction," *Journal of Physical Chemistry C*, vol. 122, no. 51, p. 29350, 2018.
- [41] L. A. Elalfy, W. M. Hassan, and W. N. Akl, "Ab initio density functional theory investigation of the interaction between carbon nanotubes and water molecules during water desalination process," *Journal of Chemistry*, vol. 2013, no. 1, p. 813592, 2013.
- [42] Y. S. Al-Hamdani, D. Alfe, and A. Michaelides, "How strongly do hydrogen and water molecules stick to carbon nanomaterials?" *Journal of Chemical Physics*, vol. 146, no. 9, 2017.
- [43] M. J. Kolb, F. Calle-Vallejo, L. B. Juurlink, and M. Koper, "Density functional theory study of adsorption of H₂O, H, O, and OH on stepped platinum surfaces," *Journal of Chemical Physics*, vol. 140, no. 13, 2014.
- [44] E. Jakubovskij, A. Selskis, I. Ignatjev, G. Stalnionis, and V. ablinskas, "Synthesis and characterization of iridium-doped multi-walled carbon nanotubes," *Lithuanian Journal of Physics*, vol. 61, no. 4, 2021.
- [45] R. Badam, M. Hara, H.-H. Huang, and M. Yoshimura, "Synthesis and electrochemical analysis of novel IrO₂ nanoparticle catalysts supported on carbon nanotube for oxygen evolution reaction," *International Journal of Hydrogen Energy*, vol. 43, no. 39, p. 18095, 2018.
- [46] X. Wen, L. Bai, M. Li, and J. Guan, "Ultrafine iridium oxide supported on carbon nanotubes for efficient catalysis of oxygen evolution and oxygen reduction reactions," *Materials Today Energy*, vol. 10, p. 153, 2018.

- [47] D. H. Kweon *et al.*, "Ruthenium anchored on carbon nanotube electrocatalyst for hydrogen production with enhanced faradaic efficiency," *Nature Communications*, vol. 11, no. 1, p. 1278, 2020.
- [48] J. Guan, D. Li, R. Si, S. Miao, F. Zhang, and C. Li, "Synthesis and demonstration of subnanometric iridium oxide as highly efficient and robust water oxidation catalyst," *ACS Catalysis*, vol. 7, no. 9, p. 5983, 2017.
- [49] A. H. Castro Neto, F. Guinea, N. M. Peres, K. S. Novoselov, and A. K. Geim, "The electronic properties of graphene," *Reviews of Modern Physics*, vol. 81, no. 1, p. 109, 2009.
- [50] X. Liu *et al.*, "Growth morphology and properties of metals on graphene," *Progress in Surface Science*, vol. 90, no. 4, p. 397, 2015.
- [51] E. Y. Andrei, G. Li, and X. Du, "Electronic properties of graphene: A perspective from scanning tunneling microscopy and magnetotransport," *Reports on Progress in Physics*, vol. 75, no. 5, p. 056 501, 2012.
- [52] M. S. A. Bhuyan, M. N. Uddin, M. M. Islam, F. A. Bipasha, and S. S. Hossain, "Synthesis of graphene," *International Nano Letters*, vol. 6, p. 65, 2016.
- [53] K. A. Madurani, S. Suprpto, N. I. Machrita, S. L. Bahar, W. Illiya, and F. Kurniawan, "Progress in graphene synthesis and its application: History, challenge and the future outlook for research and industry," *ECS Journal of Solid State Science and Technology*, vol. 9, no. 9, p. 093013, 2020.
- [54] L. Sun, "Structure and synthesis of graphene oxide," *Chinese Journal of Chemical Engineering*, vol. 27, no. 10, p. 2251, 2019.
- [55] S. Stankovich, R. D. Piner, X. Chen, N. Wu, S. T. Nguyen, and R. S. Ruoff, "Stable aqueous dispersions of graphitic nanoplatelets via the reduction of exfoliated graphite oxide in the presence of poly (sodium 4-styrenesulfonate)," *Journal of Materials Chemistry*, vol. 16, no. 2, p. 155, 2006.
- [56] N. Ye, Z. Wang, S. Wang, H. Fang, and D. Wang, "Aqueous aggregation and stability of graphene nanoplatelets, graphene oxide, and reduced graphene oxide in simulated natural environmental conditions: Complex roles of surface and solution chemistry," *Environmental Science and Pollution Research*, vol. 25, p. 10956, 2018.
- [57] Y.-J. Park, S. Y. Park, and I. In, "Preparation of water soluble graphene using polyethylene glycol: Comparison of covalent approach and noncovalent approach," *Journal of Industrial and Engineering Chemistry*, vol. 17, no. 2, p. 298, 2011.
- [58] Y. Si and E. T. Samulski, "Synthesis of water soluble graphene," *Nano Letters*, vol. 8, no. 6, p. 1679, 2008.
- [59] T. Skaltsas, N. Karousis, H.-J. Yan, C.-R. Wang, S. Pispas, and N. Tagmatarchis, "Graphene exfoliation in organic solvents and switching solubility in aqueous media with the aid of amphiphilic block copolymers," *Journal of Materials Chemistry*, vol. 22, no. 40, p. 21507, 2012.
- [60] M. González-Ingelmo *et al.*, "On the study of the preparation of graphene-anchored NHC-iridium catalysts from a coke-like waste with application in water splitting," *Applied Surface Science*, vol. 655, p. 159 556, 2024.

- [61] T.-R. Chen, F.-S. Wu, H.-P. Lee, and K. H.-C. Chen, "Diiridium bimetallic complexes function as a redox switch to directly split carbonate into carbon monoxide and oxygen," *Journal of the American Chemical Society*, vol. 138, no. 11, p. 3643, 2016.
- [62] S. B. Roy *et al.*, "Iridium on vertical graphene as an all-round catalyst for robust water splitting reactions," *Journal of Materials Chemistry A*, vol. 7, no. 36, p. 20 590, 2019.
- [63] S. Cherevko *et al.*, "Oxygen and hydrogen evolution reactions on Ru, RuO₂, Ir, and IrO₂ thin film electrodes in acidic and alkaline electrolytes: A comparative study on activity and stability," *Catalysis Today*, vol. 262, p. 170, 2016.
- [64] F.-D. Kong, S. Zhang, G.-P. Yin, J. Liu, and Z.-Q. Xu, "IrO₂-graphene hybrid as an active oxygen evolution catalyst for water electrolysis," *International Journal of Hydrogen Energy*, vol. 38, no. 22, p. 9217, 2013.
- [65] S. Ogawa, M. Hara, S. Suzuki, P. Joshi, and M. Yoshimura, "Controlled deposition of iridium oxide nanoparticles on graphene," *Electrochemistry*, vol. 88, no. 5, p. 392, 2020.
- [66] V. Mazánek *et al.*, "Ultrapure graphene is a poor electrocatalyst: Definitive proof of the key role of metallic impurities in graphene-based electrocatalysis," *ACS Nano*, vol. 13, no. 2, p. 1574, 2019.
- [67] A. A. Phatak, W. N. Delgass, F. H. Ribeiro, and W. F. Schneider, "Density functional theory comparison of water dissociation steps on Cu, Au, Ni, Pd, and Pt," *Journal of Physical Chemistry C*, vol. 113, no. 17, p. 7269, 2009.
- [68] J. L. Fajin, M. N. DS Cordeiro, and J. R. Gomes, "Density functional theory study of the water dissociation on platinum surfaces: General trends," *Journal of Physical Chemistry A*, vol. 118, no. 31, p. 5832, 2014.
- [69] J. L. Fajin, A. Bruix, M. N. D. Cordeiro, J. R. Gomes, and F. Illas, "Density functional theory model study of size and structure effects on water dissociation by platinum nanoparticles," *Journal of Chemical Physics*, vol. 137, no. 3, 2012.
- [70] S. Siahrostami and A. Vojvodic, "Influence of adsorbed water on the oxygen evolution reaction on oxides," *Journal of Physical Chemistry C*, vol. 119, no. 2, p. 1032, 2015.
- [71] D. Gonzalez *et al.*, "Water adsorption on MO₂ (M=Ti, Ru, and Ir) surfaces. importance of octahedral distortion and cooperative effects," *ACS Omega*, vol. 4, no. 2, p. 2989, 2019.
- [72] N. Luque and W. Schmickler, "The electric double layer on graphite," *Electrochimica Acta*, vol. 71, p. 82, 2012.
- [73] M. Juarez, L. Mohammadzadeh, and W. Schmickler, "The double-layer capacity of nitrogen-doped graphite," *Electrochemistry Communications*, vol. 36, p. 50, 2013.
- [74] A. Goduljan, F. Juarez, L. Mohammadzadeh, P. Quaino, E. Santos, and W. Schmickler, "Screening of ions in carbon and gold nanotubes—A theoretical study," *Electrochemistry Communications*, vol. 45, p. 48, 2014.
- [75] S. Kondrat and A. Kornyshev, "Superionic state in double-layer capacitors with nanoporous electrodes," *Journal of Physics: Condensed Matter*, vol. 23, no. 2, p. 022 201, 2010.
- [76] L. Mohammadzadeh, A. Goduljan, F. Juarez, P. Quaino, E. Santos, and W. Schmickler, "Nanotubes for charge storage—towards an atomistic model," *Electrochimica Acta*, vol. 162, p. 11, 2015.

Theoretical background

By employing theoretical models, it is possible to describe the properties of materials at the nanoscale with great precision, utilizing methods based on the fundamental laws of quantum mechanics. Among these methods, first-principles simulations are of paramount importance, as their approximations allow for the evaluation of observable macroscopic variables through the theoretical description of the interactions between atoms and electrons. Within the *ab initio* methods, those derived from Density Functional Theory (DFT) are particularly notable, as they provide an accurate reproduction of system properties at a reasonable computational cost. In this thesis, the first-principles DFT method serves as a valuable tool to achieve its objectives. Below, some key aspects of the methods used are briefly described.

2.1 The Schrödinger equation and the Hamiltonian

Any theoretical description must begin with defining the system to be considered and determining the interactions present within that system. This information is summarized in the Hamiltonian, the central expression for any theoretical treatment. All physical and chemical properties can be derived from this Hamiltonian. As the focus here is on nanoscopic particles, such as electrons and atoms, the appropriate description is provided by quantum mechanics and requires the solution of the Schrödinger equation. In this section, a comprehensive overview of the fundamental principles of quantum chemistry will be provided. The general definition of the Hamiltonian and the well-known Schrödinger equation are presented first. Then, different methods for its resolution, such as Hartree–Fock Theory and Density Functional Theory, are introduced.

The quantum Hamiltonian represents the total energy of the system. Interestingly, despite the complexity and richness of the equations that have radically transformed our understanding of the universe, these equations are typically expressed in a very simple and pure form. The equations that describe atomic systems are no exception:

$$\hat{H}\Psi = E\Psi \quad (2.1)$$

$$\hat{H}\Psi = i\hbar \frac{\partial \Psi}{\partial t} \quad (2.2)$$

These are the time-independent (eq. 2.1) and time-dependent (eq. 2.2) Schrödinger equations, respectively. $\Psi = \Psi(\mathbf{r}, \mathbf{R}, t)$ is the time-dependent wave function for all particles, where $\mathbf{r} = \{\mathbf{r}_i\}$ denotes the coordinates of the electrons and $\mathbf{R} = \{\mathbf{R}_j\}$ denotes the coordinates of the nuclei. E is the energy of the system, \hbar is the reduced Planck constant, and \hat{H} is the Hamiltonian operator that acts on the entire system. The time dependence of Ψ can be omitted in the notation, considering that this variable is included parametrically in the functions $\mathbf{r} = \mathbf{r}(t)$ and $\mathbf{R} = \mathbf{R}(t)$.

As Paul Dirac stated when he published the relativistic equation for the electron, the majority of physics and all of chemistry are explained by these equations (eq. 2.1 and eq. 2.2).

Disregarding relativistic and magnetic effects, the Hamiltonian (\hat{H}) that describes the nuclei and electrons can be written as (eq. 2.3):

$$\hat{H} = \hat{T}_{\text{nucl}} + \hat{T}_{\text{el}} + \hat{V}_{\text{nucl-nucl}} + \hat{V}_{\text{nucl-el}} + \hat{V}_{\text{el-el}} \quad (2.3)$$

where T and V represent the kinetic and electrostatic interactions, respectively, both referring to electrons (el) and nuclei (nucl).

The terms of the Hamiltonian are defined by the following expressions (eqs. 2.4–2.8), in which spin is not considered:

$$\hat{T}_{\text{nucl}} = -\frac{\hbar^2}{2} \sum_{j=1}^N \frac{\nabla_j^2}{M_j} \quad (2.4)$$

$$\hat{T}_{\text{el}} = -\frac{\hbar^2}{2m} \sum_{i=1}^n \nabla_i^2 \quad (2.5)$$

$$\hat{V}_{\text{nucl-nucl}} = \frac{1}{2} \sum_{j \neq l} \frac{Z_j Z_l e^2}{|\mathbf{R}_j - \mathbf{R}_l|} \quad (2.6)$$

$$\hat{V}_{\text{nucl-el}} = - \sum_{i,j} \frac{Z_j e^2}{|\mathbf{r}_i - \mathbf{R}_j|} \quad (2.7)$$

$$\hat{V}_{\text{el-el}} = \frac{1}{2} \sum_{i \neq k} \frac{e^2}{|\mathbf{r}_i - \mathbf{r}_k|} \quad (2.8)$$

where ∇ is the gradient operator, e and m represent the charge and the rest mass of the electron, respectively, M_j is the rest mass of the nucleus, and Z_j is its charge relative to that of the electron.

The solution of eq. 2.1, along with the definition of the Hamiltonian in eq. 2.3, provides all the necessary information about the system under study. However, its complexity makes an exact

analytical solution impossible, except for small molecules. For the calculation of more complex electronic structures, a series of approximations and corrections must be made in solving the Schrödinger equation. Among these are the following:

- Born–Oppenheimer approximation: It allows the decoupling of the motion of electrons and nuclei.
- Hartree–Fock theory: It provides an approximate form of the Schrödinger equations based on single-particle orbitals. This approach is more computationally accessible than multi-particle wave function methods, as it uses an iterative calculation scheme.
- Density Functional Theory (DFT): It provides an effective method for solving quantum mechanical problems by replacing electronic wave functions with electronic charge densities as the fundamental variables.
- van der Waals interaction corrections: These corrections allow for a more accurate description of long-range interactions.
- Pseudopotentials: By using pseudopotentials, it is possible to eliminate a large number of chemically inert electrons and avoid abrupt oscillations in the wave functions near the central region of atoms. This reduces the calculation to that of the outermost (or valence) electrons and, consequently, the number of basis functions needed to describe the total wave function.
- Periodic Boundary Conditions: They enable the simulation of infinitely extended crystals by reducing the problem to the calculation of a single simulation cell that is periodically repeated.

The following section describes some of the approximations and corrections used throughout this thesis.

2.2 Approximations and Corrections

In principle, since the formulation of Quantum Mechanics, the method for obtaining exact structural information from a molecular system has been formally established. However, as Dirac stated, while it is possible to know the theory, the mathematics required to fully develop it is not yet available. Consequently, it is necessary to resort to various approximations to make quantum mechanical calculations less computationally expensive. The approximations and corrections relevant to the work described in this thesis are outlined below.

2.2.1 Born–Oppenheimer Approximation

This is the first approximation made in most quantum mechanics calculations, as it allows us to decouple the motion of nuclei and electrons without losing accuracy in the efficient characterization of structural and electronic properties [1]. This treatment is reasonable because the mass of a nucleus is at least 10^3 times greater than the mass of an electron, and therefore, its motion is much slower in comparison. Thus, the nuclei can be considered as fixed at certain positions, $\mathbf{R}^* = \{\mathbf{R}_j^*\}$, and solve the problem for the electrons, which adapt 'instantly' to any nuclear arrangement. In this context, the wave function of the system can be separated into a nuclear factor and an electronic factor, as

follows:

$$\Psi(\mathbf{r}, \mathbf{R}^*) = \psi^{\text{nuc}}(\mathbf{R}^*)\psi^{\text{el}}(\mathbf{r}, \mathbf{R}^*) \quad (2.9)$$

In a first step, the electronic part of the system can be approximately solved by neglecting the nuclear kinetic energy:

$$\hat{H}\psi^{\text{el}}(\mathbf{r}, \mathbf{R}^*) = E_{\text{el}}\psi^{\text{el}}(\mathbf{r}, \mathbf{R}^*) \quad (2.10)$$

being

$$\hat{H}_{\text{el}} = \hat{T}_{\text{el}} + \hat{V}_{\text{nuc-el}} + \hat{V}_{\text{el-el}} \quad (2.11)$$

The obtained electronic energy, E_{el} , depends on the chosen positions, \mathbf{R}^* . By varying these positions and repeatedly solving the electronic Schrödinger equation (eq. 2.10), E_{el} is obtained as a function of \mathbf{R}^* . In the second step of the Born–Oppenheimer approximation, the electronic energy $E_{\text{el}}(\mathbf{R})$ is used as a potential term in the equation governing the motion of the nuclei (eq. 2.12), described by the nuclear wave function $\psi^{\text{nuc}}(\mathbf{R})$:

$$[\hat{T}_{\text{nuc}} + \hat{V}_{\text{nuc-nuc}} + E_{\text{el}}(\mathbf{R})] \psi^{\text{nuc}}(\mathbf{R}) = E^{\text{BO}}\psi^{\text{nuc}}(\mathbf{R}) \quad (2.12)$$

Solving this final equation allows to obtain E^{BO} , the total energy of the system according to the Born–Oppenheimer approximation.

2.2.2 Hartree–Fock Theory

This section is focused on the calculation of the ground state electron energy (E_0). An important principle in quantum mechanics, the Rayleigh–Ritz variational principle [2], provides a method for finding approximate solutions for E_0 . Specifically, a notable feature of the Hamiltonian is that its expectation value in any state Ψ will always be greater than or equal to the ground state energy, as represented in eq. 2.13.

$$E_0 \leq \frac{\langle \Psi | \hat{H} | \Psi \rangle}{\langle \Psi | \Psi \rangle} \quad (2.13)$$

Hence, starting with an initial assumption for $|\Psi\rangle$ and systematically improving it brings the calculated energy closer to the ground state energy of the system [3].

Initially, let us assume that the number of electrons in our system is N . A first approximation of the wave function, referred to here as the Hartree wave function (Ψ_{H}), can then be represented as the normalized product of the one–particle wave functions (ψ_i), as shown in eq. 2.14:

$$\Psi_{\text{H}}(\mathbf{r}_1, \dots, \mathbf{r}_N) = \psi_1(\mathbf{r}_1) \cdots \psi_1(\mathbf{r}_N) \quad (2.14)$$

Here lies the essence of the Hartree equations (eq. 2.15), where the expectation value is minimized with respect to ψ_i .

$$\left\{ \frac{-\hbar^2}{2m} \nabla^2 + v_{\text{ext}}(\mathbf{r}) + \sum_{j=1}^N \int d^3\mathbf{r}' \frac{e^2}{|\mathbf{r} - \mathbf{r}'|} |\psi_j(\mathbf{r}')|^2 \right\} \psi_i(\mathbf{r}) = \epsilon_i \psi_i(\mathbf{r}) \quad (2.15)$$

Here, the nucleus–electron potential defined in eq. 2.7 acts as an external effective potential for a particle (v_{ext} , detailed in the next section in eq. 2.24), and ϵ_i represents the energy of electron i . Furthermore, these equations indicate that the one–particle Schrödinger equation is solved for an electron in an electrostatic field generated by all electrons, including the electron itself. This leads to the so–called self–interaction, which is incorrectly included in the Hartree equations.

The Hartree equations can be solved using a self–consistent field (SCF) method as follows: starting with an initial guess, eq. 2.15 is solved to obtain a new set of solutions. These new solutions are then used as input for the next iteration, and the process is repeated until the solutions converge, meaning they remain unchanged over subsequent iterations –this is known as reaching self–consistency. From the final solution, the expectation value of the total Hartree energy (E_H) is defined according to eq. 2.16, where V_H , known as the Hartree potential, represents the classical electrostatic interaction. In the next section, this potential will be expressed in terms of the electron charge distribution (eq. 2.25).

$$E_H = \sum_i^N \epsilon_i + V_H + V_{\text{nucI-nucI}} \quad (2.16)$$

The most significant deficiency of the Hartree approach (estimated solution) is its failure to comply with the Pauli exclusion principle, as it does not account for the antisymmetry of the wave function. This issue is addressed by the Hartree–Fock equations, which begin by replacing the wave function defined in eq. 2.14 with a Slater determinant (eq. 2.17), where σ denotes the electron spin.

$$\Psi_{\text{HF}}(\mathbf{r}_1\sigma_1, \dots, \mathbf{r}_N\sigma_N) = \frac{1}{\sqrt{N!}} \begin{vmatrix} \psi_1(\mathbf{r}_1\sigma_1) & \psi_1(\mathbf{r}_2\sigma_2) & \dots & \psi_1(\mathbf{r}_N\sigma_N) \\ \psi_2(\mathbf{r}_1\sigma_1) & \psi_2(\mathbf{r}_2\sigma_2) & \dots & \psi_2(\mathbf{r}_N\sigma_N) \\ \vdots & \vdots & \ddots & \vdots \\ \psi_N(\mathbf{r}_1\sigma_1) & \psi_N(\mathbf{r}_2\sigma_2) & \dots & \psi_N(\mathbf{r}_N\sigma_N) \end{vmatrix} \quad (2.17)$$

Finally, after applying the variational principle, the Hartree–Fock equations are defined according to eq. 2.18.

$$\left\{ -\frac{\hbar^2}{2m} \nabla^2 + v_{\text{ext}}(\mathbf{r}) + v_H(\mathbf{r}) \right\} \psi_i(\mathbf{r}) - \sum_{j=1}^N \int d^3\mathbf{r}' \frac{e^2}{|\mathbf{r} - \mathbf{r}'|} \psi_j(\mathbf{r}')^* \psi_j(\mathbf{r}') \delta_{\sigma_i\sigma_j} = \epsilon_i \psi_i(\mathbf{r}) \quad (2.18)$$

In the same way as in eq. 2.16, the solution of the expectation value for the Hartree–Fock equation is given by eq. 2.19, where E_x corresponds to the energy due to exchange.

$$E_{\text{HF}} = \sum_i^N \epsilon_i + V_H - E_x + V_{\text{nucI-nucI}} \quad (2.19)$$

When comparing the expectation values derived from the Hartree (eq. 2.16) and the Hartree–Fock (eq. 2.19) equations, they differ by only one term, the exchange energy (E_x), which can be

interpreted as follows: The Coulomb repulsion between electrons with the same spin is inhibited by the antisymmetry of the wave function, causing the energy E_0 obtained by Hartree–Fock method to be lower than that from the Hartree method by an amount equal to E_x . Consequently, the Hartree–Fock method accurately calculates the exchange energy but does not account for the effects of the electron correlation, which would further reduce the system energy.

2.2.3 Density Functional Theory

Studying the interactions within a particular system (such as adsorbates on surfaces, molecules, solids, etc.) involves solving eq. 2.10, which requires calculating the properties of electrons in the presence of nuclei fixed in their positions and the influence of other electrons. Density Functional Theory (DFT) offers an alternative method for calculating the electronic properties of many-atom systems. It has been widely used in recent decades due to its simplicity in implementation, precision in results, and efficiency in terms of time and computing resources.

The central concept of DFT is that the energy of an electron system can be expressed in terms of the electron density at a particular point \mathbf{r} in space, $\rho(\mathbf{r})$. The electron energy (E_{el}) is given as a functional of the electron density, denoted as $E_{\text{el}}[\rho]$, such that for a given electron density $\rho(\mathbf{r})$, there is a unique corresponding energy.

The key variable in DFT is $\rho(\mathbf{r})$, which can be expressed as a sum over the states of each particle i , as shown in eq. 2.20.

$$\rho(\mathbf{r}) = \sum_i^N |\psi_i(\mathbf{r})|^2 \quad (2.20)$$

The main achievement of DFT is that all properties derivable from the Hamiltonian are uniquely related to $\rho(\mathbf{r})$. This is demonstrated in Thomas–Fermi theory [4], where the chemical potential μ of the free (non-interacting) electrons in a weakly varying effective potential v_{eff} is given by eq. 2.21

$$\mu = \frac{\hbar^2}{2m} [3\pi^2\rho(\mathbf{r})]^{2/3} + v_{\text{eff}}(\mathbf{r}) \quad (2.21)$$

Because $\rho(\mathbf{r})$ is uniquely related to the effective potential and the number of electrons N through the equation $N = \int \rho(\mathbf{r}) d^3r$, the complete electronic Hamiltonian can be established. In principle, all quantities related to the Hamiltonian could be determined; however, since the dependence is only implicit, this has no practical application.

The importance of applying the variational principle has been previously demonstrated. In this context, the principle can be applied to the electronic energy functional ($E_{\text{el}}[\rho]$), such that the electron density and the exact energy of the ground state are determined by minimizing the energy functional (eq. 2.22):

$$E_{\text{tot}} = \min_{n(\mathbf{r})} \{E[\rho]\} = \min_{n(\mathbf{r})} \{T[\rho] + V_{\text{ext}}[\rho] + V_{\text{H}}[\rho] + E_{\text{xc}}[\rho]\} \quad (2.22)$$

where $V_{\text{ext}}[\rho]$ and $V_{\text{H}}[\rho]$ correspond to the external potential and the energy of the classical electrostatic interaction related to the Hartree energy, respectively, while the term $T[\rho]$ represents the kinetic energy functional of the non-interacting electrons. The term $E_{\text{xc}}[\rho]$ represents the exchange–correlation functional, which includes many-body quantum mechanical effects. Part of the latter functional ($E_{\text{xc}}[\rho]$), as well as the kinetic energy functional ($T[\rho]$), are not known. For this reason, eq. 2.22 cannot be used directly.

If the variational principle is applied in a manner analogous to that used for the deduction of eq. 2.15 and eq. 2.19 in the previous section, the well-known Kohn–Sham equations [5] are obtained, as defined in eq. 2.23.

$$\left\{ -\frac{\hbar^2}{2m} \nabla^2 + v_{\text{eff}}(\mathbf{r}) \right\} \psi_i(\mathbf{r}) = \epsilon_i \psi_i(\mathbf{r}) \quad (2.23)$$

The effective potential of an electron, $v_{\text{eff}}(\mathbf{r})$, is a sum of three potentials: the external potential, $v_{\text{ext}}(\mathbf{r})$; the Hartree potential, $v_{\text{H}}(\mathbf{r})$; and the exchange–correlation potential, $v_{\text{xc}}(\mathbf{r})$, as defined in eq. 2.24, eq. 2.25, and eq. 2.26, respectively.

$$v_{\text{ext}}(\mathbf{r}) = - \sum_I \frac{Z_I e^2}{|\mathbf{r} - \mathbf{R}_I|} \quad (2.24)$$

$$v_{\text{H}}(\mathbf{r}) = \int d^3\mathbf{r}' \rho(\mathbf{r}') \frac{e^2}{|\mathbf{r}' - \mathbf{R}_I|} \quad (2.25)$$

$$v_{\text{xc}}(\mathbf{r}) = \frac{\delta E_{\text{xc}}[\rho]}{\delta \rho} \quad (2.26)$$

As with the Hartree equations, the Kohn–Sham equations can be solved iteratively through a self-consistent procedure. In fact, the Hartree hamiltonian and the Kohn–Sham hamiltonian differ only by the presence of v_{xc} , which is absent in the former. Only one additional term is needed to complete the energy equation according to DFT: the Hartree potential (eq. 2.27), which represents the classical electrostatic energy of the electron charge distribution.

$$V_{\text{H}} = \frac{1}{2} \int d^3\mathbf{r} d^3\mathbf{r}' \frac{e^2 \rho(\mathbf{r}) \rho(\mathbf{r}')}{|\mathbf{r} - \mathbf{r}'|} \quad (2.27)$$

Because V_{H} is implicitly included twice in the calculation of the Kohn–Sham eigenvalue (ϵ_i), it must be subtracted once. In this way, the ground state energy can be expressed as eq. 2.28:

$$E_0 = \sum_i^N \epsilon_i + E_{\text{xc}}[\rho] - \int v_{\text{xc}}(\mathbf{r}) \rho(\mathbf{r}) d^3\mathbf{r} - V_{\text{H}} - V_{\text{nuc} \rightarrow \text{nuc}} \quad (2.28)$$

where ϵ_i is the free particle energy given by the Kohn–Sham equation (eq. 2.23), v_{xc} is the correlation–exchange potential (eq. 2.26), V_{H} is the Hartree potential (eq. 2.27), $E_{\text{xc}}[\rho]$ is the correlation–exchange functional, $\rho(\mathbf{r})$ is the electron density (eq. 2.20), and $V_{\text{nuc} \rightarrow \text{nuc}}$ is the electrostatic interaction between the nuclei (eq. 2.5).

The correlation–exchange functional ($E_{xc}[\rho]$) can be written in a general way as:

$$E_{xc}[\rho] = \int d^3\mathbf{r} \rho(\mathbf{r}) \epsilon_{xc}[\rho](\mathbf{r}) \quad (2.29)$$

Here, ϵ_{xc} corresponds to the exchange–correlation energy per particle at position \mathbf{r} , and it depends on the entire electron density distribution.

The most commonly used functionals in DFT are based on two key approximations: the local density approximation (LDA) and the generalized gradient approximation (GGA), as described by eq. 2.30 and eq. 2.31.

$$E_{xc}^{LDA}[\rho] = \int d^3\mathbf{r} \rho(\mathbf{r}) \epsilon_{xc}^{LDA}(\rho(\mathbf{r})) \quad (2.30)$$

$$E_{xc}^{GGA}[\rho] = \int d^3\mathbf{r} \rho(\mathbf{r}) \epsilon_{xc}^{GGA}(\rho(\mathbf{r})|\nabla\rho(\mathbf{r})) \quad (2.31)$$

In the case of the LDA functional, the correlation–exchange energy (ϵ_{xc}) corresponds to that of a homogeneous electron gas. This functional describes the characteristics of bulk materials and surfaces unexpectedly well. However, as far as absolute energies are concerned, LDA is not sufficiently accurate. This deficiency is mainly due to the fact that this approximation overestimates the bonds. A notable improvement was achieved with the GGA functional, in which the density gradient is also included in ϵ_{xc} . For many chemical reactions the error associated with DFT using GGA is approximately less than or equal to 1.9 meV/atom [6]. In addition, an important source of error in both LDA and GGA approximations arises from the expression of the Hartree potential in eq. 2.27, which includes the interaction of a particle *with itself*, which has no physical meaning. This spurious "self–interaction" error (SIE) is more evident in systems with strongly localized electrons, in particular those containing *d*- and *f*-states, and might lead to a poor estimation of the electronic properties of the material (i.e. band structures, band–gaps and reaction energies). A number of improvements have been proposed to mitigate the SIE. Within such methods, Hubbard corrections [7, 8] and hybrid functionals [9] can be mentioned.

The computational cost of solving eq. 2.23 increases significantly with the number of electrons in the system. To solve larger systems such as metal surfaces among others, whose properties are worthy of being examined at an atomic level, unimaginable supercomputers or superhuman patience would be needed. However, it is known that only valence electrons are involved in chemical reactions, the influence of internal (core) electrons being insignificant. For this reason, their effect can be replaced by an effective potential independent of the valence electrons that will only depend on the nature of the atom. These potentials are called pseudopotentials, which significantly reduce the number of electrons to be taken into account in the calculation, leading to an enormous saving of computational time. The concept of pseudopotential will be defined in detail below.

2.2.4 Pseudopotentials

As is well known, the states of electrons in an atom, considering their roles in bond formation and chemical processes, can be classified into three categories: internal states, which are highly localized and do not participate in chemical bonds; valence states, which are highly delocalized and involved in chemical bonding; and intermediate states, which are localized and polarized but generally do not contribute directly to chemical bonding.

Since the inner shell electrons have little influence on the structural and electronic properties of materials, their explicit representation can be omitted without significant loss of computational accuracy. In principle, it is possible to define an appropriate wave function (Ψ_{pseudo}) that represents the combined effect of the nuclei and the inner electrons on the outer electrons. This wave function should reproduce the valence electron density of the atom when applied to the outer electrons. Such a potential is called a pseudopotential, which, for practical purposes, is conveniently represented by a smooth, nodeless function. This representation facilitates the solution of the electronic problem using standard numerical methods.

The pseudopotential must preserve the atomic properties of the element, including phase changes that occur when electrons scatter through the nucleus. Since these phase changes depend on the angular momentum state, the pseudopotential must be nonlocal, meaning it must include projectors for the different angular momentum states. The general form for a pseudopotential is as follows (eq. 2.32):

$$V_{\text{pseudo}} = \sum_{lm} |lm\rangle V_l \langle lm| \quad (2.32)$$

where $|lm\rangle$ are spherical harmonics, and V_l is the pseudopotential for the angular momentum l .

This treatment, in which only the valence electrons are explicitly considered while the core electrons are incorporated into the nucleus to form a pseudoion, significantly speeds up calculations by reducing the number of basis functions necessary to describe the electronic states. It preserves all the relevant physics in the material behavior.

Finally, in the construction of pseudopotentials, it is required that the charge of the pseudo wave function (Ψ_{pseudo}), integrated up to a certain radius r_c (called the cutoff radius), be equal to the integrated charge of the wave function with all electrons ($\Psi \sim \frac{Z}{r}$), as observed in Fig. 2.1.

2.2.5 van der Waals Corrections

A good description of long-range interactions is necessary to more accurately predict the properties of the systems under study. One of the most common methods to achieve this is by applying a correction to the van der Waals interaction using the method developed by Grimme [10]. There are many variants, with the most recent correction corresponding to DFT-D3. This correction adds a dispersion energy term (E_{disp}) to the Kohn–Sham DFT energy (E_{DFT}) according to the following equation (eq. 2.33):

$$E_{\text{DFT-D3}} = E_{\text{DFT}} + E_{\text{disp}} \quad (2.33)$$

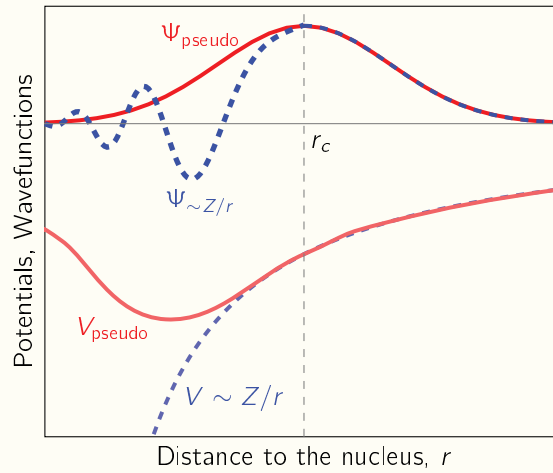


Figure 2.1: Comparison of a wave function ($\Psi \sim \frac{Z}{r}$) in the Coulomb potential of the nucleus ($V \sim \frac{Z}{r}$) (dashed blue line) and a wave function (Ψ_{pseudo}) in the pseudopotential (V_{pseudo}) (solid red line). The real and pseudo representantios coincide beyond the cutoff radius r_c .

where the dispersion energy is calculated according to the following equations (eq. 2.34, 2.35 and 2.36):

$$E_{\text{disp}} = -\frac{1}{2} \sum_{i=1}^N \sum_{j=1}^N \sum_L f_{d,6}(r_{ij,L}) \frac{C_{6ij}}{r_{ij,L}^6} + f_{d,8}(r_{ij,L}) \frac{C_{8ij}}{r_{ij,L}^8} \quad (2.34)$$

$$f_{d,n}(\mathbf{r}_{ij}) = \frac{s_n}{1 + 6(\mathbf{r}_{ij}/S_{R,n}R_{0ij})^{-\alpha_n}} \quad (2.35)$$

$$\mathbf{r}_{ij,L} = (\mathbf{r}_j - \mathbf{r}_i) + \mathbf{R}_{ij} \quad (2.36)$$

where N is the number of atoms, \mathbf{r}_{ij} is the distance vector between atoms i and j , and \mathbf{R}_{ij} is the lattice vector. We consider $R_{0ij} = \sqrt{\frac{C_{8ij}}{C_{6ij}}}$, where the coefficients C_{nij} are computed for each pair of atoms by the geometric mean of atomic terms. The parameters α_6 , α_8 and $S_{R,6}$ are set to 14, 16 and 1, respectively. The values of s_6 , s_8 and $S_{R,6}$ are selected according to the exchange and correlation functional. All necessary parameters are obtained from ref. [11].

2.3 Minimum Energy Path and Nudged Elastic Band Method

To study the reactivity of a system, it is important to find the path of minimum energy that connects two local minima on the potential energy surface, as this represents the most probable path between reactants and products. At any point along the minimum energy path, the force acting on the atoms must be directed along the reaction path. Additionally, the maximum energy value along this path indicates a saddle point on the potential energy surface, which corresponds to a transition state in chemical terms and provides the energy barrier that must be overcome for the reaction to occur. Various methods based on the calculation of the Hessian can be used to obtain transition states.

The method employed to calculate the reaction paths and transition states in this thesis is the NEB (Nudged Elastic Band) method [12–14].

The NEB method algorithm finds the minimum energy path between two geometries or fixed images, defined by the initial state (\mathbf{R}_0) and final state (\mathbf{R}_N), along a trajectory determined by a number of initially proposed intermediate geometries or images ($\mathbf{R}_1, \mathbf{R}_2, \dots, \mathbf{R}_{N-1}$). The vectors \mathbf{R}_i ($i = 0, 1, 2, \dots, N$) are composed of the coordinates defining the positions of each atom considered in the model. The initially proposed path generally differs from the minimum energy path and must be optimized. However, simply relaxing the intermediate images is not sufficient, as unstable geometries might end up in the nearest stable state, such as \mathbf{R}_0 or \mathbf{R}_N . In the NEB method, the images are connected by springs or harmonic oscillators to ensure that they remain constrained between the images that precede and follow them. On each image i ($i = 0, 1, 2, \dots, N - 1$), the net force acting can be defined according to eq. 2.37:

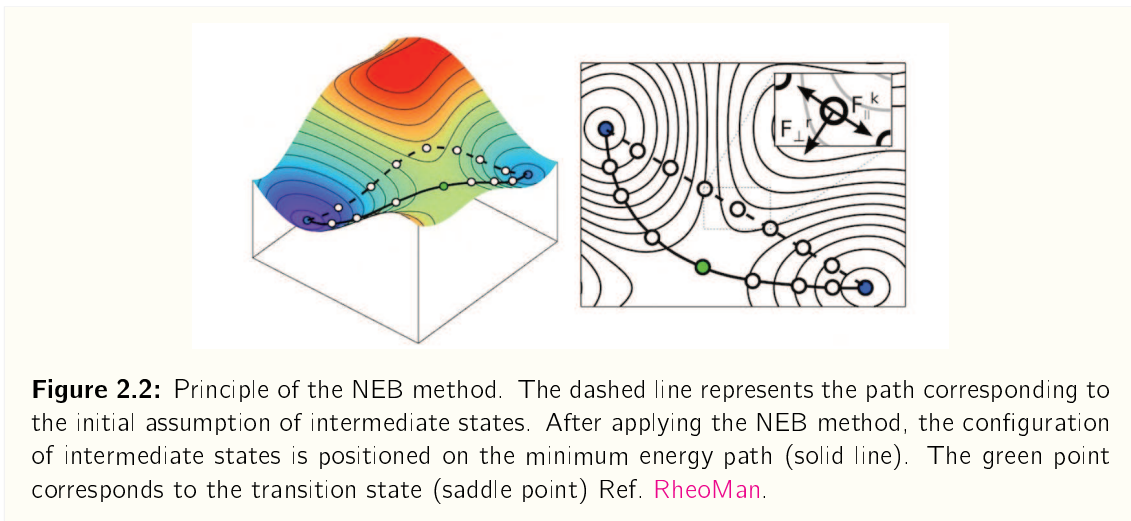
$$\mathbf{F}_i = \mathbf{F}_i^k|_{\parallel} - \mathbf{F}_i^f|_{\perp} \quad (2.37)$$

where the first term represents the net force exerted by the springs on the image i in the direction of the reaction path, while the second term indicates the component of the gradient of the potential surface V perpendicular to the reaction path in the configuration \mathbf{R}_i , which points in the direction of maximum increase of V at that position (see Fig. 2.2). These terms are calculated according to:

$$\mathbf{F}_i^k|_{\parallel} = k[(|R_{i+1} - R_i| - |R_{i-1} - R_i|) \cdot \tau_i] \tau_i \quad (2.38)$$

$$\mathbf{F}_i^f|_{\perp} = \nabla V(\mathbf{R}_i) - [\nabla V(\mathbf{R}_i) \cdot \tau_i] \tau_i \quad (2.39)$$

where k is the constant of the springs joining the images and τ_i is a tangent to the reaction path at image position i . The NEB calculation stops when the sum of these forces is zero (or passes a given convergence value). The method is highly dependent on the initial reaction path chosen, and the difficulty lies in this assumption.



After optimization of the path on the potential energy surface, it is convenient to run a second NEB calculation between the two images adjacent to the energy barrier, thus obtaining a better approximation to the transition state energy. The calculation can be refined with the CI-NEB (Climbing Image – Nudged Elastic Band) method [14]. The highest energy configuration obtained in the NEB calculation, i_{\max} , is shifted along the reaction path in order to maximize its energy, subject to a force defined by:

$$F_{i,\max} = -\nabla V(\mathbf{R}_{i,\max}) + 2\nabla V(\mathbf{F}_{i,\max})|_{\parallel} = -\nabla V(\mathbf{R}_{i,\max}) + 2[\nabla V(\mathbf{R}_{i,\max}) \cdot \boldsymbol{\tau}_i]\boldsymbol{\tau}_i \quad (2.40)$$

Its final configuration is the transition state, or saddle point configuration.

References for Chapter 2

- [1] A. Gross, *Theoretical surface science: A Microscopic Perspective. Advanced Texts in Physics*. Springer, 2003.
- [2] G. Baym, *Lectures on quantum mechanics*. CRC Press, 2018.
- [3] A. Gross, "The virtual chemistry lab for reactions at surfaces: Is it possible? will it be useful?" *Surface Science*, vol. 500, no. 1-3, p. 347, 2002.
- [4] W. Kohn, "Nobel lecture: Electronic structure of matterwave functions and density functionals," *Reviews of Modern Physics*, vol. 71, no. 5, p. 1253, 1999.
- [5] W. Kohn and L. J. Sham, "Self-consistent equations including exchange and correlation effects," *Physical Review*, vol. 140, no. 4A, A1133, 1965.
- [6] K. Lejaeghere, V. van Speybroeck, G. van Oost, and S. Cottenier, "Error estimates for solid-state density-functional theory predictions: An overview by means of the ground-state elemental crystals," *Critical Reviews in Solid State and Materials Sciences*, vol. 39, no. 1, p. 1, 2014.
- [7] V. I. Anisimov, A. I. Poteryaev, M. A. Korotin, A. O. Anokhin, and G. Kotliar, "First-principles calculations of the electronic structure and spectra of strongly correlated systems: Dynamical mean-field theory," *Journal of Physics: Condensed Matter*, vol. 9, no. 35, p. 7359, 1997.
- [8] S. L. Dudarev, G. A. Botton, S. Y. Savrasov, C. J. Humphreys, and A. P. Sutton, "Electron-energy-loss spectra and the structural stability of nickel oxide: An LSDA+U study," *Physical Review B*, vol. 57, p. 1505, 3 1998.
- [9] J. Heyd, G. E. Scuseria, and M. Ernzerhof, "Hybrid functionals based on a screened coulomb potential," *The Journal of Chemical Physics*, vol. 118, no. 18, pp. 8207–8215, 2003.
- [10] S. Grimme, J. Antony, S. Ehrlich, and H. Krieg, "A consistent and accurate ab initio parametrization of density functional dispersion correction (dft-d) for the 94 elements h-pu," *Journal of Chemical Physics*, vol. 132, no. 15, 2010.
- [11] [Online]. Available: <https://www.chemie.uni-bonn.de/pctc/mulliken-center/software/dft-d3>.
- [12] G. Henkelman, B. P. Uberuaga, and H. Jónsson, "A climbing image nudged elastic band method for finding saddle points and minimum energy paths," *Journal of Chemical Physics*, vol. 113, no. 22, p. 9901, 2000.

- [13] G. Henkelman and H. Jónsson, "Improved tangent estimate in the nudged elastic band method for finding minimum energy paths and saddle points," *Journal of Chemical Physics*, vol. 113, no. 22, p. 9978, 2000.
- [14] G. Henkelman, A. Arnaldsson, and H. Jónsson, "A fast and robust algorithm for bader decomposition of charge density," *Computational Materials Science*, vol. 36, no. 3, p. 354, 2006.

Methodology

This chapter introduces details on the various methods used to model and study the chemical systems of interest. The first section presents the DFT computation parameters, including a rationale for the exclusion of Hubbard corrections from the analysis provided in subsequent chapters. This is followed by a description of the methodology used to construct the bond length distribution plots, which offers a valuable insight into the structure of small systems, such as iridium oxide nanoparticles. The plots also provide information that can be compared with existing literature. The next sections address methods related to electronic distribution in the systems, including electrostatic potential, Fermi softness analysis and charge population analysis. Finally, details on the global structure optimization method employed in this thesis for the analysis of some of the nanoparticles are presented.

3.1 DFT calculations

Periodic density functional theory (DFT) calculations were performed using the Vienna ab initio simulation package (VASP 6.2.1) [1, 2]. The core electrons were kept frozen and replaced by pseudopotentials generated by the plane augmented wave method (PAW) [2–4]. The outer shell electrons were treated by means of a plane-wave basis set with a cut-off of 500 eV. The electron–electron exchange and correlation interactions were treated using the generalized gradient approximation in the Perdew–Burke–Ernzerhof (PBE) version [5]. Spin polarizations were considered for all the systems. In order to take into account van der Waals interactions, the DFT–D3 [6] approach of Grimme [7] was used, which consists of adding a semi-empirical dispersion potential to the conventional Kohn–Sham DFT energy. The parametrization of the k-point sampling of the Brillouin zone based on the Monkhorst–Pack grid [8] was considered. For nanoparticles (such as platinum and iridium oxide) in vacuum, only Γ -point calculations were performed. For larger, periodic systems (such as carbon nanotubes and graphene oxide), a proper optimization of k-points was carried out (see chapter 4). The geometry optimizations (ion positions and cell parameters) were performed within the conjugate-gradient minimization scheme, and the convergence criterion was achieved when the total forces were less than 0.04 eV/Å.

3.1.1 Hubbard correction

There is an ongoing discussion about the values of the Hubbard's U parameter that can be used to properly model the electronic repulsion on highly correlated d -states of Ir atoms in iridate compounds. Panda et al. [9] reported that while it is crucial to include spin-orbit coupling interactions in the bulk IrO_2 modeling, it is essentially an uncorrelated system. However, bulk IrO_2 is predicted in his work to have different conducting and magnetic properties in the interval $U = 0 - 8$ eV, but, as indicated, these results should be confirmed experimentally (for example, by low temperature magnetization measurements). In addition, it has been reported both theoretically and experimentally [10, 11] that reducing the thickness of IrO_2 surfaces has an effect on the aforementioned properties. According to these studies, a decrease in the system size leads to a localization of states, and consequently to a change in the electronic (metal to semiconductor) and magnetic (non-magnetic to anti-ferromagnetic) properties, a behavior that would be expected to increase noticeably on nanoparticles. However, to the best of our knowledge, it is difficult to choose a correct U value for the systems considered in this thesis, as no theoretical or experimental studies have been carried out on the electronic and magnetic properties of iridium oxide nanoparticles. An exploration of U values for the Ir-related systems in this thesis is described in Annex A.II. For example, while other studies have used $U = 2$ eV to study iridate compounds (bulk and surfaces) [9, 11], no notable differences concerning relative energies (such as the interaction energy in chapter 8), magnetization values, semiconducting behavior and optimized geometries have been found when applying the Hubbard correction with the same U value (2 eV) on $(\text{IrO}_2)_n$ nanoparticles and $(\text{IrO}_2)_n/\text{GO}$ systems. Furthermore, it was not possible to reproduce the density of states obtained with HSE06 functional for the nanoparticles using Hubbard corrections (in the $U = 0 - 8$ eV range). Under these considerations, Hubbard's U correction was not included in the computation of the various properties of the iridium oxide-related systems in this thesis.

3.2 Bond length distribution

The bond length distribution plots were constructed by mapping the discrete distributions $\{l_j\}$ (i.e. the set of bond lengths found in a given system) into a continuous function $\text{BLD}(l)$. This function was constructed by summing j gaussian functions as in eq. 3.1,

$$\text{BLD}(l) = \sum_j \frac{1}{3n} e^{-\frac{(l-l_j)^2}{2\sigma^2}} \quad (3.1)$$

where the j index counts for each bond, l is the length continuous variable, σ the gaussian root mean square (RMS), and n represents the size of the $(\text{IrO}_2)_n$ system under consideration. The factor $1/3n$ is introduced to allow a comparison of the distributions among different system sizes, as the bound count increases systematically with the number of atoms in the particle ($3n$). Additionally, a RMS value $\sigma = 0.02$ Å was used in order to visually group similar bond types. It should be noted here that the chosen RMS value is notably smaller than the difference between the lengths of any group of bonds, and therefore does not introduce a bias in the data interpretation.

3.3 Electrostatic potentials

The electrostatic potential at each point \mathbf{r} of the cell Ω can be obtained from the DFT calculations as of eq. 3.2,

$$v(\mathbf{r}) = v_{\text{ionic}}(\mathbf{r}) + v_{\text{XC}}(\mathbf{r}) + \int_{\Omega} \frac{\rho(\mathbf{r}')}{|\mathbf{r} - \mathbf{r}'|} d\mathbf{r}' \quad (3.2)$$

where v_{ionic} and v_{XC} are the ionic and exchange–correlation potentials, respectively, and ρ is the electronic charge density. The electrostatic potential maps (i.e. projected into electronic charge density isosurfaces) are useful to identify regions of high and low potentials, which are prone to present electrostatic interactions with other systems of similar chemical nature.

3.4 Fermi softness analysis

The Fermi softness concept, as introduced by Huang et al. [12], was also used to analyze the reactivity of particles and surfaces by considering their frontier electronic bands. This concept has previously been used to accurately describe periodic systems in terms of reactivity indices [13, 14]. The FS method introduces a weight function to modulate the contribution of each electronic band to the possible creation of new bonds, based in their proximity to the Fermi energy. As a result, two quantities of interest are obtained: the spatially localized ($s_F(\mathbf{r})$, eq. 3.3a) and the averaged (S_F , eq. 3.3b) Fermi softness,

$$s_F(\mathbf{r}) = \int_E L(E', \mathbf{r}) w(E') dE' \quad (3.3a)$$

$$S_F = \int_{\Omega} s_F(\mathbf{r}) d^3\mathbf{r} \quad (3.3b)$$

where E is the total energy, $L(E, \mathbf{r})$ the local density of states,¹ \mathbf{r} the position vector and Ω a representation of the cell space. The weight function, w , is taken as the derivative of the Fermi–Dirac distribution function at a non–zero temperature (dFDD) as in eq. 3.4,

$$w(E) = -d\text{FDD}(E) = \beta \frac{e^{\beta(E-E_F)}}{[e^{\beta(E-E_F)} + 1]^2} \quad (3.4)$$

where E_F is the Fermi energy, and $\beta = 1/k_B T$, with k_B being the Boltzmann constant and T a parametric temperature. The value of $k_B T$ was taken as 0.4 eV, as it is the one reported to be optimal for this analysis [12]. Moreover, considering that the electronic density of states (D) can be computed as of eq. 3.5

$$D(E) = \int_{\Omega} L(E, \mathbf{r}) d^3\mathbf{r} \quad (3.5)$$

¹The local density of states L can be computed as following,

$$L(E, \mathbf{r}) = \sum_n \sum_{\mathbf{k} \in \text{BZ}} W_{\mathbf{k}} \delta(E - \epsilon_{n,\mathbf{k}}) \rho_{n,\mathbf{k}}$$

where $W_{\mathbf{k}}$ is the weight of the \mathbf{k} –point, $\rho_{n,\mathbf{k}}$ is the partial charge density and $\epsilon_{n,\mathbf{k}}$ are the energy eigenvalues corresponding to each band n and the \mathbf{k} –point. The information needed to compute L with this expression can be retrieved from VASP calculations.

the averaged Fermi softness S_F is also related to the DOS as shown in eq. 3.6,

$$S_F = \int_E D(E')w(E')dE' \quad (3.6)$$

where it is possible to observe that the quantity S_F can be associated with the integral of electronic states close to the Fermi energy, weighted by the function w .

3.5 Charge population analysis

The charge population analysis of selected systems was conducted using the DDEC6 method, which has been thoroughly described in the relevant literature [15, 16]. This approach yielded valuable insights, enabling the calculation of crucial parameters for the various systems, including atomic charges, bond orders, and overlap populations.

3.6 Genetic algorithm method

In the search for appropriate structures of some systems of interest, such as the iridium oxide nanoparticles, Genetic Algorithm (GA) methods have been used for global structure optimization, as implemented by the ASE software [17, 18]. The GA procedure is shown in Fig. 3.1 and briefly explained in the steps below.

1. 20 initial candidates were generated, by randomly placing the atoms in a unit cell of appropriate dimensions;
2. using VASP as the calculator, the unrelaxed candidates are subjected to a brief geometry optimization (this is known as structure "maturing", and 20 ionic steps were used in this thesis) and total energy calculation;
3. new individuals are created from the existing population by "cut and splice pairing" employing the fitness criteria from Vilhelmsen et al. [19] and the roulette wheel selection scheme described in Johnston [20];
4. some (i.e. with a probability of 0.3) of the generated individuals are subjected to mutation following diverse mutation schema (Mirror, Rattle, Permutations; see [18]);
5. steps 2 – 4 are systematically repeated in loop through several generations of candidates, until a stop criterion is met. For this thesis, the stop criterion was to analyze the twenty most stable structures and verify that they differed by less than 10^{-3} eV while maintaining equivalent geometric configurations.

3.7 Nudged Elastic Band method

The minimum energy paths between reactants and products for the water dissociation reaction were studied by means of the Climbing Image – Nudged Elastic Band (CI-NEB), as implemented by the Henkelman group for the VASP code [21]. The CI-NEB parameters were taken at their default values, and a total of seven images were used in each instance, including initial and final states.

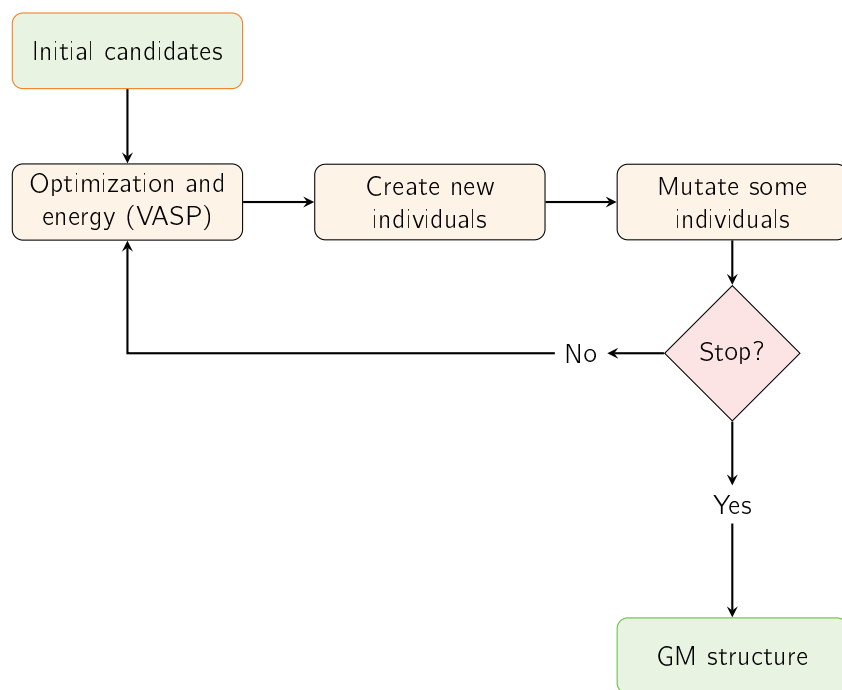


Figure 3.1: Flowchart of the genetic algorithm–based global structure optimization.

References for Chapter 3

- [1] G. Kresse and J. Furthmüller, "Efficiency of ab-initio total energy calculations for metals and semiconductors using a plane-wave basis set," *Computational Materials Science*, vol. 6, p. 15, 1996.
- [2] G. Kresse and D. Joubert, "From ultrasoft pseudopotentials to the projector augmented-wave method," *Physical Review B*, vol. 59, p. 1758, 1999.
- [3] P. E. Blöchl, O. Jepsen, and O. K. Andersen, "Improved tetrahedron method for brillouin-zone integrations," *Physical Review B*, vol. 49, no. 23, p. 16 223, 1994.
- [4] P. E. Blochl, "Projector augmented-wave method," *Physical Review B*, vol. 50, p. 1 795 317 979, 1994.
- [5] J. P. Perdew, K. Burke, and M. Ernzerhof, "Generalized gradient approximation made simple," *Physical Review Letters*, vol. 71, p. 3865, 1996.
- [6] S. Grimme, J. Antony, S. Ehrlich, and H. Krieg, "A consistent and accurate ab initio parametrization of density functional dispersion correction (dft-d) for the 94 elements h-pu," *Journal of Chemical Physics*, vol. 132, no. 15, 2010.
- [7] S. Grimme, "Semiempirical GGA-type density functional constructed with a long-range dispersion correction," *Journal of Computational Chemistry*, vol. 27(15), p. 1787, 2006.
- [8] H. J. Monkhorst and J. D. Pack, "Special points for brillouin-zone integrations," *Physical Review B*, vol. 13, p. 5188, 1976.
- [9] S. K. Panda, S. Bhowal, A. Delin, O. Eriksson, and I. Dasgupta, "Effect of spin orbit coupling and Hubbard U on the electronic structure of IrO_2 ," *Physical Review B*, vol. 89, p. 155 102, 15 2014.
- [10] E. Arias-Egido *et al.*, "Dimensionality-driven metal-insulator transition in spin-orbit-coupled IrO_2 ," *Nanoscale*, vol. 13, p. 17 125, 40 2021.
- [11] X. Ming, K. Yamauchi, T. Oguchi, and S. Picozzi, "Metal-insulator transition and $J_{\text{eff}}=1/2$ spin-orbit insulating state in rutile-based $\text{IrO}_2/\text{TiO}_2$ superlattices," *arXiv:1702.04408 [cond-mat.str-el]*, 2017.
- [12] B. Huang, L. Xiao, J. Lu, and L. Zhuang, "Spatially resolved quantification of the surface reactivity of solid catalysts," *Angewandte Chemie International Edition*, vol. 55, no. 21, p. 6239, 2016.

- [13] X. Deraet *et al.*, "Reactivity of single transition metal atoms on a hydroxylated amorphous silica surface: A periodic conceptual DFT investigation," *Chemistry–A European Journal*, vol. 27, no. 19, p. 6050, 2021.
- [14] X. Deraet *et al.*, "Understanding the reactivity of supported late transition metals on a bare anatase (101) surface: A periodic conceptual DFT investigation," *ChemPhysChem*, vol. 24, no. 6, e202200785, 2023.
- [15] T. A. Manz, "Introducing DDEC6 atomic population analysis: Part 3. Comprehensive method to compute bond orders," *RSC Advances*, vol. 7, no. 72, p. 45 552, 2017.
- [16] N. G. Limas and T. A. Manz, "Introducing DDEC6 atomic population analysis: Part 4. Efficient parallel computation of net atomic charges, atomic spin moments, bond orders, and more," *RSC Advances*, vol. 8, no. 5, p. 2678, 2018.
- [17] A. H. Larsen *et al.*, "The atomic simulation environmenta python library for working with atoms," *Journal of Physics: Condensed Matter*, vol. 29, no. 27, p. 273 002, 2017.
- [18] [Online]. Available: <https://wiki.fysik.dtu.dk/ase/ase/ga/ga.html>.
- [19] L. B. Vilhelmsen, K. S. Walton, and D. S. Sholl, "Structure and mobility of metal clusters in MOFs: Au, Pd, and AuPd clusters in MOF-74," *Journal of the American Chemical Society*, vol. 134, no. 30, p. 12 807, 2012.
- [20] R. L. Johnston, "Evolving better nanoparticles: Genetic algorithms for optimising cluster geometries," *Dalton Transactions*, no. 22, p. 4193, 2003.
- [21] [Online]. Available: <https://theory.cm.utexas.edu/vtsttools/neb.html>.

Carbon surfaces

4.1 Introduction

In the face of environmental degradation, climate change, and energy shortages, it is essential to find efficient and environmentally friendly energy conversion technologies. Fuel cells and batteries are emerging as energy storage and conversion solutions that are less harmful to the environment. They involve electrochemical reactions characterized by slow electron transfer kinetics, which limit device performance. Therefore, it is necessary to incorporate high-performance catalysts to improve the process, with the electrode material being a crucial element. New materials are currently being investigated, among which carbon nanostructures, such as graphene and carbon nanotubes, stand out for their superior properties, availability, and environmental acceptability.

The migration from conventional electrode materials to nanostructured ones with a large surface area presents significant benefits for supercapacitor technology. Carbonaceous materials such as carbon nanotubes (CNTs) are particularly intriguing for electrochemistry and catalysis because their large surface area and chemical stability result in electrodes or catalysts with exceptionally high capacitance and stability, making them highly suitable for supercapacitors. The unique tubular morphology of CNTs has generated considerable research interest. The curvature of their walls causes a shift in the π electron density of the graphene layers from the inner concave surface to the outer convex surface, resulting in an electric potential difference and, consequently, a difference in properties and chemical reactivities between the inner and outer parts of the CNTs. Furthermore, their ion storage capability presents great potential for battery applications.

It is therefore interesting to analyze the behavior of such materials, and one (relatively new) approach to do so is from a theoretical perspective. For this purpose, it is possible to construct rational models of these carbon surfaces based on experimental evidence (such as the chemical composition, the bond lengths and angles, and other physical or chemical properties). A number of software packages are available to make this possible.

The models of carbon materials chosen in this thesis are described in this chapter. The modeling and

the optimization of the parameters are included. The first part of the chapter is dedicated to the modeling of a carbon nanotube surface, while the second part deals with the corresponding description of a graphene oxide surface model. Lastly, some interesting properties of such materials are described, which will be relevant for the following chapters.

4.2 Modeling

4.2.1 Carbon nanotube surface

The *armchair* CNT with chirality (5, 5) was chosen, taking into account its small diameter (6.84 Å) and conductive nature (null band-gap) of its pristine state [1]. The nanotube was modeled using the ASE software [2], imposing periodic boundary conditions in all directions. The resulting unit cell contained 100 carbon atoms, with the nanotube axis following the z -direction (see Table 4.1). In order to properly describe the electronic properties of the CNT and derived systems, a parametrization of the k -point sampling of the Brillouin zone based on the Monkhorst-Pack grid [3] was considered. Taking into account the periodic nature of the nanotube on the z -direction, grids of $(1 \times 1 \times k_z)$ k -points were evaluated, with $k_z = 1 - 9$. According to the results shown in Fig. 4.1a, a $(1 \times 1 \times 3)$ grid was considered a good balance between numerical exactitude and computational efficiency for the calculations of CNT-related systems in this thesis. In addition, taking into account the results in Fig. 4.1b, a sufficient length of 20 Å of the cell parameters in the non-periodic directions of the nanotube a and b (i.e. those perpendicular to that of the CNT axis) was imposed to avoid the interaction of adjacent images, while properly describing the infinite nanotubes under a reasonable computational cost. The CNT model was subjected to gradually increasing axial lengths, allowing the relaxation of existent C-C interactions, and selecting the minimum energy configuration by fitting the cell volume and the computed total energy to the Birch-Murnaghan (B-M) equation of state [4, 5] (see Fig. 4.1c), from where the optimized cell parameters were taken (see Table 4.1).

The atomic positions of the CNT atoms were then optimized. Both optimizations were carried out until the total forces were less than 20 meV/Å, and the cell parameters were kept intact during these calculations. The final CNT surface model, shown in Table 4.1, is in agreement with previous work. In addition, Table 4.2 presents the electrostatic potential and Fermi softness surfaces of the pristine CNT system, both being of great interest for the analysis provided in the following chapters.

4.2.2 Graphene oxide surface

A graphene oxide nanostructure has been generated using the Sinclair and Coveney atomistic model [6, 7]. This method introduces improvements to the Lerf-Klinowski model for GO, where oxidized groups are randomly distributed [8]. Instead, Sinclair and Coveney's machine learning based model is capable of generating graphene oxide structures based on both empirical and theoretical observations. Interestingly, the chosen method can reproduce experimentally observed oxidized and unoxidized domains on the GO surface [6], which are expected to interact differently with other species, such as nanoparticles. In this thesis, hydroxyl and epoxide groups were distributed on one side of a two-dimensional 128 carbon atoms graphene sheet, and then subjected to structural optimization. Carbonyl or carboxyl groups were not included in this model, since their presence is associated with

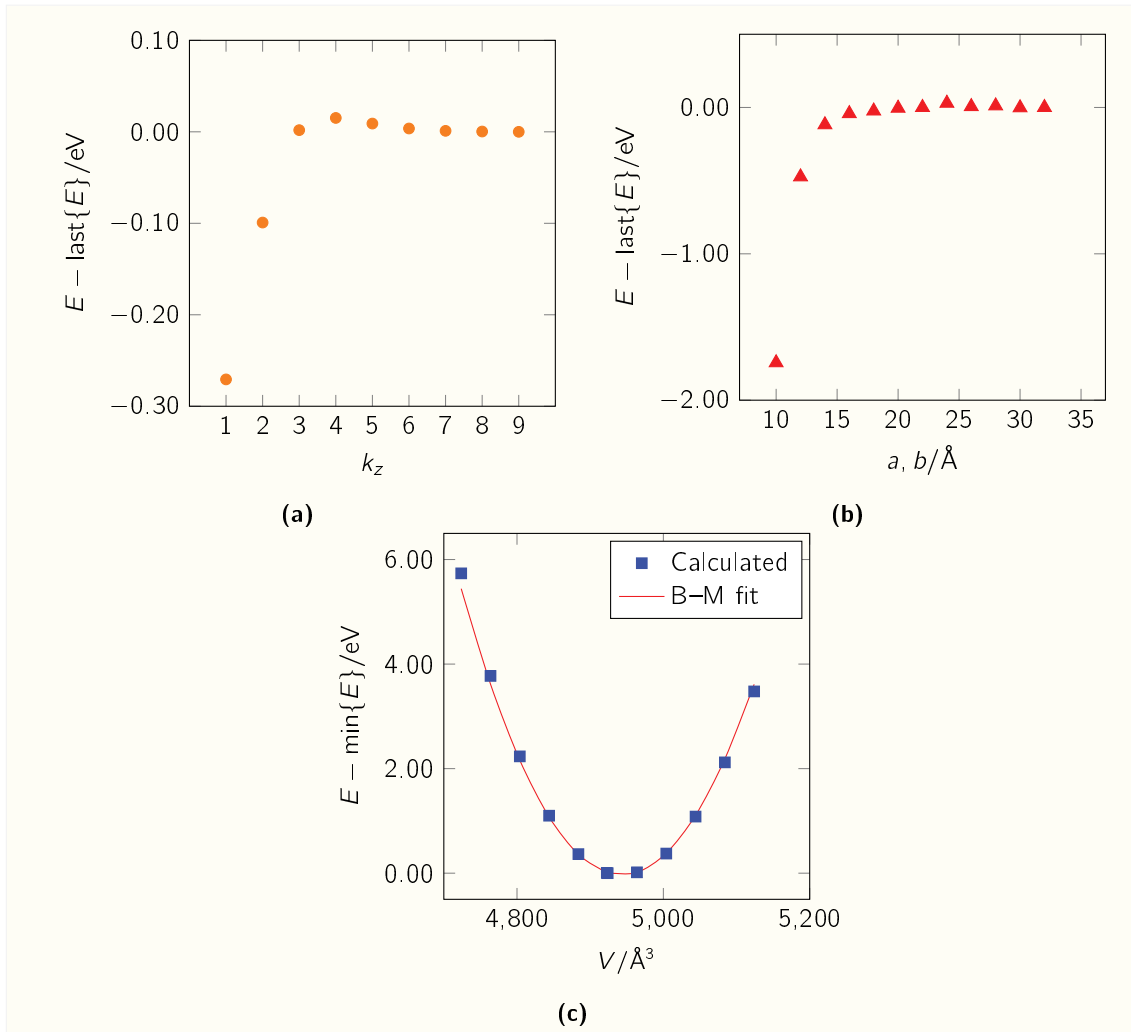
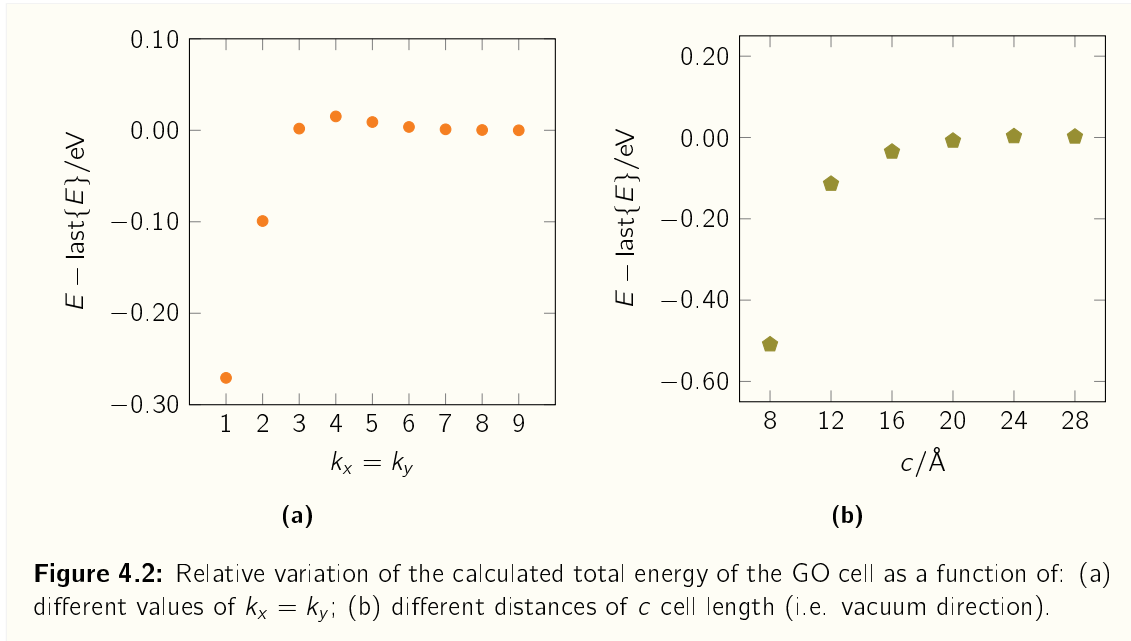


Figure 4.1: Relative variation of the calculated total energy of the CNT cell as a function of: (a) different values of k_z ; (b) different values of $a = b$ cell lengths; (c) unit cell volume (including Birch–Murnaghan fitting).



surface edges or defects. The existence of edges (which would break the two-dimensional periodic boundaries) and defects are out of the scope of this study.

A vacuum separation of 20 \AA was considered sufficient to avoid interactions between graphene oxide sheets of adjacent images. Furthermore, given the estimated dimensions of the cells in this model, a $(5 \times 5 \times 1)$ grid of k-points was deemed an appropriate choice.

As the initial structure was considered far from the expected three-dimensional surface, the geometric optimization was carried out using a series of approximations. The initial atomic positions were relaxed until total forces were less than 100 meV/ \AA . This was followed of an optimization of the cell volume, keeping the tetragonal shape, and allowing the graphene oxide surface to relax until total forces were below 50 meV/ \AA . Both steps were then repeated with a smaller total force criteria of 20 meV/ \AA . Subsequently, the resulting model was subjected to a further examination with regard to the values assigned to the k-point and c cell length (i.e., the vacuum direction) values. According to the results in Figs. 4.2a and 4.2b, the previously selected values have been considered to be well-suited for the purposes of this study. The optimized structure and unit cell parameters of the final GO model are presented in Table 4.1.

4.3 Discussion

Fig. 4.3a illustrates the high-symmetry sites "hollow", "top" and "bridge" on the carbon nanotube surface employed in this thesis. These sites are frequently referenced in literature examining the interaction between nanoparticles and CNTs. Furthermore, an additional site, labeled "shifted-top," proved to be of interest in the study of the deposition of platinum particles (see chapter 6). In the case of the graphene oxide surface, it was considered relevant to study the interaction of nanoparticles with different types of surface oxygen atoms (see chapter 8), given the presence of a dense layer of epoxy and hydroxyl groups covering the surface. Fig. 4.3b illustrates the structure of O^{epoxy} and

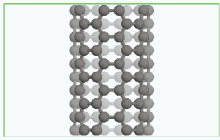

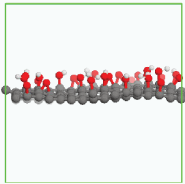
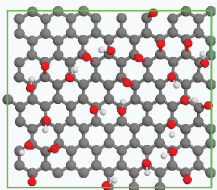
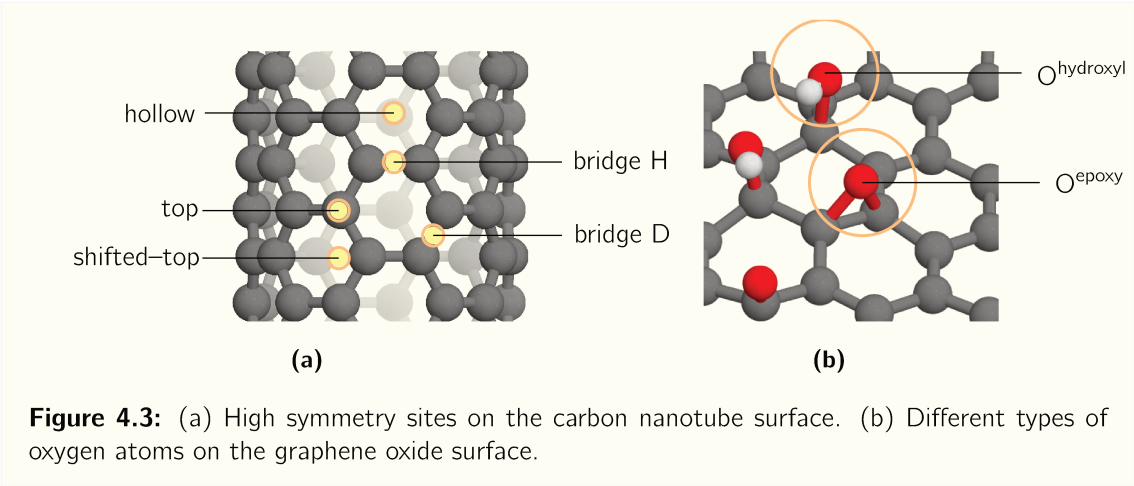
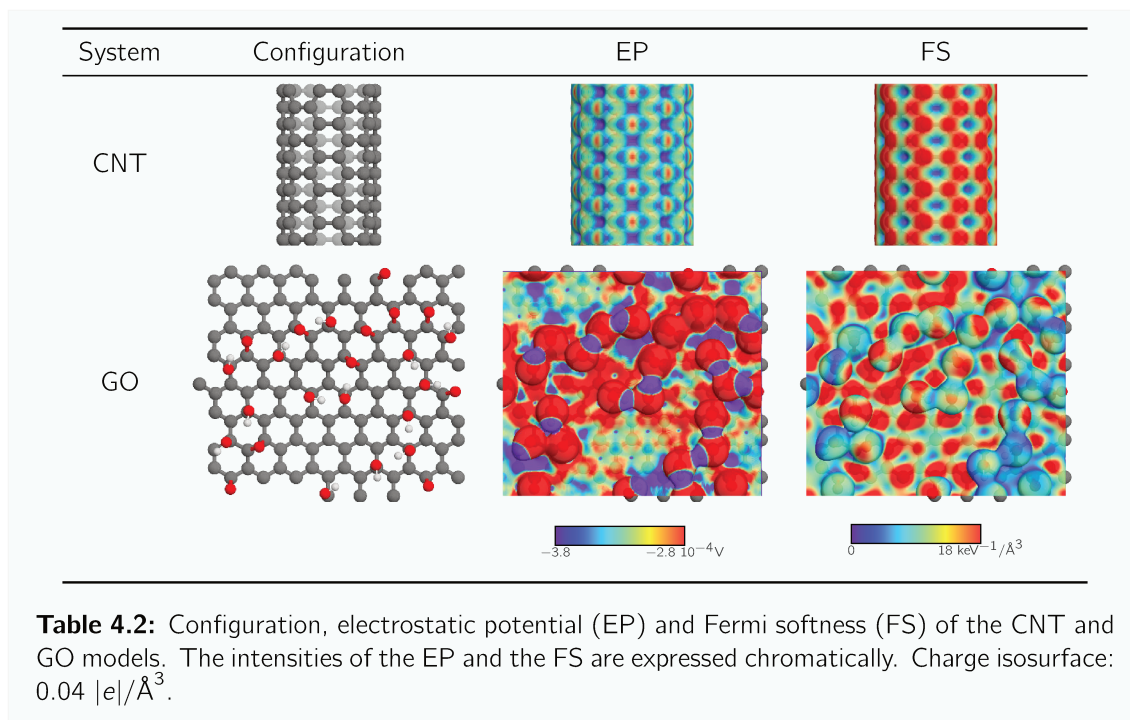
System	Configurations		Cell dimensions
	Side (yz) view	Top (xy) view	
CNT			$20.000 \times 20.000 \times 12.357 \text{ \AA}^3$
GO			$19.743 \times 17.098 \times 20.000 \text{ \AA}^3$

Table 4.1: Geometric configurations and unit cell parameters of the optimized CNT and GO models. Cell limits are shown as green lines.



$\text{O}^{\text{hydroxyl}}$ atoms on the GO.

Furthermore, the electrostatic potential surface and the Fermi softness analysis results for both CNT and GO (see Table 4.2) offer a valuable insight on the chemical reactivity of the carbon surfaces. The EP plots demonstrate a notable discrepancy in the electrostatic potentials of the carbon surfaces. The GO model evinces the most pronounced polarization due to the presence of epoxy and hydroxyl groups, with the regions in proximity to the oxygen atoms exhibiting the highest electrostatic potentials and the lowest ones near the hydrogen atom positions. Conversely, the electrostatic potential differences in the CNT surface are relatively subtle, with the highest values observed near the "bridge" regions, and the lowest values in the vicinity of the "hollow" sites. Based on these observations, it can be anticipated that the carbon nanotube surface will exhibit minimal reactivity with respect to the cleavage of nanoparticles of electrophilic or nucleophilic nature. Such particles would present a stronger interaction with the polarized graphene oxide surface. In turn, the Fermi softness surfaces of the GO and CNT models indicate a similar reactivity towards covalent bond-forming particles. The carbon nanotube



surface present a localization of frontier (i.e. more reactive) electronic states (colored in red) near the "top" and "bridge" sites. For the graphene oxide, the highest Fermi softness values are found at the oxygen's lone-pair electrons regions and the sp^3 -like carbon atoms generated by the presence of oxygen in the graphene layer.

4.4 Summary

On the one hand, a (5,5) carbon nanotube (CNT) model has been constructed by using the ASE software. The different parameters of the proposed model have been optimized in order to achieve an optime accuracy taking into account the computational cost. On the other hand, the code "make-graphitics" was used to generate a graphene oxide (GO) surface based on experimental parameters, including C/O and O/H ratios. This process resulted in the creation of a surface containing aromatic and oxidized regions, which are characterized by the presence of "hydroxyl" and "epoxy" groups. Such model was found to be in alignment with the experimental observations documented in the relevant literature. A remarkable geometrical difference with pristine graphene, especially in the oxidized regions, where a significant geometrical distortion of the sp^2 planar structure was found.

The carbon nanotube and graphene oxide surface models presented in this chapter were utilized to examine the behavior of nanoparticles in the presence of carbon materials. In this analysis, high-symmetry sites and different oxygen atoms of the surfaces, along with qualitative aspects like the electrostatic potential maps (EP) and Fermi softness analysis (FS), were instrumental in providing valuable insights for characterizing these interactions and suggesting potential anchoring configurations. Further details are provided in chapters 6, 7, 8, 9 and 10.

References for Chapter 4

- [1] V. N. Popov, "Carbon nanotubes: Properties and application," *Materials Science and Engineering: R: Reports*, vol. 43, no. 3, p. 61, 2004.
- [2] [Online]. Available: <https://wiki.fysik.dtu.dk/ase/ase/gui/gui.html>.
- [3] H. J. Monkhorst and J. D. Pack, "Special points for brillouin-zone integrations," *Physical Review B*, vol. 13, p. 5188, 1976.
- [4] F. Birch, "Finite elastic strain of cubic crystals," *Physical Review*, vol. 71, no. 11, p. 809, 1947.
- [5] M. Hebbache and M. Zemzemi, "Ab initio study of high-pressure behavior of a low compressibility metal and a hard material: Osmium and diamond," *Physical Review B*, vol. 70, no. 22, p. 224107, 2004.
- [6] R. C. Sinclair and P. V. Coveney, "Modeling nanostructure in graphene oxide: Inhomogeneity and the percolation threshold," *Journal of Chemical Information and Modeling*, vol. 59, no. 6, p. 2741, 2019.
- [7] [Online]. Available: <https://github.com/velocirobbie/make-graphitics>.
- [8] A. Lerf, H. He, M. Forster, and J. Klinowski, "Structure of graphite oxide revisited," *Journal of Physical Chemistry B*, vol. 102, no. 23, p. 4477, 1998.

Platinum and iridium oxide nanoparticles

5.1 Platinum nanoparticles

5.1.1 Introduction

Several theoretical studies on small platinum particles can be found in the literature [1–4]. In these works, the particle models were generated by means of different approaches, being the most frequently found that of the rational proposition of structures followed by geometric optimizations. For very small particles ($n = 1–6$), these rational propositions are usually based in pure geometrical aspects, resulting in one or many of the widely known linear, planar, cubic, tetrahedral, octahedra and bi-pyramidal forms, among others, for each size. For slightly larger particles ($n = 7–13$), however, a more complex analysis of the initially proposed geometries is given. For this size segment, "top-down" and "bottom-up" approaches are useful to represent the break-down of larger structures and assembling of atoms, respectively, to form nanoparticles with the desired size. A similar procedure was followed here to generate initial models of Pt_n ($n = 1–10, 13$) particles, which were then subjected to geometrical optimization using the computational methodology described in Chapter 3. This was done in order to ensure uniformity in the results obtained from the various sections of this work. Consequently, it should be noted that the results concerning Pt_n particle structure and energetics are in great agreement with what has been previously reported, as it is described through this section.

5.1.2 Results and discussion

The geometrical configurations of the optimized Pt_n ($n = 1–10, 13$) nanoparticles are shown in Table 5.1. This table also lists the formation energies (E_{form}), the maximum interatomic distances (r_{max}), the average bond lengths (d_{av}) and average effective coordination numbers (ECN) for each

system. The formation energies were computed as of eq. 5.1,

$$E_{\text{form}} = (E_{\text{Pt}_n} - nE_{\text{Pt}}) / n \quad (5.1)$$

where E_{Pt_n} and E_{Pt} represent the total energies of the nanoparticle and a Pt atom in vacuum, respectively, and n is the number of platinum atoms in the structure. The maximum interatomic distances, on the other hand, were simply computed as of eq. 5.2,

$$r_{\text{max}} = \max \{r_{ij}\} \quad (5.2)$$

where r_{ij} represents the distance between atoms i and j in the Pt_n systems. In addition, average bond lengths and effective coordination numbers were obtained as described in Chapter 3. Fig. 5.1 also presents these results graphically, so they can be visually compared.

As seen from Fig. 5.1a, the formation of all considered nanoparticles is thermodynamically favored, with a gradual decrease in energy with the increasing n and, in general terms, only a small energy difference between systems of the same size. In this figure, orange dots indicate the systems with the lowest formation energy for each size. With respect to particle dimensions, structures as large as ~ 10 Å have been considered, although the most stable configurations showed smaller sizes, with r_{max} values up to ~ 7 Å (see Fig. 5.1b). As expected, the r_{max} values demonstrate a general trend of growth as the number of platinum atoms increases. Furthermore, Fig. 5.1c illustrates that Pt–Pt bond lengths in the particles undergo a gradual increase between 2.34 Å in the Pt_2 dimer to 2.70 Å in the Pt_{13} cluster. The last value remains considerably lower than the corresponding bond length in Pt *fcc* bulk (2.81 Å calculated, 2.77 Å experimental [5]). On the other hand, the averaged effective coordination number of the Pt atoms in the nanoparticles (see Fig. 5.1d) also show larger values with the increasing n . It should be noted from these results, however, that for nanoparticles of the same size, higher ECN values are not necessarily related to more stable systems.

An interesting discussion on the dependence of some of the particle properties, such as bond lengths and formation energies, with the quantity $n^{-1/3}$ is provided in literature [6–9]. As pointed out by the authors of the cited works, such properties are expected to scale linearly with the particle surface-to-volume ratio, S/V , which can then be associated to other quantities of interest. For instance, if r is an estimation of the particle diameter:

- considering that $V \sim r^3$ and $S \sim r^2$, then

$$S/V \sim r^{-1};$$

- if the volume is proportional to the numbers of atoms in the particle, then

$$n \propto V \sim r^3 \quad \therefore \quad r \propto n^{1/3} \quad \therefore \quad S/V \propto n^{-1/3};$$

- if E^{bulk} and E^{surf} are the formation energies of the atoms in the crystal bulk and the particle surface, respectively, then the nanoparticle average energy per atom would be

$$E_{\text{form}} \sim (S \cdot E^{\text{surf}} + V \cdot E^{\text{bulk}}) / n \quad \therefore \quad E_{\text{form}} \propto n^{-1/3} \cdot E^{\text{surf}} + E^{\text{bulk}};$$























Size	Shape	Config.	$E_{\text{form}}/\text{eV}$	$r_{\text{max}}/\text{\AA}$	$d_{\text{av}}/\text{\AA}$	ECN
$n = 1$	atomic		0.00	—	—	0.00
$n = 2$	linear		-1.80	2.34	2.34	1.00
$n = 3$	linear		-2.20	4.71	2.36	1.33
	triangular		-2.36	2.49	2.49	2.00
$n = 4$	linear		-2.42	6.67	2.34	1.50
	square		-2.65	3.47	2.48	2.15
	tetrahedral		-2.64	2.58	2.59	2.99
$n = 5$	linear		-2.95	9.88	2.47	2.15
	planar		-2.88	4.90	2.52	1.50
	pyramid		-2.90	3.66	2.59	2.99
$n = 6$	planar		-3.20	4.88	2.49	2.94
	octahedron		-3.07	3.72	2.64	4.12
	prism		-3.13	3.61	2.60	3.33
$n = 7$	prism-bu		-3.26	4.92	2.60	3.71
	<i>fcc</i> -td		-3.24	4.66	2.62	4.04
$n = 8$	cube		-3.42	4.40	2.60	3.53
	prism-bu		-3.39	5.08	2.64	4.46
$n = 9$	prism-bu		-3.38	5.14	2.63	4.09
$n = 10$	prism-bu		-3.52	6.77	2.64	4.79
	<i>fcc</i> -td		-3.67	5.36	2.70	5.82
$n = 13$	<i>fcc</i> -td		-3.67	5.36	2.70	5.82
$n = \infty$	<i>fcc</i> bulk		-5.50	—	2.81(*)	12.00

Table 5.1: Configurations, formation energies (E_{form}), maximum interatomic distances (r_{max}), average bond lengths (d_{av}) and average effective coordination numbers (ECN) of the studied Pt_n particles. The terms "td" and "bu" stand for "top-down" and "bottom-up", respectively. Platinum *fcc* bulk structure data (taken from [5]) is also shown for comparison. (*) Shortest Pt–Pt distance for *fcc* bulk.

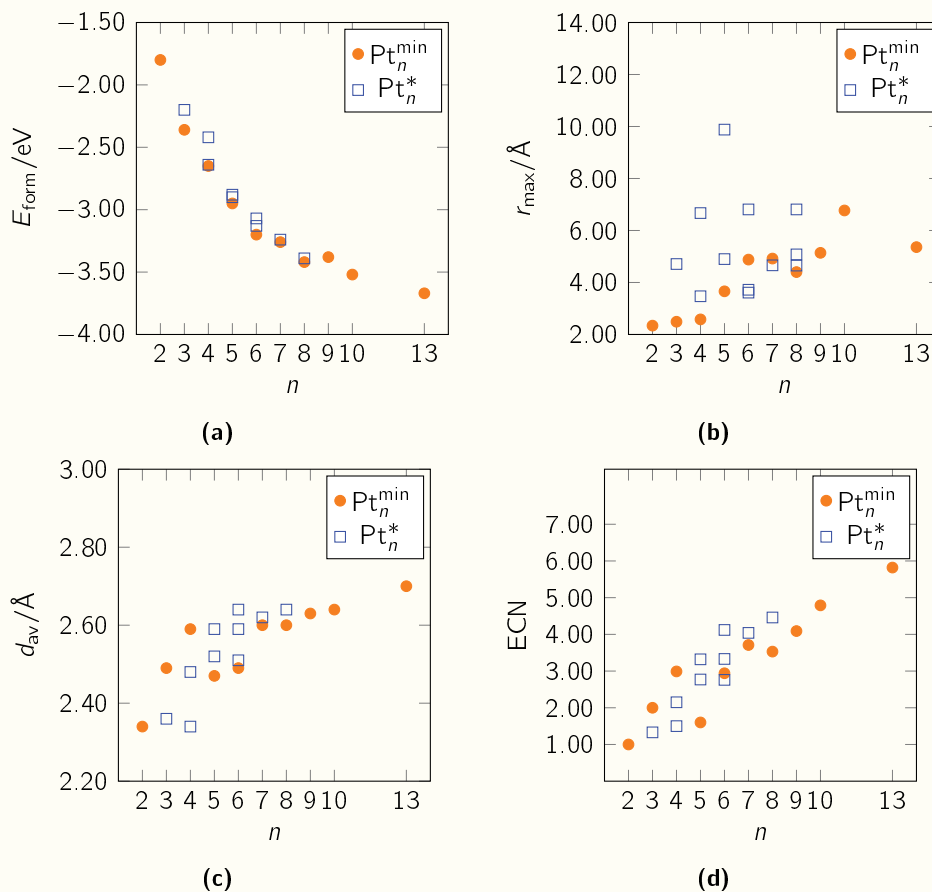


Figure 5.1: Formation energies (E_{form}), maximum interatomic distances (r_{max}), average bond lengths (d_{av}) and averaged effective coordination numbers (ECN) plotted as a function of the particle size (n). For each n , orange dots (Pt_n^{\min}) represent the systems with the lower formation energies, whilst the rest of the structures is shown as blue squares (Pt_n^*).

- similar to the formation energy analysis, if ECN^{bulk} and ECN^{surf} are the effective coordination numbers of the atoms in the bulk and the particle surface, then the averaged value would be

$$ECN \sim (S \cdot ECN^{\text{surf}} + V \cdot ECN^{\text{bulk}}) / n \quad \therefore \quad ECN \propto n^{-1/3} \cdot ECN^{\text{surf}} + ECN^{\text{bulk}};$$

- the lack of neighbors in surface atoms causes an internal pressure on the particle which would have the effect of shrinking its structure with a magnitude proportional to its diameter [8]; therefore

$$d_{\text{av}} \propto r^{-1} \quad \therefore \quad d_{\text{av}} \propto n^{-1/3}.$$

In this line, the particle size could in principle be associated with the computed r_{max} results. However, they do not represent such dependence in a clear manner (see Fig. 5.2a). This is somehow expected, as the r_{max} values depend strongly on the particle shape, which does not present a defined pattern in such small systems. Nevertheless, the linear fitting of the d_{av} and E_{form} results (Figs. 5.2c and 5.2b, respectively) prove that both quantities have indeed a more or less strong dependence on $n^{-1/3}$, which is in agreement with the cited studies. The results of the linear regressions are shown in eqs. 5.3 and 5.4,

$$d_{\text{av}} = 3.118 - 1.007 \cdot n^{-1/3} \quad , \quad R^2 = 0.697, \quad (5.3)$$

$$E_{\text{form}} = -6.041 + 5.398 \cdot n^{-1/3} \quad , \quad R^2 = 0.973. \quad (5.4)$$

It is worth noting that in the case of the formation energies the linear approximation resulted in an outstandingly good fit, regardless of the particle shape. However, the Pt–Pt bond length and formation energy in the limit case $n \rightarrow \infty$ seem to be overestimated (in magnitude) by using this method when compared to *fcc* platinum data [5]: 3.118 Å vs. 2.805 Å (calculated) and 2.775 Å (experimental) for the Pt–Pt bond length, and –6.041 eV vs. –5.50 eV (calculated) and –5.84 eV (experimental) for the formation energy. This would suggest that the Pt_n systems considered here are indeed very distant from the crystal,¹ and larger platinum particles, as those studied by Rivera Rocabado et al. [10], are needed to obtain more accurate results of the bulk system by using the regression method described above.

A summarized comparison of the results obtained here in the study of Pt_n structures with those reported in the literature is provided in Table 5.2. Similar structures have been selected to provide a systematic comparison. However, these configurations do not necessarily correspond to the most stable particles, which can be assessed by comparing Tables 5.1 and 5.2. In the latter, those systems that do not correspond to the most stable configuration (which is observed for $n \geq 4$) are marked with a "(*)" symbol. The results described here are in good agreement with the literature, both energetically and structurally. It is worth noting, however, that the formation energy results obtained here are slightly more negative than those found in other work for similar structures (see Table 5.2). Similarly, the geometric configurations presented here are also somewhat more compact, as suggested by the averaged Pt–Pt bond length values.

¹It is important to exercise caution when extrapolating conclusions or making expectations between nanoparticles and crystals, as this can lead to inaccurate results. The following example illustrates this point: "My 3-month-old son is now twice as big as when he was born. He is on track to weigh 7.5 trillion pounds by age 10."

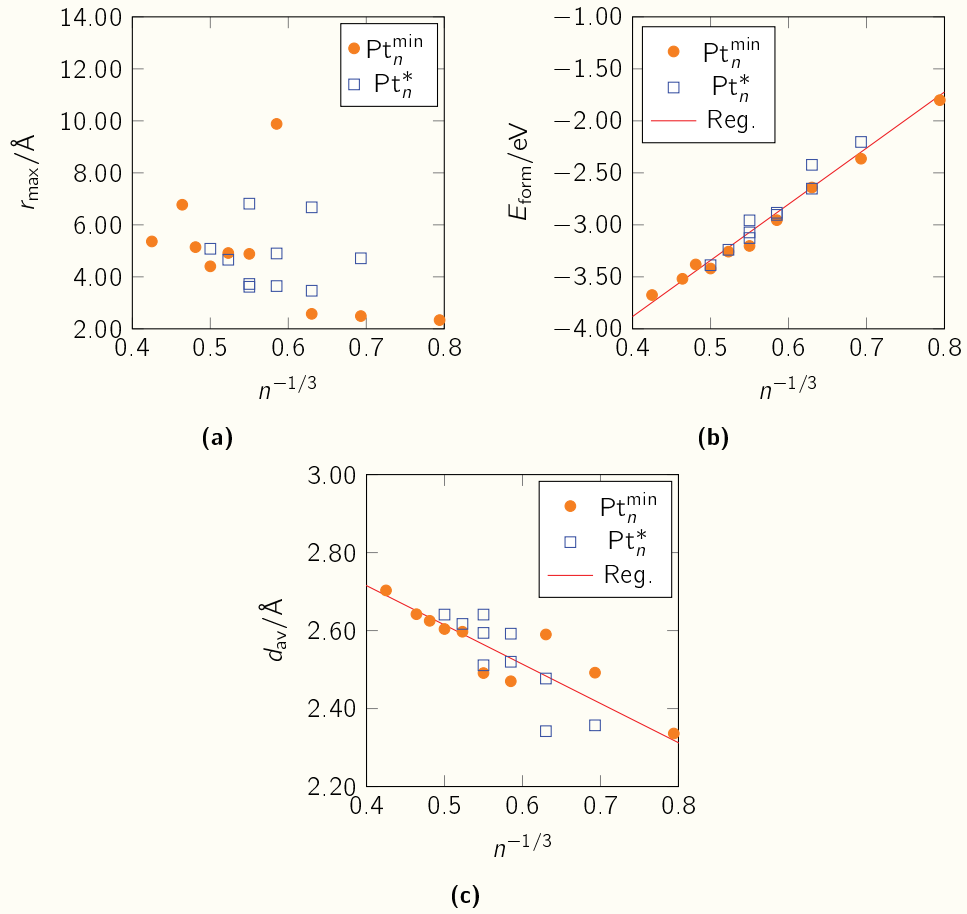


Figure 5.2: Maximum interatomic distances (r_{\max}), formation energies (E_{form}) and average bond lengths (d_{av}) plotted as a function of $n^{-1/3}$. For each n , orange dots represent the systems with the lower formation energies, whilst the rest of the structures is shown as blue squares. The red lines correspond to the linear regressions of E_{form} and d_{av} data, whose parameters are shown in eqs. 5.4 and 5.3, respectively.

Size	This work			Ref. [3]			Ref. [4]			Ref. [2]		
	Shape	$E_{\text{form}}/\text{eV}$	$d_{\text{av}}/\text{\AA}$	Shape	$E_{\text{form}}/\text{eV}$	$d_{\text{av}}/\text{\AA}$	Shape	$E_{\text{form}}/\text{eV}$	$d_{\text{av}}/\text{\AA}$	Shape	$E_{\text{form}}/\text{eV}$	$d_{\text{av}}/\text{\AA}$
$n = 2$	linear	-1.80	2.34	linear	-1.73	2.40						
$n = 3$	triang	-2.36	2.49	triang	-2.35	2.53						
$n = 4(*)$	tetrah	-2.64	2.59	tetrah	-2.64	2.63						
$n = 5(*)$	trig bipyr	-2.90	2.59	trig bipyr	-2.86	2.62						
$n = 6(*)$	prism	-3.13	2.59	prism	-3.04	2.58						
$n = 7(*)$	prism-bu	-3.26	2.60	prism-bu	-3.12	—	semitplanar	-3.17	2.43			
$n = 8(*)$	prism-bu	-3.39	2.64	prism-bu	-3.35	—	prism-bu	-3.23	2.51			
$n = 9(*)$	prism-bu	-3.38	2.63	prism-bu	-3.43	—	pyramid	-3.36	2.51			
$n = 10(*)$	prism-bu	-3.52	2.64	prism-bu	-3.53	—	pyramid	-3.52	2.54			
$n = 13(*)$	fcc-td	-3.67	2.70				pyramid	-3.54	2.62			

Table 5.2: Comparison of Pt_n results with previous work. System sizes marked with (*) do not correspond to the most stable ones found in this work, but those comparable in structure to the reported configurations. The terms "triang", "tetrah", and "trig bipyr" stand for triangular, tetrahedral and trigonal bipyramidal shapes, respectively.

Another interesting aspect of the platinum nanoparticles is related to their electronic distribution, which can be used to search for possible sites of interaction between the particles and the different carbon surfaces. In this line, two qualitative approaches have been taken to analyze the particle models: the electrostatic potentials (EP) and the Fermi softness analysis (FS). These methods are described in Sections 3.3 and 3.4, respectively. Both allow to localize, visualize and even quantify (up to certain limit) the different reactivity regions in the systems, discriminated by the nature of the governing interactions in each model. These interactions can be roughly separated in electrostatic (or coulombic/ionic) in the case of EP, and covalent (or bond-forming) for FS methods.


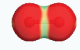
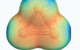

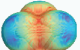
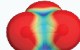
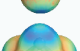
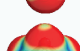



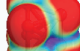







Table 5.3 presents the charge density plots of the selected Pt_n systems, where the EP and the localized FS were projected on their charge isosurfaces. In addition, the averaged Fermi softness values of each system are listed. From the EP maps, it is possible to observe a higher electrostatic potential in the outermost regions of the particles, although this effect is not substantially large when compared to other ionic compounds (as the iridium oxide particles described in Section 5.2). This suggests that such Pt_n systems are not prone to form strong electrostatic (ionic) bindings. On the contrary, the results concerning Fermi softness analysis clearly indicate that the mentioned outermost regions (i.e. opposite to the particle core) have plenty of reactive electronic states (colored in red), very close to the Fermi energy level, and susceptible to forming covalent bonds with substances that exhibit similar chemical properties. Moreover, a rather constant S_F value per atom ($\sim 2 |e|$) is found for $n \geq 4$, regardless of their size and shape, which correspond to the d -states of the Pt atoms. In opposition, due to their smaller size and the lack of inter-bondings, larger S_F values per atom ($\sim 3 |e|$) are observed for $n = 2, 3$ particles.


5.2 Iridium oxide nanoparticles

5.2.1 Introduction

Theoretical research on iridium oxide nanoparticles has been the subject of a number of works which can be cited here [11–13]. However, the generation of the particle models is not deeply detailed in these studies, being limited at best to a selection of reasonable initial structures [12, 14] based, for example, on previous work on titanium, vanadium, silicon and lead oxides [12]. Although these guess are expected to be chemically valid, this exposes a need to investigate further in the structural models used for iridium oxide particles. Some works have addressed this challenge for titanium oxide [15, 16] which represents an interesting case of study since it shares, in one of its common phases, the rutile structure adopted by the iridium oxide in its natural bulk form. Such studies were carried out by using global optimization methods, where the search for global minima (GM) structures on the potential energy surface included genetic algorithm (GA) methods in combination with interatomic potentials (IP), which allowed to find an energy descriptor of each candidate, followed by a DFT optimization of the best candidates in order to obtain a more accurate result in terms of energies and structures.

In this context, in the present chapter both rutile-derived and GM search approaches were used in order to model the iridium oxide nanoparticles. For the latter, GA methods were used to conduct structural GM searches for each of the different nanoparticle sizes. Moreover, considering that the accuracy

Size	Electrostatic potentials	Fermi softness	
		$s_F(\mathbf{r})$	S_F/eV^{-1}
$n = 2$			5.70
$n = 3$			8.56
$n = 4$			7.97
$n = 5$			9.49
$n = 6$			10.81
$n = 7$			13.94
$n = 8$			13.62
$n = 9$			18.42
$n = 10$			20.86
$n = 13$			


-0.50
-0.25 V (Electrostatic potential)



1.0
8.0 keV⁻¹Å⁻³ (Fermi softness)

Table 5.3: Electrostatic potential (EP) and localized Fermi softness (FS) surface plots, and averaged FS values of the most stable Pt_n structures. Charge isosurface: $0.04 |e|/\text{\AA}^3$. The intensity of the EP and the FS is expressed chromatically.

of the IP methods during global optimization is not as good as DFT-based total-energy methods, the GM search was carried out using the same precision level in each instance (i.e. using VASP as the calculator, see chapter 3), thus avoiding a loss of accuracy throughout the global optimization of each nanoparticle. In this regard, it is considered here that this approach represents an improvement of the procedures reported in previous work for similar systems, which we can currently afford thanks to the substantial progress made in computing power in recent years, and enables us to perform a rational, energy-based selection of novel iridium oxide nanoparticle structures.

5.2.2 Results and discussion

Different iridium oxide nanoparticle models were proposed based both in the IrO_2 bulk structure and in GM search with GA methods. As in the case of Pt_n , nanosized –up to ~ 6 nm diameter– configurations were considered, which for stoichiometric iridium oxide can be represented by the formula $(\text{IrO}_2)_n$ with $n \leq 6$. This stoichiometric form was selected over other configurations based in the abundance –and therefore stability– of the macroscopic rutile Ir(IV) oxide.

Structures derived from the IrO_2 bulk (i.e. on which the Ir and O atoms present a similar pattern as in the rutile oxide, in terms of coordination and bond types) were taken following those reported in literature [17, 18]. As with the rest of the systems, the initial configurations were subjected to geometry optimization in order to produce a systematic comparison between the models. For each particle size, the lowest energy configurations were selected, whose resulting structures are presented in Table 5.4. As expected, the optimized configurations did not present substantial differences from the initially proposed models.

On the other hand, the most stable structures of the iridium oxide nanoparticles obtained with the GA methodology are also presented in Table 5.4.

Table 5.4 also list the formation energies values per atom (E_{form}) and maximum interatomic distances (r_{max}). The formation energies were calculated according to eq. 5.5,

$$E_{\text{form}} = [E_{(\text{IrO}_2)_n} - nE_{\text{Ir}} - 2nE_{\text{O}}] / 3n \quad (5.5)$$

where $E_{(\text{IrO}_2)_n}$, E_{Ir} and E_{O} are the total energies computed for the $(\text{IrO}_2)_n$ nanoparticle, an Ir atom and an O atom in vacuum, respectively, and n is the number of IrO_2 units in the particle. In addition, the maximum interatomic distances were computed in the same way as in the case of the Pt_n particles in eq. 5.2. The values obtained for both quantities are also shown in Fig. 5.3 in order to provide a better visual comparison of the results.

Based on the energy results, it is evident that the aggregation of IrO_2 units is favored both in rutile and GA-derived particle models, resulting in an overall stability gain of approximately 0.4 eV and 0.6 eV per atom, respectively, with each additional unit. The energy values change minimally with the increasing particle size in the given size range (see Fig. 5.3a), and are considerably distant ($\gtrsim 0.8$ eV/atom) from the IrO_2 rutile bulk formation energy in the limit case. Comparing the energies obtained for both models, such small iridium oxide particles are therefore more likely to adopt structures as the ones obtained with the GA method, instead of following a rutile-like pattern. A similar behavior was previously reported by Hamad et al. when comparing $(\text{TiO}_2)_n$ ($n = 1 - 15$)




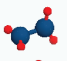

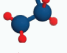
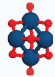
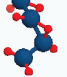

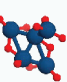
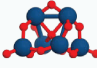
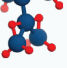
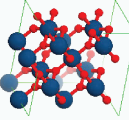
Size	Rutile-derived			GA-derived		
	Config.	$E_{\text{form}}/\text{eV}$	$r_{\text{max}}/\text{\AA}$	Config.	$E_{\text{form}}/\text{eV}$	$r_{\text{max}}/\text{\AA}$
$n = 1$		-4.20	3.39		-4.21	3.39
$n = 2$		-4.62	5.33		-4.82	4.25
$n = 3$		-4.58	5.94		-4.82	6.42
$n = 4$		-4.65	6.46		-4.83	8.41
$n = 5$		-4.65	8.54		-4.84	8.17
$n = 6$		-4.66	9.04		-4.84	8.68
$n = \infty$		-5.67				

Table 5.4: Configurations, formation energies (E_{form}) and maximum interatomic distances (r_{max}) of the most stable $(\text{IrO}_2)_n^{\text{rutile}}$ and $(\text{IrO}_2)_n^{\text{GA}}$ structures. Rutile bulk structure is also shown for comparison.

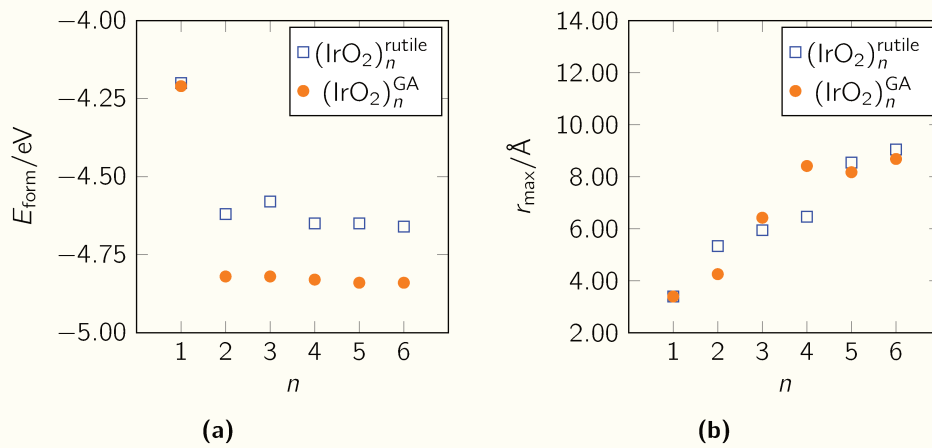


Figure 5.3: Formation energies (E_{form}) and maximum interatomic distances (r_{max}), plotted as a function of the particle size (n).

nanoclusters with anatase-like structures [15]. Although the described energy difference between both types of structures might seem shallow (~ 0.2 eV/atom), it is worth noting that such difference is increasing by 0.6 eV for each additional IrO_2 unit, thus justifying the higher relative stability of GA-derived models of larger particles.

Considering the r_{max} values for each n , the different models are found to present similar nanoparticle sizes (see Fig. 5.3b). Nevertheless, in the following paragraphs, interatomic distances, bond counts and charge population analysis are used in order to provide an insight of the nanoparticles and their differences with the rutile structure.

For the systems under consideration, discrete bond length distributions were determined based purely in geometric aspects. The atomic covalent radius for iridium ($r_{\text{Ir}}^{\text{cov}}$) and oxygen ($r_{\text{O}}^{\text{cov}}$) reported in literature [19], affected by a factor of 133% in order to set a reasonable limit for the interaction (see eqs. 5.6), were used to determine the bond existence between any pair of atoms.

$$r_{\text{Ir-O}}^{\text{max}} = (r_{\text{Ir}}^{\text{cov}} + r_{\text{O}}^{\text{cov}}) \cdot 133\% = 2.75 \text{ \AA} \quad (5.6a)$$

$$r_{\text{Ir-Ir}}^{\text{max}} = (r_{\text{Ir}}^{\text{cov}} + r_{\text{Ir}}^{\text{cov}}) \cdot 133\% = 3.75 \text{ \AA} \quad (5.6b)$$

$$r_{\text{O-O}}^{\text{max}} = (r_{\text{O}}^{\text{cov}} + r_{\text{O}}^{\text{cov}}) \cdot 133\% = 1.76 \text{ \AA} \quad (5.6c)$$

Fig. 5.4 depicts the distribution of bond lengths for both the rutile and GA-derived nanoparticles. The IrO_2 rutile bulk structure bond length distribution is also shown in both cases for comparison. This structure, represented by the black dashed line in both Fig. 5.4a and 5.4b, exhibits two types of iridium–oxygen bonds with very similar lengths (1.98 Å and 2.01 Å) displayed as a single, overlapped peak, as well as two different types of Ir–Ir lengths associated to the (001) (3.19 Å) and (111) (3.59 Å) cell directions. Similar distances are found for the larger nanoparticles ($n \geq 3$). As seen on Table 5.4, their structures present oxygen atoms in "bridge" positions, i.e. coordinating with two Ir atoms (O_{brg} , see the example in Fig. 5.5), with Ir–O lengths values that resemble the ones found in the bulk structure. The slight shift to lower values found in nanoparticles for Ir– O_{brg} distances (1.8 – 2.1 Å) with respect to the Ir–O lengths in bulk structure can be explained by the fact that, in the latter, each oxygen atom simultaneously coordinates with three iridium atoms, while the two-bond environment of " O_{brg} " atoms allows them to interact at shorter distances. The larger nanoparticles ($n \geq 3$) also present pairs of Ir atoms located at relative distances which are comparable to the ones present in the bulk structure (Ir–Ir^{long}, see Fig. 5.5), recalling the distances between Ir atoms in both the (001) and (111) directions. In the last case, rutile and GA-derived particles show a differential behavior with respect to the (111) bond length. The latter presents increased Ir–Ir lengths, while in the formers these distances are reduced, thus suggesting an ability of GA-derived models to form less constrained geometries.

Although the bond length distribution in the nanoparticles becomes more similar to that of the bulk structure with the increasing nanoparticle size, their molecular nature also introduces specific bondings associated with chemical interactions not present in the crystalline structure of the oxide. These new interactions correspond to Ir=O ("oxo") bonds, and direct ("short") Ir–Ir bonds (see Fig. 5.5).

The distribution of Ir=O bonds is shown in Fig. 5.4 as combined peaks at 1.72 Å, with a clear

difference compared to the group of Ir–O bond lengths. As the nanoparticles grow in size, the relative number of "oxo" groups decreases in each nanoparticle because more oxygen atoms take inter-bonding positions between other iridium atoms. Moreover, "short" Ir–Ir bonds are observed in the nanoparticles only, with values in the range 2.30 Å to 3.00 Å. Among them, the shorter bonds in GA-derived models (between 2.30 Å and 2.40 Å) correspond to Ir–Ir interactions without participation of other O or Ir atoms, while the larger bonds (2.50 Å to 2.60 Å) involves a third atom. The "short" Ir–Ir bond distances values are close to those found in the metallic iridium bulk (2.715 Å [20], depicted as a dashed light blue line in Fig. 5.4), which could suggest that the formation of the $(\text{IrO}_2)_n$ particles involves the creation of "core-shell-like" patterns (particles with interacting Ir atoms, and surrounded by O species), more markedly in the case of GA-derived models.

Despite the existence of some similitude in bond length distributions of rutile and GA-derived models, two main differences are also worth to mention here. First, the different bond regions are more defined for GA-derived configurations, suggesting, in one hand, that they present more consistently similar chemical environments, and, in the other hand, that these structural models could be explained by a "bottom-up" concatenation of similar units. Secondly, the predominance of Ir=O ("oxo") bond quantities over the Ir–O bonds in the GA-derived particles (see Fig. 5.4b), in opposition with the proportion found in rutile-derived models (see Fig. 5.4a). While the number of "oxo" bonds does not seem to have an impact in the formation energy when considering rutile and GA-derived structures separately, it might explain the energy difference between these groups as described before. Therefore, this description could be in line with what has been suggested in previous research on metal oxide nanoparticles [21], regarding the number of terminal Ir=O groups and their effect on the stability of the clusters.

The results described above clearly demonstrate the existence of significant differences between the nanoparticles and the IrO_2 rutile bulk structure with respect to the chemical bonding of their atoms. Moreover, the amount of different types of bonds (Ir–O, Ir=O and Ir–Ir) on the particles and the bulk are well-related to the atomic net charge of the involved Ir atoms. For these structures, Table 5.5 shows the atomic net charge for each Ir atom (q_{Ir}) along with the number of bonding neighbours discriminated by type of bond: Ir=O, Ir–O and Ir–Ir (c_{oxo} , c_{brg} and c_{Ir} , respectively). A multiple linear regression of $q_{\text{Ir}} = q_{\text{Ir}}(c_{\text{oxo}}, c_{\text{brg}}, c_{\text{Ir}})$ is found to have a reasonably good fit (see eqs. 5.7) for both rutile and GA-derived configurations.²

$$q_{\text{Ir}}^{\text{rutile}} = -0.03 + 0.32 \cdot c_{\text{oxo}} + 0.23 \cdot c_{\text{brg}} - 0.03 \cdot c_{\text{Ir}} \quad , \quad r^2 = 0.8507 \quad (5.7a)$$

$$q_{\text{Ir}}^{\text{GA}} = -0.06 + 0.41 \cdot c_{\text{oxo}} + 0.24 \cdot c_{\text{brg}} - 0.12 \cdot c_{\text{Ir}} \quad , \quad r^2 = 0.9258 \quad (5.7b)$$

Differences arise, once again, between the two types of models. Based on the regression coefficients, for GA-derived systems both Ir=O and Ir–O bonds have a charge depletion effect on the Ir atom, showing the "O_{oxo}" species the major impact on charge withdrawing, while, in turn, Ir–Ir bonds have a small buffer effect on the charge depletion induced by O atoms. For rutile-derived systems, however, the electronic depletion effect on Ir atoms due to Ir=O and Ir–O bonds is also observed, but with a smaller coefficient value for each. Additionally, Ir–Ir bonds would have no significant effect as the

²In order to have common points between both regressions, and therefore to ensure a proper comparison, bulk IrO_2 system data and the zero values (0, 0, 0) were included. Standard errors for rutile and GA-derived models regressions, respectively (given in the same order as the coefficients in eqs. 5.7): (0.09, 0.05, 0.02, 0.02), (0.09, 0.04, 0.02, 0.03).

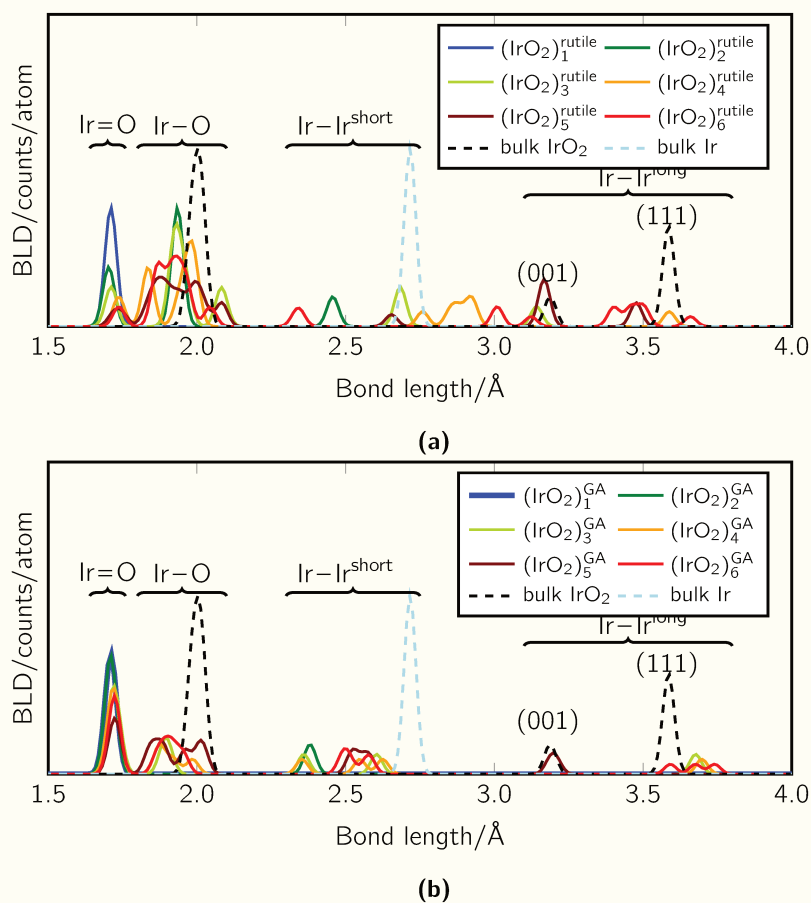


Figure 5.4: Distribution of bond lengths for $(\text{IrO}_2)_n^{\text{rutile}}$ (a) and $(\text{IrO}_2)_n^{\text{GA}}$ (b). Distributions from iridium oxide and metallic iridium bulks are also shown in dashed lines for comparison. Domains for different types of bonds (Ir=O, Ir-O, and Ir-Ir) are indicated as well.

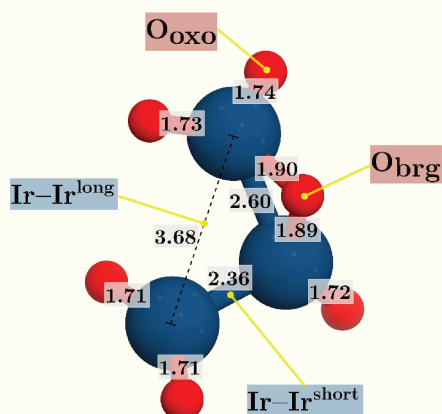


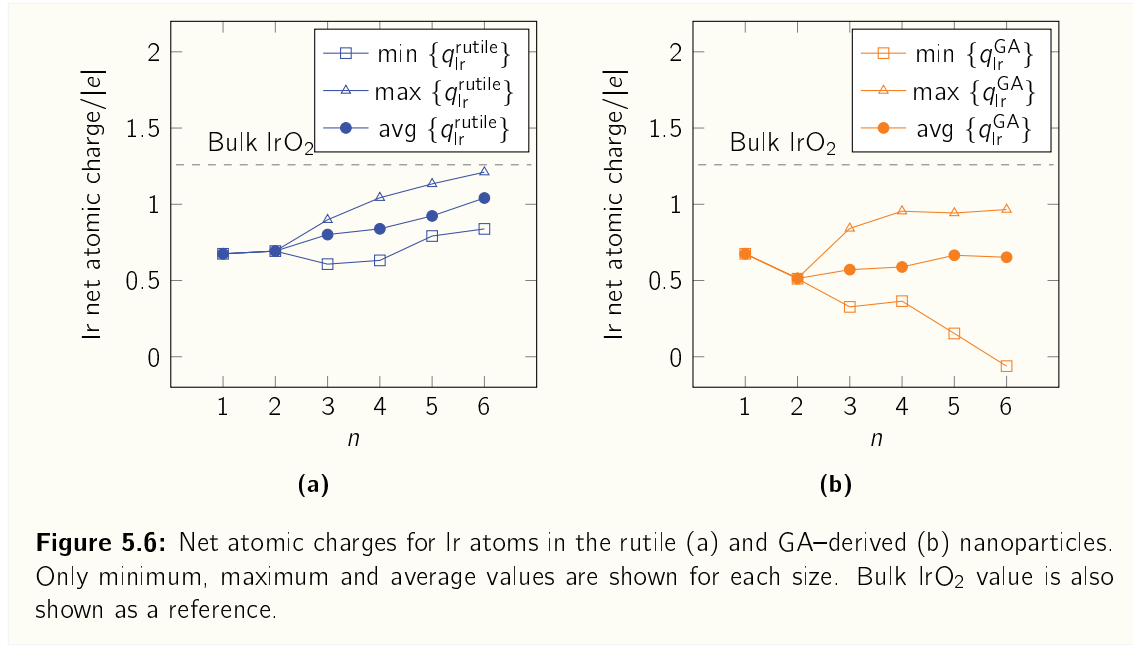
Figure 5.5: Interatomic distances (gray background), and different types of oxygen atoms (pink background) and iridium bondings (light blue background) for the $(\text{IrO}_2)_3^{\text{GA}}$ particle. This example helps to illustrate the diverse types of bondings in the nanoparticles.

Size	Rutile-derived				GA-derived			
	$q_{\text{Ir}}/ e $	c_{oxo}	c_{brg}	c_{lr}	$q_{\text{Ir}}/ e $	c_{oxo}	c_{brg}	c_{lr}
$n = 1$	+0.68	2	0	0	+0.68	2	0	0
$n = 2$	+0.51	2	0	1	+0.69	1	2	1
	+0.51	2	0	1	+0.69	1	2	1
$n = 3$	+0.54	2	0	1	+0.90	1	3	1
	+0.33	1	1	2	+0.61	0	2	2
	+0.84	2	1	1	+0.90	1	3	1
$n = 4$	+0.36	1	1	2	+1.04	1	3	2
	+0.52	2	0	1	+1.04	1	3	2
	+0.95	2	1	1	+0.64	0	3	3
	+0.52	1	2	2	+0.64	0	3	3
$n = 5$	+0.94	2	1	1	+0.79	0	3	1
	+0.15	0	3	3	+1.13	1	3	1
	+0.77	1	2	1	+0.93	0	4	0
	+0.66	1	2	2	+0.92	0	4	0
	+0.80	1	2	1	+0.84	1	3	0
$n = 6$	-0.06	0	2	3	+1.08	0	4	0
	+0.96	2	1	1	+1.07	0	4	0
	+0.97	2	1	1	+0.84	0	4	0
	+0.91	2	1	1	+0.85	0	4	0
	+0.22	0	2	3	+1.21	1	3	0
	+0.92	2	1	1	+1.20	1	3	0
$n = \infty$	+1.26	0	6	0				

Table 5.5: Iridium atomic net charges (q_{Ir}) and number of bonding neighbours (c_{oxo} , c_{brg} and c_{lr}) discriminated by type of bond (Ir=O, Ir–O and Ir–Ir respectively) for each Ir atom of the nanoparticles (both rutile and GA-derived) and bulk IrO₂ rutile. The existence of bondings was determined by using the DDEC6 overlapping population results, where an overlap charge of at least 0.1 $|e|$ was required to define a possible bond between any pair of atoms.

corresponding regression coefficient is not statistically different from zero.

The iridium atomic charge also behaves differently in bulk and in the nanoparticles. Due to symmetry, a single charge value is found for Ir in the rutile structure (+1.26 $|e|$). For the GA-derived nanoparticles, a more heterogeneous set of values is found for Ir atoms, ranging from -0.06 $|e|$ to +0.97 $|e|$. This inhomogeneity grows with the particle size (see Fig. 5.6b), and it is caused by the existence of chemically different Ir atoms as previously described. Atomic net charges of Ir in rutile-derived models (Fig. 5.6a), in turn, show a clearly increasing trend and a greater homogeneity. In this case, the iridium charge values approximate to that of the IrO₂ bulk with the increasing size of the particle. As seen from Table 5.5, and in agreement with the regression models, the highest atomic charges for each particle corresponds to the most oxidized Ir, which are found to have the largest amount of bonds with O atoms, and the greatest number of "O_{oxo}" species. In the same way, the lowest atomic charges are related to the least oxygen-coordinated Ir atoms for each nanoparticle. In addition, rutile-derived models present, in general terms, fewer Ir=O ("oxo") and Ir–Ir bonds with respect to their GA-derived pairs. The difference on the number of intermetallic bondings becomes considerable



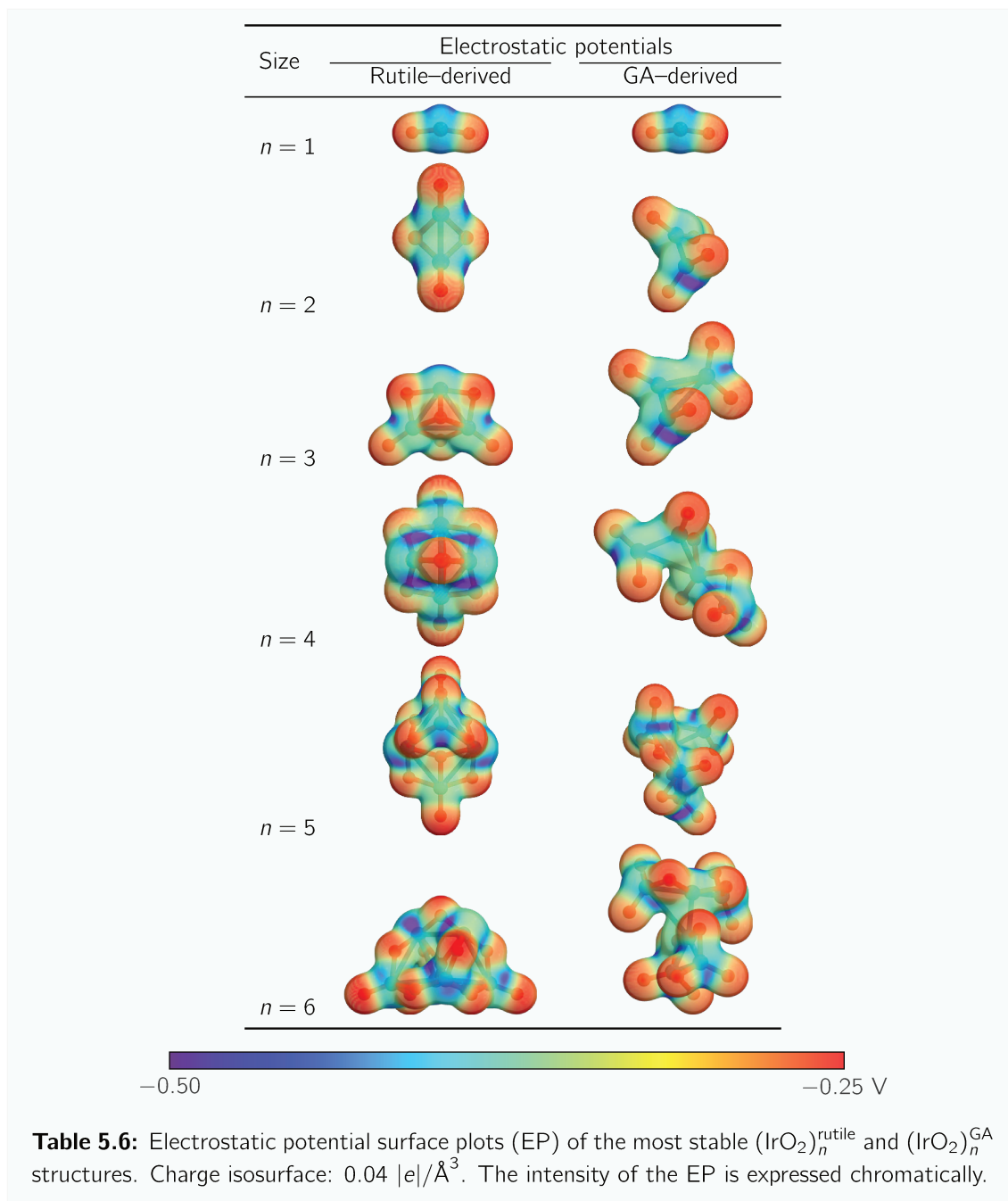
for $n \geq 5$ systems, practically disappearing on rutile-derived configurations. These observations strengthens the "core-shell-like" model of the GA-derived particles.

Despite having the same stoichiometry, the GA-derived particles exhibit less oxidized Ir atoms compared to both the rutile-derived ones and the IrO₂ bulk, due to differences in their structure and their specific chemical environments, as described in this section. In this regard, the variety of atomic charges among the different iridium atoms might have an interesting impact on the reactivity of the nanoparticles.

While the structures of the IrO₂ and Ir₂O₄ nanoparticles described here have been previously reported [11], the remaining Ir₃O₆, Ir₄O₈, Ir₅O₁₀ and Ir₆O₁₂ configurations are, to the best of our knowledge, introduced for the first time in this work.

Iridium oxide "core-shell-like" structures, as the ones suggested here (particularly for GA-derived models), have been experimentally described in recent studies. For example, Tomihara et al. [22] reported small iridium oxide cluster anions Ir_nO_m[−] ($n = 5 - 8$), examined by means of ion mobility mass spectrometry (IMMS) and theoretical calculations, whose structures were found to present O atoms preferentially bonded to the terminal sites of Ir cores. Additionally, Lettenmeier et al. [23, 24] studied different nanosized (~ 2 nm) iridium structures showing a metallic Ir core surrounded by a thin layer of Ir⁺³/Ir⁺⁴ oxides/hydroxides, which presented enhanced oxygen evolution reaction (OER) activity.

As in the case of the Pt_n systems, electrostatic potentials and Fermi softness analysis was performed on the iridium oxide nanoparticles to inquire on their electronic properties. Table 5.6 presents the charge density plots of rutile and GA-derived systems, with the computed electrostatic potentials projected on their charge surfaces. From these representations, it is possible to observe that a lower potential can be found near O atoms in all cases, while regions close to Ir atoms show the opposite effect. This can be explained by the higher electron affinity of the oxygen atoms, which tend to attract electronic charge from the nearby zone.



The localized Fermi softness can be represented graphically in the same way as the electrostatic potentials. In this case, FS plots allow to visualize the surface reactivity of the particles based on the energy of their electronic states. Table 5.7 presents the $s_F(\mathbf{r})$ plots and S_F values for the studied nanoparticles. The $s_F(\mathbf{r})$ plots unveil a higher reactivity nearby Ir atoms, which can be easily attributed to the valence electronic d -states of the metal. On the contrary, the O atoms present a much smaller overall reactivity, with weak exceptions at non-bonding (i.e. electron lone-pairs) regions, which states are also expected to present energies near the Fermi level.

On the other hand, S_F values for both rutile and GA-derived models increase evenly for $n \geq 2$, which can be associated with an increasing amount of d -states from Ir atoms with the increasing particle size. In addition, for the rutile-derived particles, S_F grows by a factor of ~ 2 with each additional IrO_2 unit, while a smaller factor of ~ 1.7 is found for GA-derived models under the same approach. Thus, according to what has been described by means of FS qualitative and quantitative analysis, a higher capacity to form covalent bonds with chemically similar structures could be expected from rutile-derived nanoparticles when compared to their GA-derived peers.

5.3 Summary

Both platinum and iridium oxide nanoparticle models are introduced and described in the present chapter. Energetic, geometric and electronic aspects have been analyzed in depth to understand the principal characteristics of the nanoparticles.

The formation platinum nanoparticles, Pt_n ($n = 1 - 10, 13$), was found to be thermodynamically favored, resulting in significant differences with the *fcc* crystal structure in terms of energy, bond lengths, and coordination numbers. Furthermore, the analysis of electrostatic potential and Fermi softness surfaces indicates that such Pt_n systems are more likely to form covalent bonds with substances that exhibit similar chemical properties.

With regard to the iridium oxide nanoparticles, particular attention has been paid to the generation and characterization of the $(\text{IrO}_2)_n$ ($n = 1 - 6$) nanoparticle models –obtained by means of Genetic Algorithm (GA) methods– and the comparison with those found in literature. The results suggested that the formation of "core-shell-like" patterns (particles with interacting Ir atoms, and surrounded by O species) are preferred in such small oxide systems. Moreover, the amount of different types of bonds (Ir–O, Ir=O and Ir–Ir) on the nanoparticles and the bulk system is well related to the atomic net charge of the involved Ir atoms.

The analysis conducted on platinum and iridium oxide nanoparticles in the gas-phase enables the selection of adequate models for further investigation of their interaction with carbon surfaces.

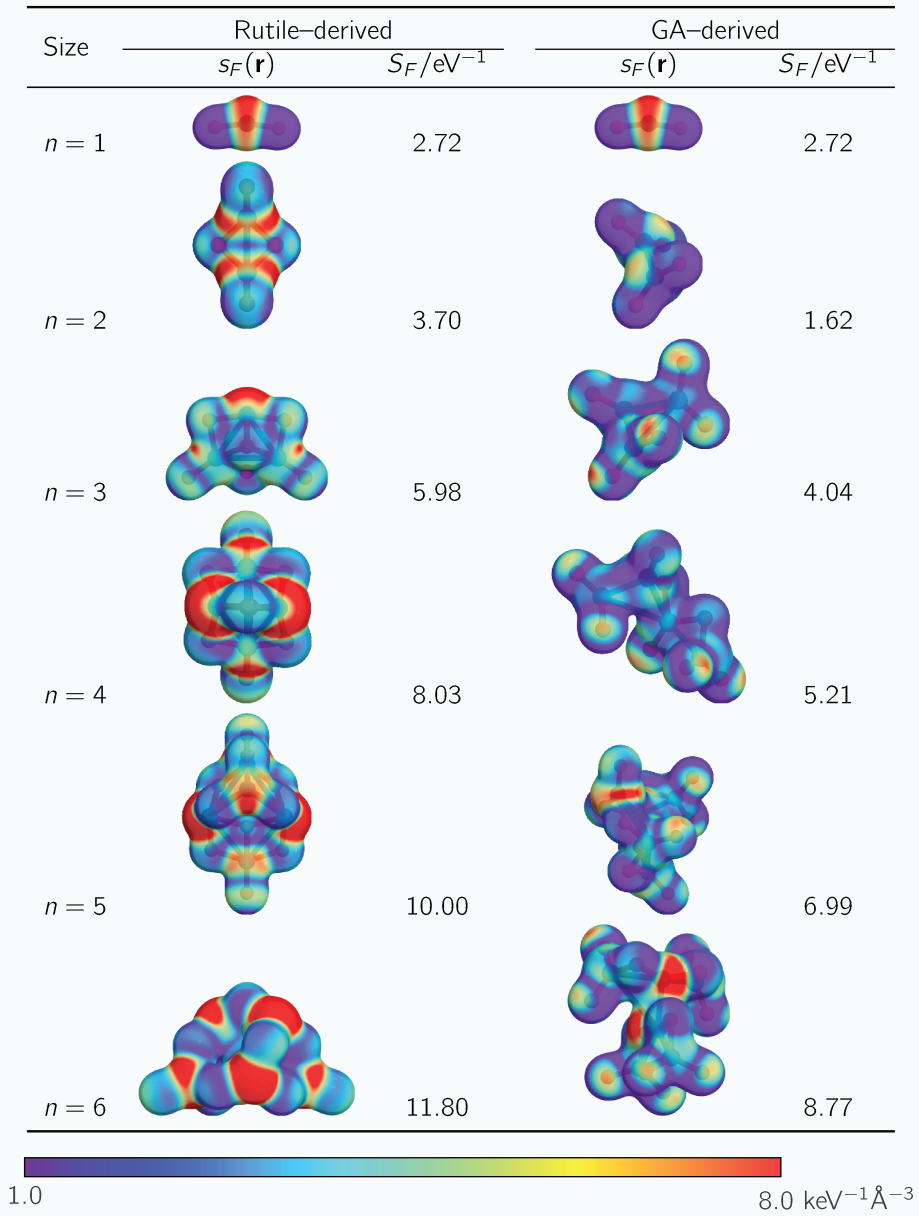


Table 5.7: Spatially localized ($s_F(\mathbf{r})$) and averaged (S_F) Fermi softness plots and values, respectively, of the most stable $(\text{IrO}_2)_n^{\text{rutile}}$ and $(\text{IrO}_2)_n^{\text{GA}}$ structures. The intensity of the FS is expressed chromatically. Charge isosurface: $0.04 |e|/\text{\AA}^3$.

References for Chapter 5

- [1] A. Sebetci and Z. B. Güvenç, "Energetics and structures of small clusters: Pt_N , $N = 2 - 21$," *Surface Science*, vol. 525, no. 1-3, p. 66, 2003.
- [2] P. Rodriguez-Kessler and A. Rodriguez-Domnguez, "Size and structure effects of Pt_N ($N = 12 - 13$) clusters for the oxygen reduction reaction: First-principles calculations," *Journal of Chemical Physics*, vol. 143, no. 18, 2015.
- [3] Y. Chi, L. Zhao, X. Lu, C. An, W. Guo, and C.-M. L. Wu, "Effect of alloying on the stabilities and catalytic properties of Pt–Au bimetallic subnanoclusters: A theoretical investigation," *Journal of Nanoparticle Research*, vol. 18, p. 1, 2016.
- [4] P. Rodriguez-Kessler, A. Muñoz-Castro, P. Alonso-Dávila, F. Aguilera-Granja, and A. Rodriguez-Domnguez, "Structural, electronic and catalytic properties of bimetallic Pt_nAg_n ($n = 1 - 7$) clusters," *Journal of Alloys and Compounds*, vol. 845, p. 155 897, 2020.
- [5] P. Janthon *et al.*, "Bulk properties of transition metals: A challenge for the design of universal density functionals," *Journal of Chemical Theory and Computation*, vol. 10, no. 9, p. 3832, 2014.
- [6] S. Krüger, S. Vent, and N. Rösch, "Size dependence of bond length and binding energy in palladium and gold clusters," *Berichte der Bunsengesellschaft für Physikalische Chemie*, vol. 101, no. 11, p. 1640, 1997.
- [7] O. D. Häberlen, S.-C. Chung, M. Stener, and N. Rösch, "From clusters to bulk: A relativistic density functional investigation on a series of gold clusters Au_n , $n = 6, \dots, 147$," *Journal of Chemical Physics*, vol. 106, no. 12, p. 5189, 1997.
- [8] I. V. Yudanov, A. Genest, and N. Rösch, "DFT studies of palladium model catalysts: Structure and size effects," *Journal of Cluster Science*, vol. 22, p. 433, 2011.
- [9] R. Koitz, T. M. Soini, A. Genest, S. Trickey, and N. Rösch, "Scalable properties of metal clusters: A comparative study of modern exchange–correlation functionals," *Journal of Chemical Physics*, vol. 137, no. 3, 2012.
- [10] D. S. Rivera Rocabado, T. Ishimoto, and M. Koyama, "The effect of SnO_2 (110) supports on the geometrical and electronic properties of platinum nanoparticles," *SN Applied Sciences*, vol. 1, p. 1, 2019.
- [11] I. I. Aysan, T. Gorkan, I. Ozdemir, Y. Kadioglu, G. Gökolü, and E. Aktürk, "Electronic structure, cohesive and magnetic properties of iridium oxide clusters adsorbed on graphene," *Journal of Molecular Graphics and Modelling*, vol. 101, p. 107 726, 2020.

- [12] X. Zhou, J. Yang, and C. Li, "Theoretical study of structure, stability, and the hydrolysis reactions of small iridium oxide nanoclusters," *Journal of Physical Chemistry A*, vol. 116, no. 40, p. 9985, 2012.
- [13] A. Halder *et al.*, "Water oxidation catalysis via size-selected iridium clusters," *Journal of Physical Chemistry C*, vol. 122, no. 18, p. 9965, 2018.
- [14] I. Bandyopadhyay and C. M. Aikens, "Structure and stability of $(\text{TiO}_2)_n$, $(\text{SiO}_2)_n$, and mixed $\text{Ti}_m\text{Si}_{n-m}\text{O}_{2n}$ [$n = 2-5$, $m = 1$ to $(n-1)$] clusters," *Journal of Physical Chemistry A*, vol. 115, no. 5, p. 868, 2011.
- [15] S. Hamad, C. Catlow, S. Woodley, S. Lago, and J. Mejias, "Structure and stability of small TiO_2 nanoparticles," *Journal of Physical Chemistry B*, vol. 109, no. 33, p. 15 741, 2005.
- [16] S. Shevlin and S. Woodley, "Electronic and optical properties of doped and undoped $(\text{TiO}_2)_n$ nanoparticles," *Journal of Physical Chemistry C*, vol. 114, no. 41, p. 17 333, 2010.
- [17] E. Berardo *et al.*, "Describing excited state relaxation and localization in TiO_2 nanoparticles using TD-DFT," *Journal of Chemical Theory and Computation*, vol. 10, no. 12, p. 5538, 2014.
- [18] E. Berardo *et al.*, "Benchmarking the fundamental electronic properties of small TiO_2 nanoclusters by GW and coupled cluster theory calculations," *Journal of Chemical Theory and Computation*, vol. 13, no. 8, p. 3814, 2017.
- [19] B. Cordero *et al.*, "Covalent radii revisited," *Dalton Transactions*, no. 21, p. 2832, 2008.
- [20] R. W. G. Wyckoff and R. W. Wyckoff, *Crystal structures*. Interscience publishers New York, 1963, vol. 1.
- [21] Z.-w. Qu and G.-J. Kroes, "Theoretical study of the electronic structure and stability of titanium dioxide clusters $(\text{TiO}_2)_n$ with $n = 1-9$," *Journal of Physical Chemistry B*, vol. 110, no. 18, p. 8998, 2006.
- [22] R. Tomihara *et al.*, "Structural evolution of iridium oxide cluster anions Ir_nO_m^- ($n = 5-8$) with sequential oxidation: Binding mode of O atoms and Ir framework," *Journal of Physical Chemistry C*, vol. 123, no. 24, p. 15 301, 2019.
- [23] P. Lettenmeier *et al.*, "Nanosized IrOx-Ir catalyst with relevant activity for anodes of proton exchange membrane electrolysis produced by a cost-effective procedure," *Angewandte Chemie International Edition*, vol. 55, no. 2, p. 742, 2016.
- [24] P. Lettenmeier *et al.*, "Highly active nano-sized iridium catalysts: Synthesis and operando spectroscopy in a proton exchange membrane electrolyzer," *Chemical Science*, vol. 9, no. 14, p. 3570, 2018.

Carbon nanotube surface modified with platinum

6.1 Introduction

It is well established that platinum is an effective catalyst for a range of reactions, including the hydrogen electrode reaction (HER), oxygen electrode reaction (OER), water–gas shift (WGS), and others [1–7]. However, given the expense and limited availability of Pt–based materials, there is a significant demand for the design of new Pt nanostructures. These involve much less of this metal than bulk materials, allowing for a reduction in cost while maintaining the desired catalytic properties. Consequently, this type of system has been the subject of several studies, both experimental and theoretical, with the aim of exploring their physical and chemical properties and potential applications in fuel cells. In terms of experimental results, low loads of Pt on CNT surfaces have demonstrated remarkable electrocatalytic properties for HER and HOR reactions, in terms of durability, effective electrochemical active area, and current density, in comparison with conventional Pt/C electrodes. [8, 9]. The adsorption of platinum nanoclusters containing 1 – 7, 9, and 13 atoms on CNTs of different chiralities was investigated by DFT, which revealed energetically favorable configurations [9–15]. The metal–carbon surface exhibits a substantial charge delocalization and a change in the metal *d*–band profile, which affect the electrocatalytic activity of this hybrid material [12]. Furthermore, the use of this metal can be reduced by utilizing Pt nanostructures, which have a larger number of low–coordinated sites. These sites are of great importance for catalytic phenomena due to the stabilization of reaction intermediates [16].

Therefore, there is a good reason to study platinum nanoparticles. In this sense, the present thesis intends to contribute to this matter from a theoretical point of view, studying small clusters dispersed on a (5,5)–CNT surface in order to analyze the particle–surface interaction. Thus, this chapter introduces the results and further discussion of the deposition of platinum nanoparticles, as presented in chapter 6, on the external surface of the carbon nanotube model.

System	Site (Name)	E_{int}/eV	$d_{\text{NP-CNT}}/\text{\AA}$
Pt ₁ /CNT	Pt/ <i>br</i>	−2.41	2.07
	Pt/ <i>stp</i>	−2.20	2.01
	Pt/ <i>tp</i>	−1.93	2.01
	Pt/ <i>hw</i>	−1.15	2.34

Table 6.1: Interaction sites, energies (E_{int}) and minimum particle–surface distances ($d_{\text{NP-CNT}}$) of the optimized Pt₁/CNT configurations.

6.2 Results and discussion

In order to analyze the stability of these hybrid systems, the particle–surface interaction energy was defined as of eq. 6.1

$$E_{\text{int}} = [E_{\text{Pt}_n/\text{CNT}} - E_{\text{Pt}_n} - E_{\text{CNT}}] / n \quad (6.1)$$

where $E_{\text{Pt}_n/\text{CNT}}$, E_{Pt_n} and E_{CNT} are the total electronic energies of the total system, the nanoparticle in gas-phase and the pristine carbon surface, respectively, and n is the number of platinum atoms in the particle. All particles introduced in section 5.1 were considered for their deposition.

For the smaller Pt_{*n*} systems ($n = 1 - 4$), a carefully analysis regarding particle orientation and surface interacting sites was carried out. In this context, a single platinum atom (Pt₁) deposition on (5, 5)–CNT was systematically investigated first, considering high-symmetry sites of the carbon nanotube: "hollow" (*hw*), "top" (*tp*) and "bridges" (*br*) (see Fig. 4.3a). The results in Table 6.1 indicate that the deposition on the carbon surface is highly favorable and the energetic of the platinum–surface interaction is given with the following order of stability: $br < tp < hw$. In addition, some of the platinum atoms at *hw* sites suffered a position shift toward the *tp* site during optimization, resulting in a new adsorption site labeled as "shifted-top" (*stp*). According to the results in Table 6.1, the stability of the deposition of Pt on the *stp* site can be situated between that of the corresponding *br* and *tp* sites. The geometric configuration of the most stable Pt₁/CNT system, i.e. the *br* site, is shown in Fig. 6.4. These results are in agreement with values reported elsewhere [10, 17, 18].

The results obtained for the Pt₁/CNT configurations were taken into account in the study of the deposition of larger nanoparticles. To continue with, the Pt₂ dimer was deposited with each platinum atom tentatively located in one of the previously considered sites. Interaction energy results are presented in Table 6.2. A preference for *br* sites is also observed for the most stable case, closely followed by the corresponding deposition on *tp* sites. The other configurations, although seemingly convenient for individual atoms, are being limited by the Pt–Pt bond length.

Following with this approach, the analysis of Pt₃ deposition has been done with both lineal and triangular particle configurations. According to the energetic results in Table 6.3, the clustered structures are preferred. Among them, those were only two platinum atoms interact directly with the CNT (vertical deposition, the most stable case named as **3b**, see Fig. 6.1) present enhanced stability than that of those in which the carbon–surface interface involves three platinum atoms (horizontal deposition, the most stable case named as **3a**, see Fig. 6.1). The observed behavior can be attributed to a structural incompatibility between the support and the nanoparticle. These results are in good

System	Site (Name)	E_{int}/eV	$d_{\text{NP-CNT}}/\text{\AA}$	$d_{\text{Pt-Pt}}/\text{\AA}$
Pt ₂ /CNT	Pt/ <i>br,br</i>	−2.64	2.02	2.64
	Pt/ <i>tp,tp</i>	−2.61	2.07	2.49
	Pt/ <i>br,br</i>	−2.53	2.09	2.49
	Pt/ <i>stp,stp</i>	−2.45	2.13	2.65

Table 6.2: Interaction sites, energies (E_{int}), minimum particle–surface distances ($d_{\text{NP-CNT}}$), and Pt–Pt distances ($d_{\text{Pt-Pt}}$) of the optimized Pt₂/CNT configurations.

System	Site (Name)	E_{int}/eV	$d_{\text{NP-CNT}}/\text{\AA}$	$d_{\text{Pt-Pt}}/\text{\AA}$
Pt ₃ /CNT (triangular)	Pt/ <i>br,br</i> (3b)	−3.30	2.11	2.53
	Pt/ <i>stp,stp</i>	−3.27	2.08	2.55
	Pt/ <i>br,br</i>	−3.20	2.13	2.52
	Pt/ <i>tp,tp,br</i> (3a)	−2.85	2.13	2.59
	Pt/ <i>stp,tp,tp</i>	−2.79	2.23	2.59
Pt ₃ /CNT (lineal)	Pt/ <i>br,br,br</i>	−2.98	2.06	2.57
	Pt/ <i>br,br,tp</i>	−2.86	2.03	2.55
	Pt/ <i>br,br,tp</i>	−2.59	2.05	2.59

Table 6.3: Interaction sites, energies (E_{int}), minimum particle–surface distances ($d_{\text{NP-CNT}}$), and average Pt–Pt distances ($d_{\text{Pt-Pt}}$) of the optimized Pt₃/CNT configurations. Labels of systems of interest are also shown.

agreement with rather similar systems reported by others [11]. In the case of Pt_{3b}, modifications on the deposition region of the CNT due to the presence of the particle are subtler and the carbon material seems to remain geometrically comparable to the pristine nanotube (C–C expansion of 1.4 %). The horizontal adsorption (Pt_{3a}), in turn, introduces a stronger perturbation, leading to a higher expansion of the neighboring carbon network (3.3 %). A similar trend is found when the Pt–Pt distances on the particles are compared with the corresponding ones in gas phase (4.4 % for Pt_{3a} and 2.4 % for Pt_{3b}). The above findings indicate that the less favorable energy associated with the horizontal adsorption of Pt₃ is related to a larger geometrical stress on both the particle and the nanotube.

The results introduced up to this point indicate enhanced stability of the Pt₁, Pt₂ and Pt₃ particles when deposited on *br*, *stp* and *tp* sites. This can be attributed to the formation of strong Pt–C

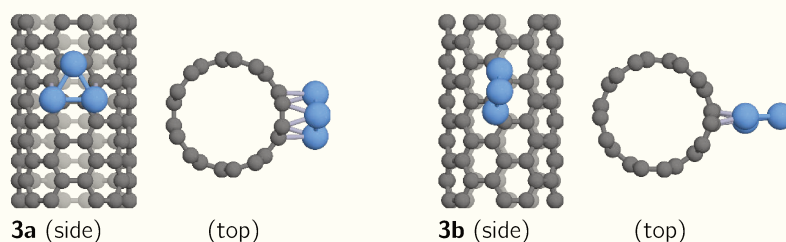


Figure 6.1: Side and top views of selected Pt₃/CNT adsorbed configurations.

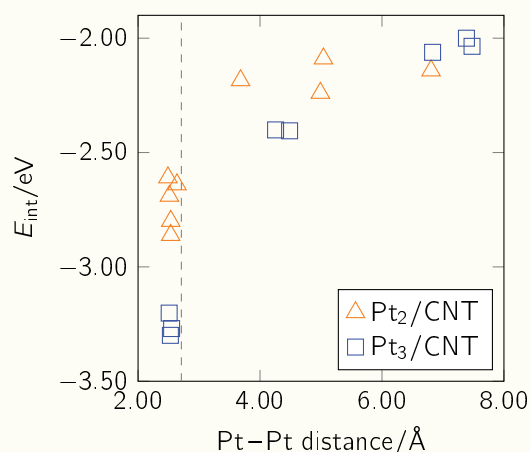


Figure 6.2: Interaction energies as a function of the average Pt–Pt distances of several Pt₂/CNT and Pt₃/CNT systems containing dispersed and agglomerated platinum atoms. Pt–Pt distance in crystal bulk (2.71 Å) is shown in dashed line as a reference.

covalent bonds, which is a reasonable assumption given the considerable magnitude of the interaction energies involved, and the information provided by the Fermi softness plot of the CNT (see Table 4.2). This plot indicates that the aforementioned regions of the nanotube are more likely to form covalent bonds, as they localize high FS values. Accordingly, the deposition of platinum nanoparticles can be categorically defined as a chemisorption process.

Other interesting aspect to consider is the dispersion vs. agglomeration of Pt atoms on the nanotube surface. This effect was analyzed by considering several systems containing two and three metallic atoms deposited on favorable (*br* and/or *stp*) sites of the CNT at different relative distances. Fig. 6.2 presents the results of this analysis, where it is possible to observe that, for both Pt₂/CNT and Pt₃/CNT systems, the most stable cases are given for those configurations where the platinum atoms are located at relative distances which can be considered within the chemical bond length range. Thus, the deposition of Pt_{*n*} on CNT is expected to follow a clustered form, as the Pt–Pt interaction is clearly stronger than the corresponding Pt–C one.

The study of the deposition of larger Pt_{*n*} particles ($n \geq 4$) was carried out in a similar way as that used for the Pt₂ and Pt₃ structures, i.e. tentatively placing the platinum atoms of the particles on the energetically favored *br*, *stp* and *tp* sites of the CNT. In addition, special attention has been paid to those configurations which followed a bottom-up construction.¹ However, as the particles grew in size, their deposition on the CNT resulted in a similar number of Pt atoms interacting directly with the carbon surface, the most stable systems of each size involving particle–CNT interfaces with only 2, 3 or 4 platinum atoms. This observation, which is somehow expected considering the small diameter and consequently large curvature of the CNT, can be asserted from Fig. 6.3a which shows an asymptotic behavior of the interaction energy results for such systems, with a small variation of the values for $n > 7$. This would indicate a limit on the effective interaction area of the (5, 5)–CNT with respect to the Pt_{*n*} particles. Nonetheless, it is also worth noting from Fig. 6.3a the existence of an stabilization effect of the nanoparticles at the CNT surface, as the interaction energies are more favorable than

¹i.e. those Pt_{*n*}/CNT systems whose structures do not differ notably from that of some stable Pt_{*n-1*}/CNT configuration, but for the presence of an additional single Pt atom.

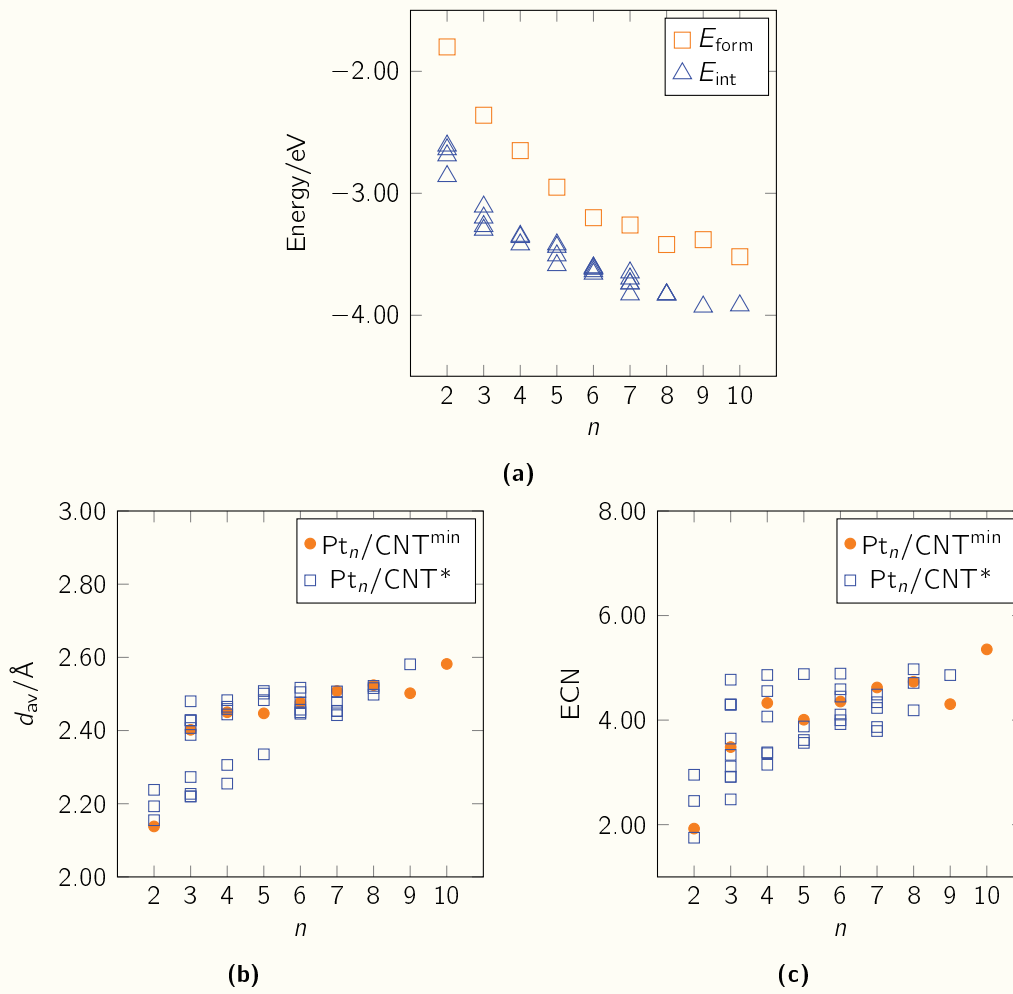
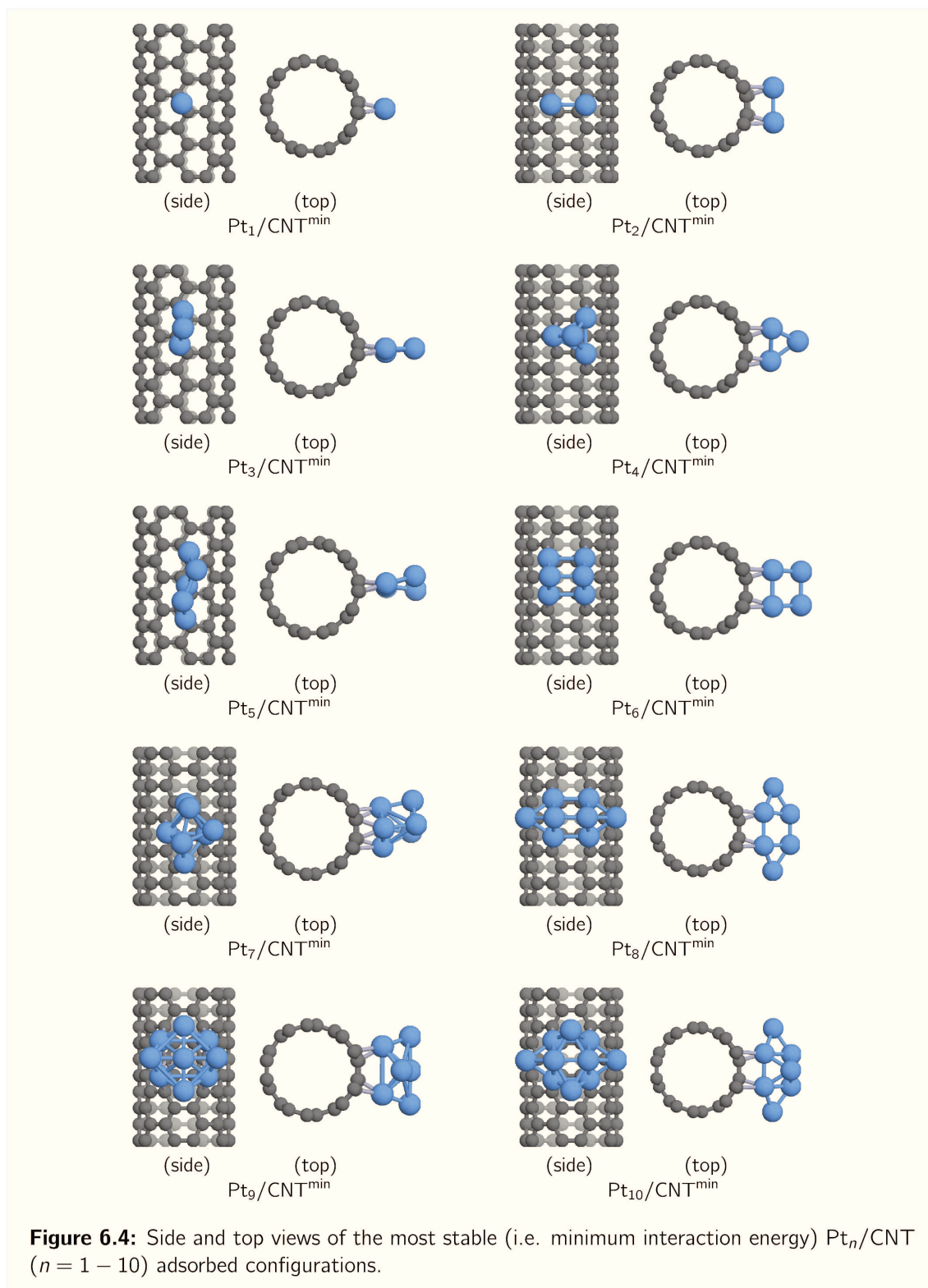


Figure 6.3: Pt_n formation and Pt_n/CNT interaction energies (E_{form} and E_{int} , respectively) (a), average bond lengths (d_{av}) (b), and average effective coordination numbers (ECN) of Pt atoms (c) as a function of the particle size n . In (b) and (c) plots, orange dots ($\text{Pt}_n/\text{CNT}^{\text{min}}$) represent the systems with the lower interaction energies, whilst the rest of the structures is shown as blue squares (Pt_n/CNT^*).

the respective particle formation energies (eq. 5.1) in all cases. The stability of Pt_n/CNT systems, however, does not seem to be well related to the average bond lengths nor the coordination number of the deposited platinum atoms, as noted from Figs. 6.3b and 6.3c, respectively, as the most stable cases for each n (orange dots) do not necessarily match an d_{av} or ECN extrema. Nevertheless, an increasing trend of both quantities is observed with the increasing particle size for all considered systems. Finally, Fig. 6.4 presents information of the most stable Pt_n/CNT systems.

6.3 Summary

In the present chapter, the adsorption of small Pt_n ($n = 1 - 10$) particles on a (5, 5) carbon nanotube (CNT) has been investigated. This included the optimization of the platinum nanostructures and adsorption sites on the carbon surface and the identification of the most stable configurations.



In addition, different factors that govern the thermodynamic of the particle adsorption have been analyzed in detail.

The analysis of the interaction energies revealed the most stable sites for Pt–CNT interaction. Moreover, for Pt₃/CNT systems, the number of platinum atoms directly interacting with the carbon nanotube was limited due to structural incompatibility between the nanoparticle and the support, which induced a larger geometrical stress and thus poorer interaction energies for the system with larger quantity of Pt–C bonds. This limitation was also observed with bigger particles ($n \geq 4$), which is in agreement with the small diameter of the CNT. Furthermore, a stabilization effect of the nanoparticles at the carbon surface is observed. This encourages the study of systems with small platinum particles, considering that low coordinated sites might play an important role in their catalytic properties.

References for Chapter 6

- [1] J. K. Norskov and C. H. Christensen, "Toward efficient hydrogen production at surfaces," *Science*, vol. 312, no. 5778, p. 1322, 2006.
- [2] J. Wang *et al.*, "Anchoring ultrafine Pt electrocatalysts on $\text{TiO}_2\text{-C}$ via photochemical strategy to enhance the stability and efficiency for oxygen reduction reaction," *Applied Catalysis B: Environmental*, vol. 237, p. 228, 2018.
- [3] Q. Fu, H. Saltsburg, and M. Flytzani-Stephanopoulos, "Active nonmetallic Au and Pt species on ceria-based water-gas shift catalysts," *Science*, vol. 301, no. 5635, p. 935, 2003.
- [4] S. C. Ammal and A. Heyden, "Water-gas shift activity of atomically dispersed cationic platinum versus metallic platinum clusters on titania supports," *ACS Catalysis*, vol. 7, no. 1, p. 301, 2017.
- [5] A. Bruix *et al.*, "A new type of strong metal-support interaction and the production of N_2 through the transformation of water on Pt/CeO_2 (111) and $\text{Pt/CeO}_x/\text{TiO}_2$ (110) catalysts," *Journal of the American Chemical Society*, vol. 134, no. 21, p. 8968, 2012.
- [6] S. Aranifard, S. C. Ammal, and A. Heyden, "On the importance of metal-oxide interface sites for the water-gas shift reaction over Pt/CeO_2 catalysts," *Journal of Catalysis*, vol. 309, p. 314, 2014.
- [7] C. Ratnasamy and J. P. Wagner, "Water gas shift catalysis," *Catalysis Reviews*, vol. 51, no. 3, p. 325, 2009.
- [8] M. Tavakkoli *et al.*, "Electrochemical activation of single-walled carbon nanotubes with pseudo-atomic-scale platinum for the hydrogen evolution reaction," *ACS Catalysis*, vol. 7, no. 5, p. 3121, 2017.
- [9] T. Kim, Y. Kwon, S. Kwon, and J. G. Seo, "Substrate effect of platinum-decorated carbon on enhanced hydrogen oxidation in PEMFC," *ACS Omega*, vol. 5, no. 41, p. 26902, 2020.
- [10] P. Pannopard, P. Khongpracha, M. Probst, and J. Limtrakul, "Gas sensing properties of platinum derivatives of single-walled carbon nanotubes: A DFT analysis," *Journal of Molecular Graphics and Modelling*, vol. 28, no. 1, p. 62, 2009.
- [11] D. H. Chi *et al.*, "Electronic structures of Pt clusters adsorbed on (5,5) single wall carbon nanotube," *Chemical Physics Letters*, vol. 432, no. 1-3, p. 213, 2006.
- [12] N. T. Cuong, A. Fujiwara, T. Mitani, and D. H. Chi, "Effects of carbon supports on Pt nano-cluster catalyst," *Computational Materials Science*, vol. 44, no. 1, p. 163, 2008.

- [13] N. T. Cuong, A. Sugiyama, A. Fujiwara, T. Mitani, and D. H. Chi, "Density functional study of Pt₄ clusters adsorbed on a carbon nanotube support," *Physical Review B*, vol. 79, no. 23, p. 235 417, 2009.
- [14] X. Zhang, H. Cui, D. Chen, X. Dong, and J. Tang, "Electronic structure and H₂S adsorption property of Pt₃ cluster decorated (8,0) SWCNT," *Applied Surface Science*, vol. 428, p. 82, 2018.
- [15] J.-g. Wang, Y.-a. Lv, X.-n. Li, and M. Dong, "Point-defect mediated bonding of Pt clusters on (5,5) carbon nanotubes," *Journal of Physical Chemistry C*, vol. 113, no. 3, p. 890, 2009.
- [16] M. J. Kolb, F. Calle-Vallejo, L. B. Juurlink, and M. Koper, "Density functional theory study of adsorption of H₂O, H, O, and OH on stepped platinum surfaces," *Journal of Chemical Physics*, vol. 140, no. 13, 2014.
- [17] E. Durgun, S. Dag, V. M. K. Bagci, O. Gülseren, T. Yildirim, and S. Ciraci, "Systematic study of adsorption of single atoms on a carbon nanotube," *Physical Review B*, vol. 67, p. 201 401, 20 2003.
- [18] G. Chen and Y. Kawazoe, "Interaction between a single Pt atom and a carbon nanotube studied by density functional theory," *Physical Review B*, vol. 73, no. 12, p. 125 410, 2006.

Carbon nanotube surface modified with iridium oxide

7.1 Introduction

The following is a brief description of some important experimental and theoretical contributions to the study of carbon surfaces, especially nanotubes, modified with iridium oxide-related compounds. Special attention was paid to those in which important reactions (as OER, HER and WO –see below) are investigated considering these materials as potential catalysts. The nature and dimensions of such systems recall the ones to be described in this chapter.

Wen et al. [1] have studied oxygen evolution reaction (OER) on ultrafine iridium oxide particles ($1.0 - 1.3 \text{ \AA}$) on multi-walled CNT (MWCNT) with an inner size of $5 - 10 \text{ nm}$. According to their work, iridium is present as Ir^{+4} , and the hybrid material showed "efficient and robust water oxidation performance": $\text{TOF} = 3.48 \text{ s}^{-1}$, $\eta = 217 - 272 \text{ mV}$, and good stability.

Guan et al. [2] have studied sub-nanometric iridium dioxide clusters supported on MWCNT by chemical vapor deposition (CVD) method. This resulted in a narrow distribution of cluster sizes, "from several atoms to 2 nm , having an average size of ca. 1.1 nm ". Moreover, the authors suggest that the synthesized material "demonstrated to be highly efficient and robust for water oxidation" (WO) reaction: $\text{TOF} = 11.2 \text{ s}^{-1}$, $\eta = 249/293 \text{ mV}$ in basic/acidic media, respectively. The high efficiency in WO reaction is attributed to the sub-nanometric size of the iridium oxide particles, and the unsaturated Ir atoms, compared to commercial (rutile) IrO_2 .

Badam et al. [3] synthesized and characterized IrO_2 catalysts supported on MWCNT ($10 - 20 \text{ nm}$ diameter) substrate. Iridium oxide particle sizes were in the order of the 1.7 nm , with a structure resembling that of the IrO_2 rutile. A "strong metal-substrate interaction" was determined by X-ray photoelectron spectroscopy (XPS). OER overpotential at 10 mA/cm^2 for this material was found to be 270 mV in acidic conditions, which was "around 12 mV and 50 mV lesser than on nanoporous IrO_2 [4] and IrO_2/Pt [5], respectively". For this reaction, the high activity and durability were ascribed

to the conducting nature of the substrate, and to the strong metal–substrate anchoring.

On the other hand, Aysan et al. [6] analyzed the interaction of $(\text{IrO})_n$ and $(\text{IrO}_2)_n$ ($n = 1 - 5$) clusters with a pristine graphene surface, following a similar computational methodology as the one taken in this Thesis. A weak particle–surface interaction can be induced from their results regarding $(\text{IrO}_2)_n$ systems, based both in their large Ir–C distances and in the absence of clear bonds between these clusters and the graphene surface. As it will be described in this chapter, the results presented here for the CNT surface are in partially agreement with Ayzan's conclusions for graphene, although more promising outcomes are hereby reported.

Motivated by these good theoretical and experimental results, an in–depth study about the deposition of iridium oxide nanoparticles in a carbon nanotube surface was carried out, in order to be able to describe the particle–surface interactions and characterize the strength of such interaction. These results were considered as a starting point for the study of water dissociation reaction on iridium oxide–modified CNTs in chapter 10.

7.2 Results and discussion

Following a similar approach to that used with platinum nanoparticles, the high symmetry sites of the carbon surface were considered as points of interaction between the $(\text{IrO}_2)_n$ particles and the CNT: "hollow" (*hw*), "top" (*tp*) and "bridges" (further subdivided in "horizontal"—*brH*—and "oblique"—*brD*—to the CNT axis). Only small $(\text{IrO}_2)_n$ particles were used in this study ($n = 1, 2, 3$), in order to maintain a proportional size with the CNT diameter. Different configurations were initially proposed to study the interaction between the $(\text{IrO}_2)_n$ and the CNT, exploring not only the mentioned carbon surface sites but the relative particle orientation as well, considering that both O and Ir could, in principle, have chemically interacted with the carbon surface. The proposed structures were subjected to geometry optimization, and the interaction energy between the particle and the surface of the most stable configurations, computed according to eq. 7.1, was then obtained.

$$E_{\text{int}} = [E_{(\text{IrO}_2)_n/\text{CNT}} - E_{(\text{IrO}_2)_n} - E_{\text{CNT}}] / n \quad (7.1)$$

In this equation, $E_{(\text{IrO}_2)_n/\text{CNT}}$, $E_{(\text{IrO}_2)_n}$ and E_{CNT} represent the electronic energies of the total system, the nanoparticle in gas–phase and the pristine carbon surface, respectively, and n is the amount of IrO_2 units in the oxide.

The deposition of a single oxide unit $(\text{IrO}_2)_1$ on CNT was first studied. As stated above, several configurations involving different surface sites and particle orientations were tentatively explored. In particular, eight initial models were proposed. In half of the models, the Ir atom of the oxide was placed in one of the carbon surface sites (*hw*, *tp*, *brH* and *brD*) with the oxygen atoms pointing outward from the CNT (see example in Fig. 7.1a). In the other half, oxygen atoms were pointed toward from the surface (see example in Fig. 7.1b), and the particle was placed such that each of the O atoms were located in sites that best matched the carbon surface sites. As a consequence of the CNT pattern, it was possible to place the oxygen atoms in pairs of equivalent sites.

Table 7.1 lists the resulting interaction energies and particle–surface distances for the optimized $(\text{IrO}_2)_1/\text{CNT}$ models. It is possible to observe that only two of the systems form stable adsorptions

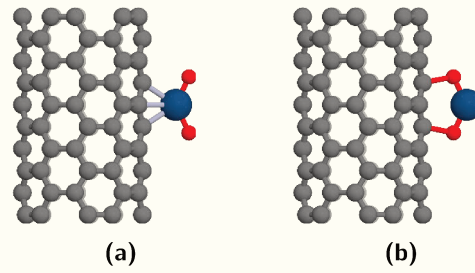


Figure 7.1: Different relative orientations considered for the $(\text{IrO}_2)_1$ nanoparticle: oxygen atoms pointing outward (a) and toward (b) from the CNT surface.

System	Site (Name)	E_{int}/eV	$d_{\text{NP-CNT}}/\text{\AA}$
$(\text{IrO}_2)_1/\text{CNT}$	Ir/ <i>tp</i> (1a)	-0.40	2.40
	Ir/ <i>brD</i> (1b)	-0.23	2.21
	O/ <i>brH</i>	+2.3	1.57
	{phys}	-0.37	3.08
	{phys}	-0.41	3.02
	{phys}	-0.31	2.97
	{phys}	-0.40	2.98
	{phys} (1c)	-0.36	2.95

Table 7.1: Interaction sites, energies (E_{int}) and minimum particle–surface distances ($d_{\text{NP-CNT}}$) of the optimized $(\text{IrO}_2)_1/\text{CNT}$ configurations. Denominations of systems of interest are also shown. Physisorbed configurations are indicated as "{phys}".

(named **1a** and **1b**), which are characterized by means of the formation of one (**1a**) or two (**1b**) Ir–C bonds, while no oxygen atom seems to participate in the particle–surface bonding (see Fig. 7.4 below). The interaction energies and particle–surface distance results obtained from the rest of the physisorbed systems are grouped at $E_{\text{int}} \approx -0.5$ eV and $d_{\text{NP-CNT}} \approx 3.1$ Å, respectively (see Fig. 7.3 below). Noteworthy, the physisorbed states are equivalently or even more energetically stable than the adsorbed systems. The substantial physisorption energies observed for $(\text{IrO}_2)_1/\text{CNT}$ were not found in systems involving the deposition of larger nanoparticles.

The type of interaction (adsorption or physisorption) between the iridium oxide and the surface was determined by means of both geometric and electronic considerations. For the geometric aspect, the reported atomic covalent radius [7] were used to compute $r_{\text{C-O}}^{\text{max}}$ and $r_{\text{C-Ir}}^{\text{max}}$ according to eq. 7.2.

$$r_{\text{C-O}}^{\text{max}} = (r_{\text{C}}^{\text{cov}} + r_{\text{O}}^{\text{cov}}) \cdot 133\% = 1.85 \text{ \AA} \quad (7.2a)$$

$$r_{\text{C-Ir}}^{\text{max}} = (r_{\text{C}}^{\text{cov}} + r_{\text{Ir}}^{\text{cov}}) \cdot 133\% = 2.85 \text{ \AA} \quad (7.2b)$$

which helped establishing a soft limit of covalent bonds in the studied systems. Considering that all stable particle–surface covalent interactions are given between Ir and C atoms, the $r_{\text{C-Ir}}^{\text{max}}$ value is used in Fig. 7.3 (see below) to draw a line between adsorbed and physisorbed states.

With respect to the electronic effects, atomic orbitals overlapping values were obtained by means of DDEC6 analysis. Table 7.2 presents the sum of Ir–C overlaps for systems corresponding to

System name	Site	Ir–C ovlp./ e
1a	Ir/ <i>tp</i>	0.55
1b	Ir/ <i>bgD</i>	1.01
1c	{phys}	0.25

Table 7.2: Atomic Ir–C overlap values for selected $(\text{IrO}_2)_1/\text{CNT}$ systems obtained by means of DDEC6 analysis.

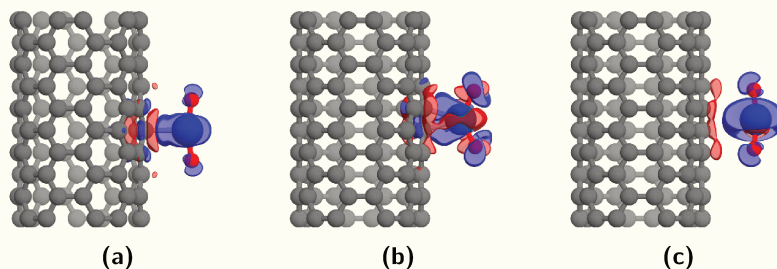


Figure 7.2: Charge density difference plots of **1a** (a), **1b** (b) and **1c** (c) systems. Blue and red colors indicate regions with charge accumulation and depletion, respectively. Isovalue: $0.001 |e|/\text{\AA}^3$.

both adsorbed (**1a** and **1b**) and physisorbed (here represented by the system with the smaller particle–surface distance, and denominated as **1c**) states. The physisorbed system **1c** shows the least, although non–zero, overlapping value, meaning that there is a weak interaction between the Ir and the surface. Adsorbed systems **1a** and **1b**, on the other hand, present larger overlapping values, whose proportion is in line with the amount of Ir–C bonds in *tp* and *bgD* sites adsorptions as described above.

Furthermore, to analyze the effect of the electronic redistribution due to particle–surface interaction, charge density differences were computed as of eq. 7.3,

$$\Delta\rho(\mathbf{r}) = \rho_{(\text{IrO}_2)_n/\text{CNT}}(\mathbf{r}) - \rho_{\text{CNT}}(\mathbf{r}) - \rho_{(\text{IrO}_2)_n}(\mathbf{r}) \quad (7.3)$$

where $\rho_{(\text{IrO}_2)_n/\text{CNT}}$, ρ_{CNT} and $\rho_{(\text{IrO}_2)_n}$ are the electronic charge densities corresponding to the total system, the CNT surface and the iridium oxide particle in gas phase, respectively. The last two systems were frozen at their final equilibrium configuration upon adsorption. The results are shown in Fig. 7.2, on which the charge accumulation on the Ir–C bond region clearly reaffirms the existence of covalent bonds in the adsorbed systems **1a** and **1b** (Figs. 7.2a and 7.2b, respectively). Conversely, in physisorbed states (Fig. 7.2c) although no covalent bondings are observed, there is indeed a charge relocation of the carbon surface π electrons –close to the zone of interaction– to the iridium oxide particle. This charge polarization, together with the low Ir–C overlapping value, provides an evidence of the non–bonding nature of the physisorption interaction, which is in line the interaction energy values of these systems.

To continue with, the deposition of both rutile and GA–derived $(\text{IrO}_2)_2$ particles was analyzed following a similar approach to that used for the single IrO_2 unit described above. Both Ir and O atoms from

System name	Site	Ir–C ovlp./ e
3a	Ir/ <i>bgD</i>	1.02
3b	Ir/ <i>bgD</i>	1.03
3c	Ir/ <i>tp</i>	0.77

Table 7.3: Atomic Ir–C overlap values for (chemically) adsorbed (IrO₂)₃/CNT systems obtained by means of DDEC6 analysis.

the nanoparticles were tentatively used as possible binding points with the different sites of the carbon surface, summing up eleven and four initial models for rutile and GA-derived particles, respectively. No chemically adsorbed (IrO₂)₂/CNT systems were found in this study. In turn, all proposed models adopted different physisorbed states during geometry optimization. As seen in Table 7.4, the relaxed systems presented low interaction energies (approximately -0.15 eV and -0.05 eV for rutile and GA-derived models, respectively) and large particle–surface distances (between 2.8 Å and 4.0 Å for all (IrO₂)₂ particles). The interaction energies, however, suggested that the physisorption of rutile-derived particles is slightly more favored than in the case of the GA-derived models.

Lastly, the deposition of (IrO₂)₃ nanoparticles was investigated. Considering the results obtained for the previous systems, only initial configurations involving Ir–C interactions were proposed under the same tentative approach. The interaction energies and particle–surface distances of the optimized (IrO₂)₃/CNT systems are listed in Table 7.4. In addition, the geometric configurations of selected systems are presented in Fig. 7.4. Compared with the (IrO₂)₂ cases, the deposition analysis of (IrO₂)₃ particles yielded some promising outcomes for rutile-derived models, showing stable adsorptions on *brD* and *tp* sites, which are given by means of the formation of approximately two and one Ir–C bonds for the formers (namely **3a** and **3c**) and the latter (**1c**), respectively. Table 7.3 list the Ir–C overlap values for these configurations, which closely resemble the ones found for the **1a** and **1b** systems. This information, together with the interaction energies, does not suggest a noteworthy improvement on the stability of the larger (IrO₂)₃ particles on the carbon surface. On the other hand, GA-derived (IrO₂)₃ particle relaxations on the CNT surface sites did not resulted in chemically adsorbed states regardless of the proposed initial configuration.

Results from (IrO₂)_{*n*}/CNT ($n = 1, 2, 3$) models are summarized in Fig. 7.3, where it is possible to assert that physisorption states are predominant for this systems. Only few stable chemisorbed configurations were obtained, namely **1a**, **1b**, **3a**, **3b** and **3c**, with favorable interaction energies ranging from -0.2 eV to -0.5 eV.

To further analyze these findings, a qualitative description with electrostatic potentials (EP) and Fermi softness (FS) was made. From Table 4.2 it is possible to observe that the electrostatic potential on the carbon surface is very weak, about 10^3 times smaller than the one found in the iridium oxide nanoparticles (see Table 5.6). Such an homogeneous EP does not offer, in principle, an attractive interaction for the oxide nanoparticles which, in turn, present a substantial potential polarization. The local Fermi softness of CNT in Table 4.2, on the other hand, points to more reactive electronic states in regions near the *tp* and *bgD* sites. Thus, FS qualitative analysis confirms that the (IrO₂)_{*n*}-CNT binding in the adsorbed configurations has a covalent character, involving *p*–C and *d*–Ir electronic states close to Fermi energy. As the magnitude of the Fermi softness close to Ir atoms in the

Size	Rutile			GA		
	Site (Name)	E_{int}/eV	$d_{\text{NP-CNT}}/\text{\AA}$	Site (Name)	E_{int}/eV	$d_{\text{NP-CNT}}/\text{\AA}$
$n = 2$	{phys}	-0.17	2.90	{phys}	-0.02	3.23
	{phys}	-0.14	2.99	{phys}	-0.01	3.19
	{phys}	-0.15	3.09	{phys}	-0.02	3.17
	{phys}	-0.14	2.94	{phys}	-0.01	4.19
	{phys}	-0.15	2.86			
	{phys}	-0.17	3.03			
	{phys}	-0.17	2.99			
	{phys}	-0.16	3.06			
	{phys}	-0.17	3.16			
	{phys}	-0.18	2.96			
	{phys}	-0.14	3.00			
$n = 3$	lr/bg- (3a)	-0.43	2.15	{phys}	-0.04	3.26
	lr/bg-⊥ (3b)	-0.49	2.14	{phys}	-0.04	3.10
	lr/tp- (3c)	-0.39	2.21	{phys}	-0.04	3.63
				{phys}	-0.09	3.19
				{phys}	-0.10	3.19
				{phys}	-0.09	3.47
				{phys}	-0.06	3.17
				{phys}	-0.06	3.21
				{phys}	-0.06	3.51

Table 7.4: Interaction sites, energies (E_{int}) and minimum particle-surface distances ($d_{\text{NP-CNT}}$) of the optimized $(\text{IrO}_2)_n^{\text{rutile}}/\text{CNT}$ and $(\text{IrO}_2)_n^{\text{GA}}/\text{CNT}$ ($n = 2, 3$) configurations. Physisorbed configurations are indicated as "{phys}".

nanoparticles is more pronounced in the rutile-derived models (see Table 5.6), their greater stability on the carbon surface (specifically at the mentioned *tp* and *bgD* sites), with respect to GA-derived particles, is then justified. The lower reactivity of the latter towards a covalent surface like that of CNT is not unexpected, considering the "core-shell" structure of the GA-derived iridium oxide nanoparticles, with "oxo"-type oxygen atoms at their surface withdrawing electronic charge from the iridium atoms. As seen in Table 5.7, there is a substantial difference of the Fermi softness of the electronic charge near the oxygen and iridium atoms, which implies that the mentioned charge withdrawal would be accompanied by a diminishing of the bond-forming capability of the Ir species, and therefore of the covalent interaction between the particles and the carbon surface.

7.3 Summary

Following the previous analysis of Pt_n/CNT systems, a study regarding the deposition of iridium oxide nanoparticles, $(\text{IrO}_2)_n$ ($n = 1, 2, 3$), on a (5, 5) carbon nanotube (CNT) surface has been made in this chapter. For this matter, structures derived from both rutile systems and Genetic Algorithm (GA) methods have been employed.

Contrary to what was found for Pt clusters in the previous chapter, the iridium oxide particles showed a weaker interaction with the pristine carbon surface. Moreover, the greater stability of the GA-derived clusters in the gas phase (as seen in chapter 5), in comparison to bulk-derived configurations, led to

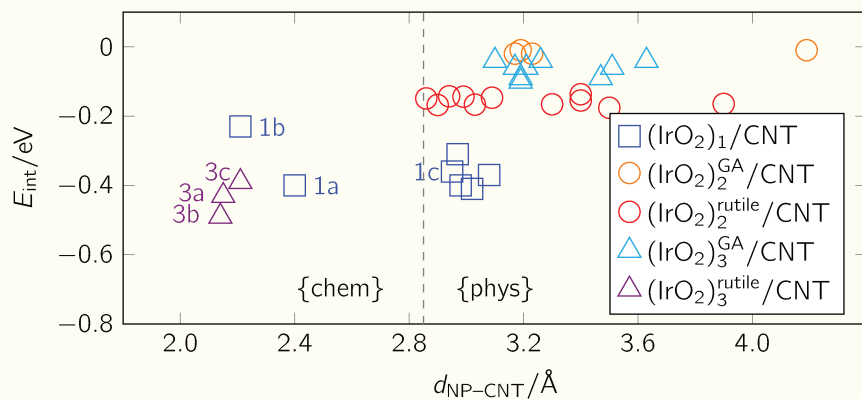


Figure 7.3: Interaction energies (E_{int}) plotted w.r.t. the minimum particle–surface distances ($d_{\text{NP-CNT}}$) of the optimized $(\text{IrO}_2)_n^{\text{rutile}}/\text{CNT}$ and $(\text{IrO}_2)_n^{\text{GA}}/\text{CNT}$ systems. The sum of Ir and C covalent radius reported in literature is also shown in dashed line as a reference, in order to distinguish between "chemisorbed" and "physisorbed" domains ($\{\text{chem}\}$ and $\{\text{phys}\}$, respectively).

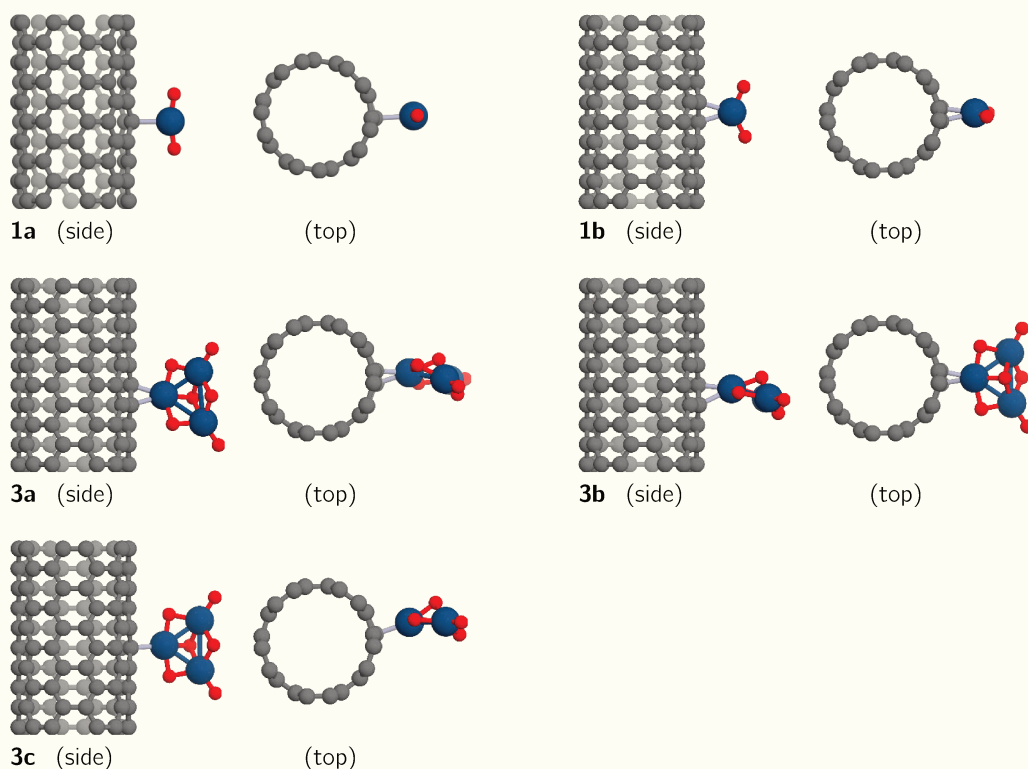


Figure 7.4: Side and top views of the (chemically) adsorbed $(\text{IrO}_2)_n/\text{CNT}$ configurations.

a negative impact on their interaction energies with the CNT. This resulted in a physisorbed state for all GA-derived particles. The stabilization of such physisorbed states can be attributed to a charge polarization induced by the particle–surface interaction. On the other hand, covalent Ir–C bonding resulted from the interaction of the IrO₂ monomer and the rutile-derived (IrO₂)₃ particle with the CNT. These findings correlate well with the regions of reactive electronic orbitals, as illustrated in the localized Fermi softness plots (see Fig. 4.2 and Table 5.7). In turn, the "core–shell–like" structure of the GA-derived iridium oxide nanoparticles, with larger charge transfer from the metal to the oxygen atoms, justifies the reduced reactivity of the Ir atoms toward covalent surfaces as that of the CNT. This again confirms Fermi softness as a useful tool for the prediction of such interactions. Lastly, it is worth noting that larger particles do not seem to improve their stability on the carbon nanotube surface. This can be considered of practical interest, considering that small-sized supporting materials such as the (5, 5)–CNTs could be carrying iridium oxide particles at the nanoscale, thus reducing the amount of precious catalyst used.

References for Chapter 7

- [1] X. Wen, L. Bai, M. Li, and J. Guan, "Ultrafine iridium oxide supported on carbon nanotubes for efficient catalysis of oxygen evolution and oxygen reduction reactions," *Materials Today Energy*, vol. 10, p. 153, 2018.
- [2] J. Guan, D. Li, R. Si, S. Miao, F. Zhang, and C. Li, "Synthesis and demonstration of subnanometric iridium oxide as highly efficient and robust water oxidation catalyst," *ACS Catalysis*, vol. 7, no. 9, p. 5983, 2017.
- [3] R. Badam, M. Hara, H.-H. Huang, and M. Yoshimura, "Synthesis and electrochemical analysis of novel IrO₂ nanoparticle catalysts supported on carbon nanotube for oxygen evolution reaction," *International Journal of Hydrogen Energy*, vol. 43, no. 39, p. 18 095, 2018.
- [4] G. Li, S. Li, M. Xiao, J. Ge, C. Liu, and W. Xing, "Nanoporous IrO₂ catalyst with enhanced activity and durability for water oxidation owing to its micro/mesoporous structure," *Nanoscale*, vol. 9, no. 27, p. 9291, 2017.
- [5] G. C. da Silva, M. R. Fernandes, and E. A. Ticianelli, "Activity and stability of Pt/IrO₂ bifunctional materials as catalysts for the oxygen evolution/reduction reactions," *ACS Catalysis*, vol. 8, no. 3, p. 2081, 2018.
- [6] I. I. Aysan, T. Gorkan, I. Ozdemir, Y. Kadioglu, G. Gökolu, and E. Aktürk, "Electronic structure, cohesive and magnetic properties of iridium oxide clusters adsorbed on graphene," *Journal of Molecular Graphics and Modelling*, vol. 101, p. 107 726, 2020.
- [7] B. Cordero *et al.*, "Covalent radii revisited," *Dalton Transactions*, no. 21, p. 2832, 2008.

Graphene oxide modified with iridium oxide

8.1 Introduction

A review of the literature reveals a scarcity of theoretical works dedicated to the study of the deposition of iridium oxides on oxidized carbon surfaces. Kong et al. [1] demonstrated in their experimental work that uniformly supported ultrafine IrO_2 nanoparticles (~ 1.7 nm) on a reduced graphene oxide (rGO) surface exhibit superior oxygen evolution reaction (OER) activity (2.3 times higher than that of commercial IrO_2), high OER durability, and excellent performance in long-term water electrolysis. However, the authors ascribe the enhanced durability to a strong interaction between the particles and the π -electrons of the rGO. The results for $(\text{IrO}_2)_n/\text{CNT}$ described in the previous chapter indicate that such non-covalent interactions may not be particularly robust. This is in line with Aysan et al. [2], which showed that $(\text{IrO}_2)_n$ ($n = 1 - 5$) clusters present a weak interaction with the pristine graphene sheet, and that no bonding is observed between the Ir or O atoms in the particle and the C atoms on the surface. Consequently, it can be hypothesized that non-reduced graphene oxide surface (GO) may offer superior properties as a substrate for iridium oxide particles, as suggested in the experimental work of Korkmaz et al. [3].

Under these considerations, in this chapter the deposition of iridium oxide onto the oxidized regions of the GO model was exclusively examined utilizing the O atoms of the carbon material as binding sites for the Ir atoms in the particles. The interaction between the O atoms of the nanoparticles and the GO surface was not considered, given that these peroxo bonds would entail significantly higher formation energy. Given the polar nature of the substrate, GA-derived iridium oxide particles were selected for this matter. This choice was made due to the greater polarization of Ir–O bonds in these nanoparticles, which can be attributed to their “core-shell-like” structures. As expected, the number of possible surface–nanoparticle interaction configurations increased in direct proportion to the quantity of Ir atoms (and therefore, the size) of the particles. All oxygen atoms from the GO sheet model (whether $\text{O}^{\text{hydroxyl}}$ or O^{epoxy}) were considered as binding points for each nanoparticle

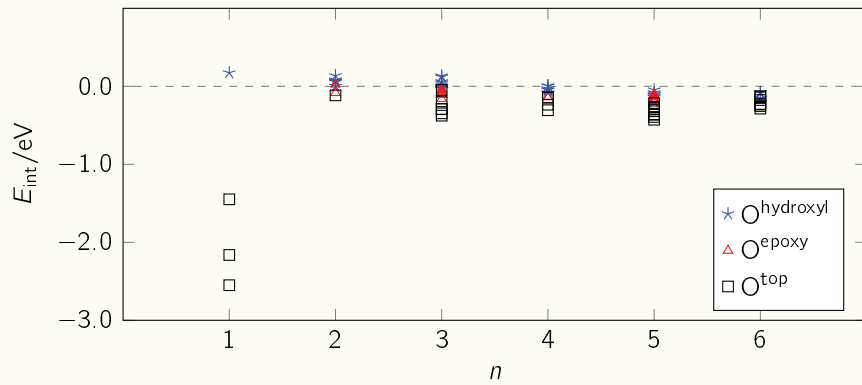


Figure 8.1: Interaction energies of $(\text{IrO}_2)_n/\text{GO}$ systems for different binding sites ("hydroxyl", "epoxy" and "top" oxygens) and nanoparticle sizes.

interaction site resulting in about 90 initial models, many of which were found to be energetically unstable after structure optimization. The interest of this chapter is solely directed towards the scenarios where stable bonding interactions were formed between iridium oxide nanoparticles and the GO surface, without changing the stoichiometry of each component except for the newly formed (single) bond.

8.2 Results and discussion

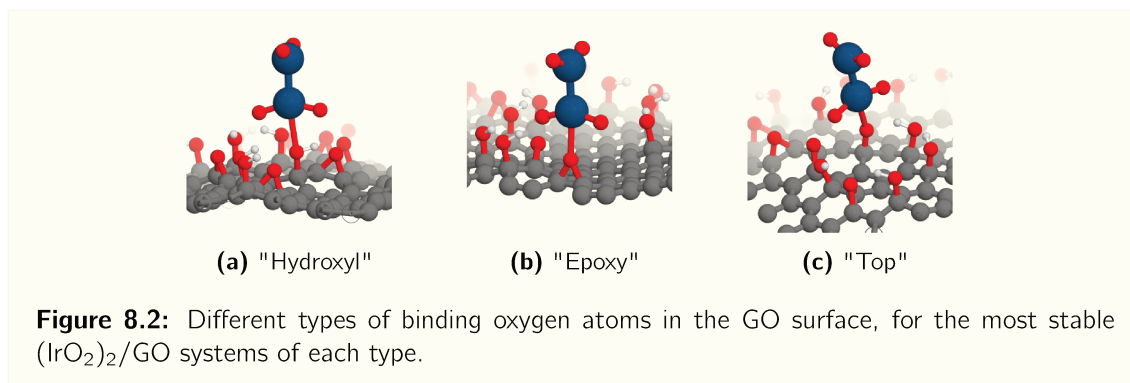
The energy change resulting from the interaction between the nanoparticles and the surface (E_{int}) was computed according to the eq. 8.1,

$$E_{\text{int}} = [E_{(\text{IrO}_2)_n/\text{GO}} - E_{\text{GO}} - E_{(\text{IrO}_2)_n}] / n \quad (8.1)$$

where $E_{(\text{IrO}_2)_n/\text{GO}}$, E_{GO} and $E_{(\text{IrO}_2)_n}$ are the total energies of the iridium oxide-modified surface, the pristine surface and the $(\text{IrO}_2)_n$ nanoparticle, respectively, and n is the number of IrO_2 units in the particle.

Fig. 8.1 shows the interaction energies of all the stable ($E_{\text{int}} < 0$ eV) and near-stable ($0 \text{ eV} \leq E_{\text{int}} < 0.25$ eV) systems, differentiated by the type of binding oxygen on the GO surface after the iridium oxide deposition. These oxygen atoms can be separated in three groups: "hydroxyl", "epoxy" and "top". In the first two groups, the configuration of the oxygen atoms are similar to the ones found in the unmodified GO sheet. Instead, the "top" group represents the binding oxygen atoms that arises from the breaking of an "epoxy" oxygen to form a new bond with the iridium oxide nanoparticle. These three different types of oxygen atoms are depicted in Fig. 8.2 for the case of the $(\text{IrO}_2)_2$ cluster, each corresponding to the most stable system of its group.

The interaction energies and geometrical configurations of the most stable adsorbed systems for each type of binding oxygen and particle size are listed in Table 8.1. The most stable adsorptions are given with the oxygen atoms in a "top" configuration. Furthermore, stable binding to "hydroxyl" oxygen atoms is only possible for $n \geq 4$, and binding to an "epoxy" oxygen is rare among the stable systems. This suggests that the C–O–Ir bond stability is negatively affected by additional bonds (i.e. other



than Ir–O) on the binding oxygen. In the most stable systems, an "epoxy" oxygen of GO breaks one of the C–O bonds in favor of the formation of an Ir–O bond, as the whole process is characterized by a decrease in the total energy of the system.

The adsorbed systems were subjected to an atomic charge population analysis using the DDEC6 method. Bond order analysis results were used to characterize the newly formed nanoparticle–surface bond in each case.

For $n = 1$ and $n \geq 3$ nanoparticles, a single bond (with bond order ~ 1.0) is found between the binding Ir and the surface oxygen. However, the adsorption of $(\text{IrO}_2)_2$ is markedly different. In contrast with the $n > 2$ particles, the strong Ir–Ir bond (bond order 1.7) found in the $(\text{IrO}_2)_2$ nanoparticle reduces the interaction of the iridium atom with the oxygen atom of the GO in 60% (resulting in a bond order of 0.4). This interaction is only present on the $(\text{IrO}_2)_2$ configuration, as direct Ir–Ir bonding (i.e. without participation of O atoms) is not found in the larger nanoparticles.

8.3 Summary

This chapter introduces the results and further analysis of the deposition of a variety of iridium oxide nanoparticles, $(\text{IrO}_2)_n$ ($n = 1 - 6$), onto a graphene oxide (GO) surface model. Considering the weaker interactions found (and reported in literature) between the particles and the non-oxidized regions, the deposition of the nanoparticles was made extensive to all O atoms (i.e. "hydroxyl" and "epoxy") of the GO surface to gain a more comprehensive understanding. The results demonstrated that the most stable adsorption modes are achieved through the rupture of an "epoxy" oxygen of GO, favoring the formation of a new Ir–O bond. This process is observed to occur consistently, regardless of the size of the particle. This chemisorption mechanism offers a more insightful understanding of the experimental observations reported by Korkmaz et al. [3].

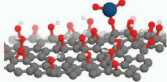
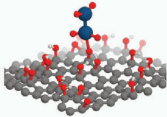
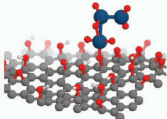
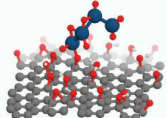
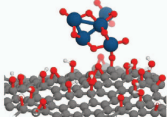
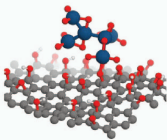
Size	Configuration	E_{int}
$n = 1$		-2.56 eV
$n = 2$		-0.12 eV
$n = 3$		-0.38 eV
$n = 4$		-0.31 eV
$n = 5$		-0.43 eV
$n = 6$		-0.29 eV

Table 8.1: Most stable adsorbed configurations of the $(\text{IrO}_2)_n/\text{GO}$ ($n = 1 - 6$) systems. The interaction energy (E_{int}) of each system is listed on the side.

References for Chapter 8

- [1] F.-D. Kong, S. Zhang, G.-P. Yin, J. Liu, and Z.-Q. Xu, "IrO₂–graphene hybrid as an active oxygen evolution catalyst for water electrolysis," *International Journal of Hydrogen Energy*, vol. 38, no. 22, p. 9217, 2013.
- [2] I. I. Aysan, T. Gorkan, I. Ozdemir, Y. Kadioglu, G. Gökolu, and E. Aktürk, "Electronic structure, cohesive and magnetic properties of iridium oxide clusters adsorbed on graphene," *Journal of Molecular Graphics and Modelling*, vol. 101, p. 107 726, 2020.
- [3] S. Korkmaz, F. M. Tezel, and. Kariper, "Synthesis and characterization of go/IrO₂ thin film supercapacitor," *Journal of Alloys and Compounds*, vol. 754, p. 14, 2018.

Water adsorption and dissociation on Pt_n/CNT

9.1 Introduction

The dissociation of water molecules into hydrogen (H) and hydroxide (OH) ions on catalytic surfaces is a pivotal reaction in electrochemical water splitting. Effective catalysts, such as platinum, facilitate this process by providing active sites that lower the activation energy needed to break the O-H bonds in water molecules. Research has shown that platinum surfaces, due to their unique electronic properties, can significantly enhance the efficiency of this dissociation reaction, leading to improved hydrogen production rates [1].

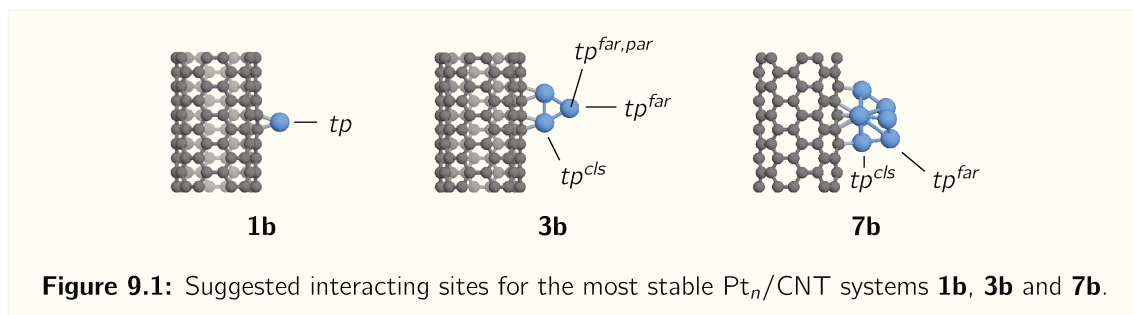
Water dissociation has been deeply studied for several material types and geometries and are well documented [2–4]. Phatak et al. [2] investigated the dissociation of water on (111) surfaces of five metals (Cu, Au, Ni, Pd and Pt). The authors found the lowest barrier for Pt(111) (0.75 eV). Similarly, other authors have also studied this reaction on noble metal surfaces such as Pt and Pd, for which they found high activation energies for flat surfaces [3, 5], while on stepped and kinked surfaces the presence of low coordinated atoms suggests a decrease in the energy barrier of the process [3]. In addition, the reaction on platinum nanoparticles with 13 to 40 atoms in the gas phase was studied theoretically by Fajín et al. [4]. The authors reported that a water molecule preferentially adsorbs to the low coordinated atoms at the edges of the particle. In addition, since the activation energies were lower than those of a Pt(111) surface in all cases studied, the authors suggest that only small Pt nanoparticles can promote water dissociation under working conditions. More recently, Bazhenov et al. [6] have also developed theoretical models for two types of nanoparticles, Pt₅₅ and Pt₁₄₇, where the water adsorption was found to be strongly dependent on the nature of the surface sites in terms of coordination and *d*-band structure. In particular, they report that the energy of the transition state increases linearly with the coordination number of the surface sites in the nanoparticle and with the water adsorption energy, while it decreases linearly with the increase in the *d*-band center of the site.

In practice, fuel cells with an ultra-low platinum content are already being scaled up to the production stage with outstanding results (see, for example, [ULPHE-PEM fuel cells of "Jalvasub engineering"](#)). In addition, carbon-based catalysts with ultra-low platinum loading are becoming increasingly important in the field of catalysis, particularly for applications such as fuel cells and electrocatalysis. These catalysts leverage the advantageous properties of carbon materials to reduce the amount of platinum needed while maintaining high catalytic performance. This is especially critical given the high cost of platinum, which poses significant economic challenges for its widespread use. Recent research has demonstrated that optimizing the structure and morphology of carbon-supported platinum catalysts can lead to remarkable enhancements in catalytic activity, even with minimal platinum loadings [7–10]. By lowering the cost and improving the performance of catalysts, these new materials are key to accelerating the adoption of clean hydrogen technologies and mitigating climate change impacts.

In this context, some works on platinum-modified carbon materials are worthy of mention here. It has been reported that the adsorption of small Pt clusters, containing 1, 3, 4, 5, 7, 9 and 13 atoms, on CNTs of different chiralities is energetically favored [11–16]. The metal-carbon interaction usually involves electronic charge transfer, as well as a significant charge delocalization and metal *d*-band modification, both factors with incidence on the electrocatalytic properties of the hybrid material [13]. On the other hand, the adsorption of small molecules such as H₂O, H₂S and H₂ on pristine CNTs surfaces is energetically poorly favored [17, 18], while this interaction notably improves with the presence of metallic clusters [11, 14, 15]. Such metallic nanostructures have a higher amount of low-coordinated sites, which have proven to be very important in electrochemistry, as they can stabilize reaction intermediates, as H and OH [19]. Moreover, Tavakkoli et al. [20] have shown both theoretically and experimentally that it is possible to synthesize single-walled CNTs with ultra-low amounts of platinum (i.e., atomically dispersed Pt). This material exhibited remarkable electrocatalytic properties for the HER (hydrogen evolution reaction), reaching and even exceeding those of conventional Pt/C electrodes. In addition, Kim et al. [16] came to similar conclusions regarding Pt/CNT catalysts, considering the HOR (hydrogen oxidation reaction) of a PEMFC (proton exchange membrane fuel cell) anode. Similar systems were also addressed by means of DFT calculations.

However, in spite of the efforts in understanding the process, some details of the reaction path and nanoparticle size/shape effects are still not clear. In this regard, the aim of the studies presented in this chapter is to contribute to the ongoing discussion and consider the water adsorption and further dissociation as a probe reaction to understand the nanostructure reactivity and the factors that might influence the process at an atomic scale.

Regarding the computational modeling of the material, in order to avoid CNT deformations, which might lead to unexpected and non-systematic results out of the scope of this thesis, the C atom positions were kept fixed during geometric optimizations, excepting those first, second and third neighbors of the adsorbed Pt_{*n*} nanoparticles. On the other hand, unless otherwise indicated, the positions of the Pt, O and H atoms of both the particles and the water molecule were optimized in all directions. This choice of configurations is therefore aimed to the study of the physicochemical interactions between the different parts of the system, particularly between the Pt_{*n*} and the water molecule, and the local effects of the particles on the carbon nanotube surface.



9.2 Results and discussion

9.2.1 Water molecule adsorption

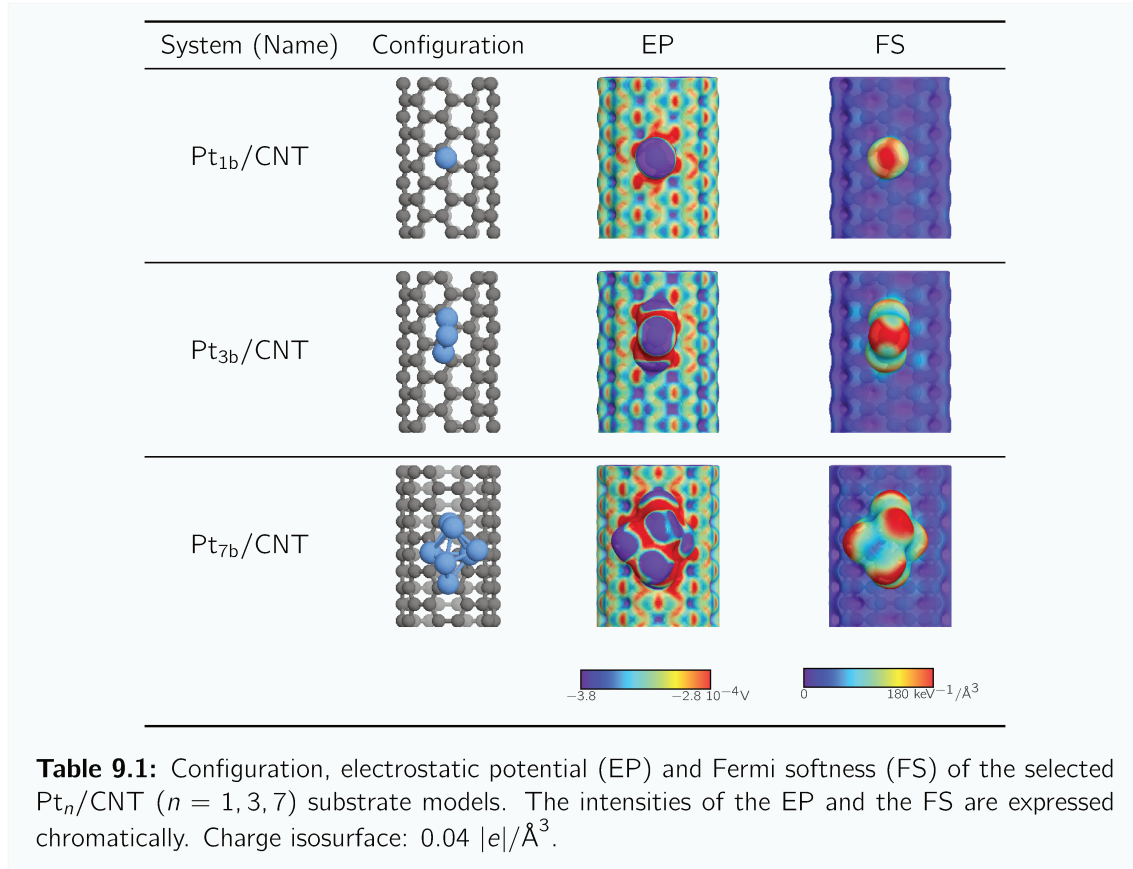
To focus the study on the potential particle–surface synergic effect, this chapter presents an analysis of water adsorption and dissociation on a representative selection of Pt_1/CNT , Pt_3/CNT and Pt_7/CNT systems, considering that including larger Pt_n particles would dilute the effect of the interface. For this matter, the Pt_n/CNT systems were chosen according to their stability. Table 9.1 presents the selected systems, respectively labeled as **1b**, **3b** and **7b**, along with their electrostatic potential (EP) and localized Fermi softness (FS) surfaces.

In accordance with the existing literature [3, 4], the adsorption of a water molecule was proposed at "top" (tp) sites of the platinum atoms of the nanoparticles. In addition, the EP and FS plots aided to analyze the water molecule adsorption sites, which are presented in Fig. 9.1. In the case of Pt_{1b}/CNT , a single adsorption site was proposed, consistent with the lowest EP and highest FS region (see Table 9.1). In order to analyze the effect of the CNT, two different water adsorption sites were proposed for the larger Pt_{3b}/CNT and Pt_{7b}/CNT systems: one closer and the other further from the carbon surface (namely " cls " and " far ", respectively). An approach similar to that of the Pt_{1b}/CNT system has been taken for Pt_{7b}/CNT , considering that EP and FS plots seemingly point toward similar adsorption sites in radial directions with respect to the metal particle. For Pt_{3b}/CNT , instead, three different binding locations were suggested: two in a radial direction (i.e. in the same plane of the Pt_3 particle), and the other parallel to the nanoparticle plane (referred to as " par "). The first two adsorption modes were proposed in accordance with the Pt_{3b}/CNT EP plot, while the latter was suggested in alignment with the FS plot (see Table 9.1).

Water molecule adsorption energies were calculated according to eq. 9.1,

$$E_{ads} = E_{H_2O/Pt_n/CNT} - E_{Pt_n/CNT} - E_{H_2O} \quad (9.1)$$

where $E_{H_2O/Pt_n/CNT}$, $E_{Pt_n/CNT}$ and E_{H_2O} represent the electronic energies of the total system, the Pt_n/CNT substrate and the water molecule in gas-phase, respectively. Results concerning adsorption energies for the studied systems are summarized in Table 9.2. It is possible to observe from these results that water adsorption energies on cls sites are in the order of ~ -0.4 eV, while the corresponding values for the far sites lie in the -1.1 to -0.7 eV range. The par adsorption mode, on the other hand, resulted in a weaker interaction between the water molecule and the proposed adsorbate, both in terms of energy and atomic overlap. In this case, the platinum–oxygen distance



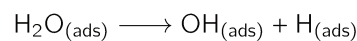
(2.8 Å) increased substantially compared to the other systems (~ 2.3 Å). The reported Pt–O^w distance for the *par* mode thus suggests that the configuration is on the borderline between adsorption and physisorption, since it is about 40 % larger than the sum of the reported covalent radius of both the oxygen and platinum atoms [21]. Furthermore, the adsorption energies for the in-plane modes keep a good relation with the Pt–O^w distances, as illustrated in Fig. 9.3 and in the results of the linear fit in eq. 9.2, emphasizing the difference with the *par* adsorption mode.

$$d_{\text{Pt-O}^w} = 2.4697 + 0.2881E_{\text{ads}} \quad , \quad R^2 = 0.9970. \quad (9.2)$$

It is also important to note that the results of water molecule adsorption in the *par* mode indicate that the H₂O–Pt_n/CNT interaction appears to be governed by electrostatic forces, leading to highly polarized covalent bonds. This is further supported by the fact that this interaction is particularly weak in the region where, according to the FS plot, more reactive electronic states are observed. Instead, the evidence suggests that the chemisorption of water occurs between the high EP regions of the H₂O molecule (located close to the oxygen atom, see Fig. 9.2) and the low EP regions of the CNT-deposited Pt_n.

9.2.2 Water molecule dissociation

As a starting point, the reaction step



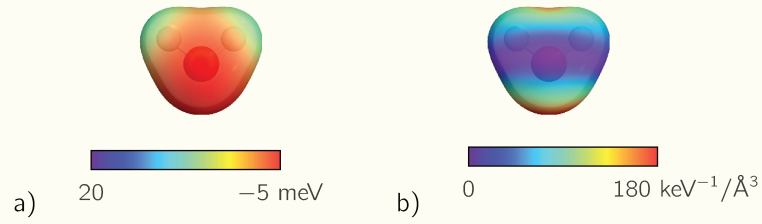


Figure 9.2: Electrostatic potential (a) and localized Fermi softness (b) surfaces of the isolated water molecule. Charge isosurface: $0.04 |e|/\text{\AA}^3$.

Substrate	Site	E_{ads}/eV	$d_{\text{Pt}-\text{O}^w}/\text{\AA}$	Pt–O ^w ovlp./ e
Pt _{1b} /CNT	tp	−1.12	2.14	0.48
Pt _{3b} /CNT	$tp^{\text{far},\text{par}}$	−0.33	2.82	0.08
Pt _{3b} /CNT	tp^{cls}	−0.44	2.34	0.34
Pt _{3b} /CNT	tp^{far}	−0.65	2.29	0.39
Pt _{7b} /CNT	tp^{cls}	−0.35	2.36	0.35
Pt _{7b} /CNT	tp^{far}	−0.95	2.20	0.48

Table 9.2: Adsorption energy (E_{ads}), Pt–water oxygen distance ($d_{\text{Pt}-\text{O}^w}$), Pt–O^w atomic overlap results for the proposed H₂O/Pt_n/CNT configurations.

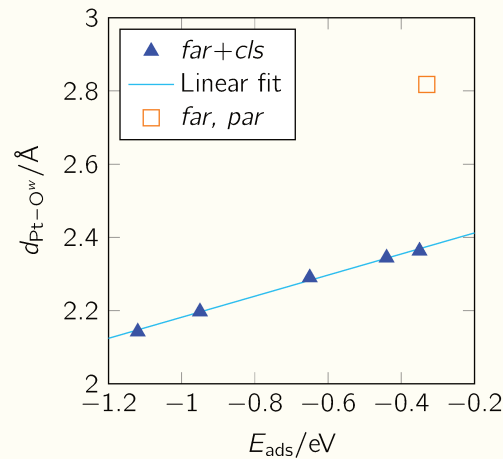


Figure 9.3: Platinum–water distances ($d_{\text{Pt}-\text{O}^w}$) as a function of the adsorption energies (E_{ads}) for in-plane (blue triangle marks) and parallel (orange square mark) adsorption modes. A linear fit of the first group is included.

has been explored on different sites of Pt_{1b}, Pt_{3b} and Pt_{7b} supported particles to investigate the effects of particle size, shape, metal–carbon interface and how these factors affect the kinetics of the H–OH bond breaking to clarify some mechanistic insights that determine the catalytic activity of the materials. These reaction paths were analyzed by means of the CI–NEB method, taking stable adsorbed water configurations as initial states (IS). For this matter, the adsorption energy differences were computed for each image as of eq. 9.3,

$$\Delta E_{\text{ads}}^i = E_{\text{ads}}^i - E_{\text{ads}}^{\text{IS}} \quad (9.3)$$

where the E_{ads} values were calculated following eq. 9.1, the superscript i indicates the image number in the reaction path, and IS corresponds to the initial state image. The results are summarized in Table 9.3 and detailed below. Values in boldface correspond to activation energies, computed as of eq. 9.4,

$$E_{\text{act}} = E_{\text{ads}}^{\text{TS}} - E_{\text{ads}}^{\text{IS}} \quad (9.4)$$

where $E_{\text{ads}}^{\text{TS}}$ correspond to the transition states adsorption energies.

For the Pt_{1b}/CNT substrate, only one water adsorption mode was suggested, and thus a single dissociation path was subsequently considered. The H–OH scission occurred on top of a single platinum atom, which resulted in a prohibitively high activation energy (0.8 eV). The final state (FS) configuration therefore presented H and OH species adsorbed on the same Pt atom.

The larger nanoparticles offer alternative reaction pathways, provided that the dissociated hydrogen can be transferred to a neighboring platinum atom, thus avoiding the formation of new bonds on the same platinum atom as in the case of Pt_{1b}. In such pathways, dissociation might occur at the intermetallic bridge sites. In this line, four additional reaction paths have been suggested, i.e. two for each of the Pt_{3b} and Pt_{7b} systems, where $\text{H} \rightarrow \text{Pt}^{\text{cls}}$ and $\text{H} \rightarrow \text{Pt}^{\text{far}}$ migrations were considered (with the water molecule being adsorbed in the opposite *far* or *cls* site, respectively). The activation energies presented in Table 9.3 indicate that the proximity of the water adsorption site to the carbon surface has a significant impact on the activation energy for the Pt_{3b} particle. However, this is not observed for the Pt_{7b}/CNT system, suggesting that the carbon nanotube effect is less pronounced with larger nanoparticles.

Furthermore, Fig. 9.4 illustrates the adsorption energy results for each of the examined CI–NEB images. From this, it is possible to observe that the final states energies are not considerably different from that of the corresponding initial states for those paths where an H atom is translocated to a neighboring Pt atom (Pt_{3b} and Pt_{7b} systems). Moreover, as seen with the IS, the FS corresponding to water molecules initially adsorbed at *cls* sites showed less stable configurations when compared to systems where water was adsorbed at *far* sites. In this line, the further reactivity of such $\text{H}_{(\text{ads})}$, $\text{OH}_{(\text{ads})}$ species is expected to improve in vicinity of the metal–carbon interface.

To gain further insight into the observed reactivity of the water molecule on the Pt_{3b}/CNT and Pt_{7b}/CNT systems substrates, Table 9.4 presents the net atomic charges of the platinum atoms (obtained via the DDEC6 method) and the charge density differences, computed as per eq. 9.5

$$\Delta\rho(\mathbf{r}) = \rho_{\text{Pt}_n/\text{CNT}}(\mathbf{r}) - \rho_{\text{CNT}}(\mathbf{r}) - \rho_{\text{Pt}_n}(\mathbf{r}) \quad (9.5)$$

Image	Pt _{1b}		Pt _{3b} , H→Pt ^{far}		Pt _{3b} , H→Pt ^{cls}	
	$\Delta E_{\text{ads}}/\text{eV}$	$\nu^{\text{O-H}}/i$	$\Delta E_{\text{ads}}/\text{eV}$	$\nu^{\text{O-H}}/i$	$\Delta E_{\text{ads}}/\text{eV}$	$\nu^{\text{O-H}}/i$
IS	0.000		0.000		0.000	
01	0.082		0.017		0.012	
02	0.371		0.049		0.093	
03	0.823	999 cm ⁻¹	0.173		0.861	1049 cm ⁻¹
04	0.658		0.332	379 cm ⁻¹	0.411	
05	0.470		0.062		-0.069	
FS	0.436		-0.079		-0.174	

Image	Pt _{7b} , H→Pt ^{far}		Pt _{7b} , H→Pt ^{cls}	
	$\Delta E_{\text{ads}}/\text{eV}$	$\nu^{\text{O-H}}/i$	$\Delta E_{\text{ads}}/\text{eV}$	$\nu^{\text{O-H}}/i$
IS	0.000		0.000	
01	0.060		0.017	
02	0.301		0.161	
03	0.491	598 cm ⁻¹	0.463	677 cm ⁻¹
04	0.401		0.182	
05	0.281		0.043	
FS	0.208		0.030	

Table 9.3: CI-NEB results corresponding to water dissociation paths on the studied systems. Adsorption energy differences (ΔE_{ads}^i) for each image are shown. The activation energies are indicated in boldface, and the O–H vibrational modes frequencies at the corresponding transition states ($\nu^{\text{O-H}}$) are listed.

where $\rho_{\text{Pt}_n/\text{CNT}}$, ρ_{CNT} and ρ_{Pt_n} are the electronic charge densities corresponding to the total system, the carbon nanotube, and the platinum particle in gas phase, respectively. The electronic charges of the platinum particle in the Pt_{3b}/CNT system exhibit a notable charge polarization, with an accumulation (higher localization) observed in the outermost Pt atom. The particle polarization is much more subtle in the Pt_{7b}/CNT system. The charge readjustment that gives rise to this polarization emerges from the particle–CNT interaction, as evidenced in the charge density difference plots. The extent of the carbon substrate effect is thus conditioned by the platinum particle size and shape. Therefore, the CNT-induced Pt_{3b} nanoparticle polarization seems to be directly linked to its capacity to split the water molecule into H_(ads) and OH_(ads) species with a minimal energy barrier.

9.3 Summary

This chapter assesses the catalytic capabilities of the Pt_n/CNT material through an evaluation of its performance in key test reactions, namely water adsorption and further dissociation pathway. The geometry, size, and charge relocation between the platinum particles and the carbon support play an important role in determining the adsorption and activation energies of the processes.

The results indicate that the H₂O–Pt_n/CNT interaction appears to be governed by electrostatic forces, leading to highly polarized covalent bonds. This conclusion is supported by the analysis of the Fermi softness and electrostatic potential surfaces of both the water molecule and the CNT-supported platinum nanoparticle. In addition, the dissociation phenomenon involving the Pt/CNT interface is

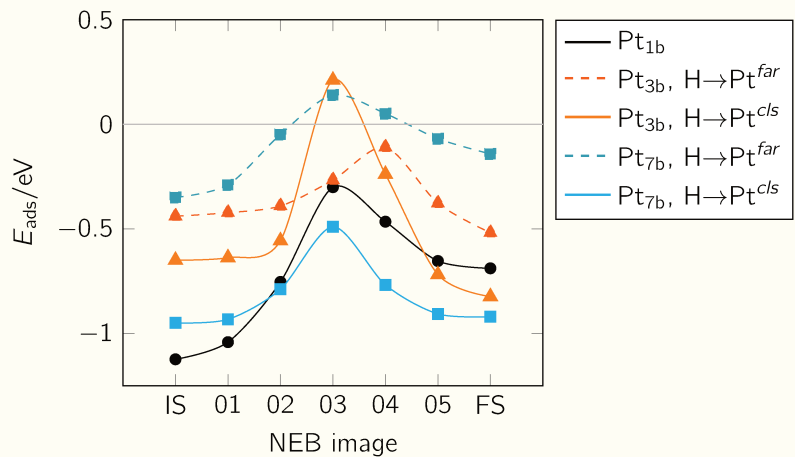


Figure 9.4: Adsorption energies (E_{ads}) of the studied reaction paths as a function of the NEB image number.

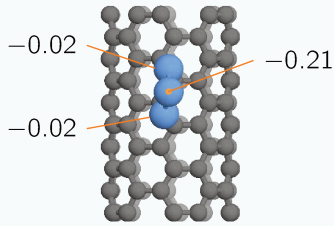
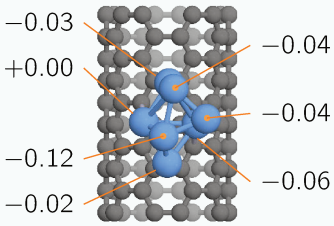
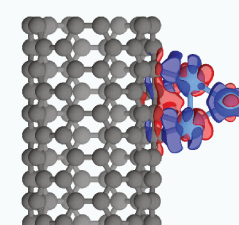
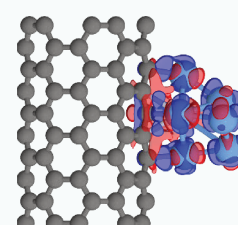
	Pt _{3b} /CNT	Pt _{7b} /CNT
Atomic charges		
CDD		

Table 9.4: Net atomic charges (DDEC6 method) and electronic charge density differences (CDD) of Pt_{3b}/CNT and Pt_{7b}/CNT systems. In the CDD plots, blue and red colors indicate regions with charge accumulation and depletion, respectively. Isovalue: 0.010 |e|/Å³.

more favorable than those in pure Pt(111) ($E_{\text{act}} \approx 0.8$ eV [2, 3]). This leads to lower activation energies, which can be modulated by the negative charge accumulation on a low-coordinated atom. The results of this study encourage experimentalists to synthesize stable Pt nanoparticles with triangular shapes to promote polarization and increase the efficiency of catalysis.

References for Chapter 9

- [1] J. Greeley, T. F. Jaramillo, J. Bonde, I. Chorkendorff, and J. K. Nørskov, "Computational high-throughput screening of electrocatalytic materials for hydrogen evolution," *Nature Materials*, vol. 5, no. 11, p. 909, 2006.
- [2] A. A. Phatak, W. N. Delgass, F. H. Ribeiro, and W. F. Schneider, "Density functional theory comparison of water dissociation steps on Cu, Au, Ni, Pd, and Pt," *Journal of Physical Chemistry C*, vol. 113, no. 17, p. 7269, 2009.
- [3] J. L. Fajin, M. N. D. S. Cordeiro, and J. R. Gomes, "Density functional theory study of the water dissociation on platinum surfaces: General trends," *Journal of Physical Chemistry A*, vol. 118, no. 31, p. 5832, 2014.
- [4] J. L. Fajin, A. Bruix, M. N. D. Cordeiro, J. R. Gomes, and F. Illas, "Density functional theory model study of size and structure effects on water dissociation by platinum nanoparticles," *Journal of Chemical Physics*, vol. 137, no. 3, 2012.
- [5] J. P. Clay, J. P. Greeley, F. H. Ribeiro, W. N. Delgass, and W. F. Schneider, "DFT comparison of intrinsic WGS kinetics over Pd and Pt," *Journal of Catalysis*, vol. 320, p. 106, 2014.
- [6] A. S. Bazhenov, L. Lefferts, and K. Honkala, "Adsorption and activation of water on cuboctahedral rhodium and platinum nanoparticles," *The Journal of Physical Chemistry C*, vol. 121, no. 8, p. 4324, 2017.
- [7] L. Huang *et al.*, "An integrated platinum-nanocarbon electrocatalyst for efficient oxygen reduction," *Nature Communications*, vol. 13, no. 1, p. 6703, 2022.
- [8] Z. Song *et al.*, "Ultralow loading and high-performing Pt catalyst for a polymer electrolyte membrane fuel cell anode achieved by atomic layer deposition," *ACS Catalysis*, vol. 9, no. 6, p. 5365, 2019.
- [9] Z. Xiang *et al.*, "Catalyst with a low load of platinum and high activity for oxygen reduction derived from strong adsorption of Pt–N₄ moieties on a carbon surface," *Electrochemistry Communications*, vol. 127, p. 107039, 2021.
- [10] C. Hao *et al.*, "Efficient catalyst layer with ultra-low Pt loading for proton exchange membrane fuel cell," *Chemical Engineering Journal*, vol. 472, p. 144945, 2023.
- [11] P. Pannopard, P. Khongpracha, M. Probst, and J. Limtrakul, "Gas sensing properties of platinum derivatives of single-walled carbon nanotubes: A DFT analysis," *Journal of Molecular Graphics and Modelling*, vol. 28, no. 1, p. 62, 2009.

- [12] D. H. Chi *et al.*, "Electronic structures of Pt clusters adsorbed on (5,5) single wall carbon nanotube," *Chemical Physics Letters*, vol. 432, no. 1-3, p. 213, 2006.
- [13] N. T. Cuong, A. Fujiwara, T. Mitani, and D. H. Chi, "Effects of carbon supports on Pt nano-cluster catalyst," *Computational Materials Science*, vol. 44, no. 1, p. 163, 2008.
- [14] N. T. Cuong, A. Sugiyama, A. Fujiwara, T. Mitani, and D. H. Chi, "Density functional study of Pt₄ clusters adsorbed on a carbon nanotube support," *Physical Review B*, vol. 79, no. 23, p. 235 417, 2009.
- [15] X. Zhang, H. Cui, D. Chen, X. Dong, and J. Tang, "Electronic structure and H₂S adsorption property of Pt₃ cluster decorated (8,0) SWCNT," *Applied Surface Science*, vol. 428, p. 82, 2018.
- [16] T. Kim, Y. Kwon, S. Kwon, and J. G. Seo, "Substrate effect of platinum-decorated carbon on enhanced hydrogen oxidation in PEMFC," *ACS Omega*, vol. 5, no. 41, p. 26 902, 2020.
- [17] L. A. Elalfy, W. M. Hassan, and W. N. Akl, "Ab initio density functional theory investigation of the interaction between carbon nanotubes and water molecules during water desalination process," *Journal of Chemistry*, vol. 2013, no. 1, p. 813 592, 2013.
- [18] Y. S. Al-Hamdani, D. Alfe, and A. Michaelides, "How strongly do hydrogen and water molecules stick to carbon nanomaterials?" *Journal of Chemical Physics*, vol. 146, no. 9, 2017.
- [19] M. J. Kolb, F. Calle-Vallejo, L. B. Juurlink, and M. Koper, "Density functional theory study of adsorption of H₂O, H, O, and OH on stepped platinum surfaces," *Journal of Chemical Physics*, vol. 140, no. 13, 2014.
- [20] M. Tavakkoli *et al.*, "Electrochemical activation of single-walled carbon nanotubes with pseudo-atomic-scale platinum for the hydrogen evolution reaction," *ACS Catalysis*, vol. 7, no. 5, p. 3121, 2017.
- [21] B. Cordero *et al.*, "Covalent radii revisited," *Dalton Transactions*, no. 21, p. 2832, 2008.

Water adsorption and dissociation on $(\text{IrO}_2)_n/\text{CNT}$

10.1 Introduction

In this chapter, the interaction of water molecules with $(\text{IrO}_2)_n/\text{CNT}$ systems is studied following a similar approach to that used with Pt_n/CNT . As introduced in chapter 7, iridium oxide catalysts have shown exceptional activity in facilitating the water oxidation reactions, making them vital for efficient energy conversion and storage systems. Contrary to the Pt_n/CNT case, different species (i.e. both metallic and oxygen atoms) are present in the proposed catalyst, thus presenting a markedly different chemical environment, when compared with the platinum-modified nanotube supports, for water molecules adsorption and further dissociation. Moreover, on the one hand the oxygen atoms of the oxide structure might be crucial in the interaction with a water molecule, as these O species would provide an direct and natural binding site for a H atom dissociating from H_2O . On the other hand, the ability of iridium to form oxide compounds would help stabilizing dissociated oxygen species as $\text{OH}_{(\text{ads})}$.

With regard to the computational modeling of the material, in line with the approach outlined in the previous chapter, only the positions of the Ir, O and H atoms of both the particles and the water, as well as those first, second and third C atoms neighbors, were relaxed during geometry optimizations. Any exceptions to this are clearly indicated.

10.2 Results and discussion

10.2.1 Water molecule adsorption

Water molecule adsorption was considered on the most stable $(\text{IrO}_2)_n/\text{CNT}$ systems of each particle size, namely **1a** and **3b** (as described in Chapter 7). For each of them, exposed regions of iridium atoms were suggested as binding sites for the oxygen atom of the water molecule. This is based



Figure 10.1: Suggested interacting sites for the most stable $(\text{IrO}_2)_n/\text{CNT}$ systems (namely **1a** and **3b**) of each particle size.

Substrate	Site	E_{ads}/eV	$d_{\text{Ir}-\text{O}^{\text{w}}}/\text{\AA}$	Ir–C ovlp./ e	Ir–O ^w ovlp./ e
$(\text{IrO}_2)_{1\text{a}}^*/\text{CNT}$	{phys}	–0.18	3.49	0.55	0.04
$(\text{IrO}_2)_{1\text{a}}/\text{CNT}$	"top"	–0.18	2.25	0.64	0.17
$(\text{IrO}_2)_{3\text{b}}/\text{CNT}$	{phys}	–0.26	3.78	1.03	0.04
$(\text{IrO}_2)_{3\text{b}}/\text{CNT}$	"top"	–0.51	2.23	1.04	0.33

Table 10.1: Adsorption energy (E_{ads}), Ir–water oxygen distance ($d_{\text{Ir}-\text{O}^{\text{w}}}$), and Ir–C and Ir–O^w atomic overlap results for the proposed $\text{H}_2\text{O}/(\text{IrO}_2)_n/\text{CNT}$ configurations. The system in which some atomic positions were kept frozen during optimization is marked with an asterisk symbol (see details in the text).

on the consideration that the formation of direct $\text{O}^{\text{water}}-\text{O}^{\text{IrO}_x}$ interactions would otherwise require larger energies. Two sites were thus proposed as possible water binding sites, namely "top" and "side", which are presented in Fig. 10.1. This site selection will facilitate the analysis of the potential effects of the carbon nanotube on the water– $(\text{IrO}_2)_n$ interaction, as they differ in their proximity to the carbon surface.

For each proposed substrate and site, the water adsorption energies were calculated as of eq. 10.1,

$$E_{\text{ads}} = E_{\text{H}_2\text{O}/(\text{IrO}_2)_n/\text{CNT}} - E_{(\text{IrO}_2)_n/\text{CNT}} - E_{\text{H}_2\text{O}} \quad (10.1)$$

where $E_{\text{H}_2\text{O}/(\text{IrO}_2)_n/\text{CNT}}$, $E_{(\text{IrO}_2)_n/\text{CNT}}$ and $E_{\text{H}_2\text{O}}$ represent the electronic energies of the total system, the $(\text{IrO}_2)_n/\text{CNT}$ substrate and the water molecule in gas-phase, respectively. Results concerning adsorption energies for these systems are summarized in Table 10.1. It can be observed that water adsorption on "side" sites lead to physisorbed states in both $(\text{IrO}_2)_{1\text{a}}/\text{CNT}$ and $(\text{IrO}_2)_{3\text{b}}/\text{CNT}$ systems, suggesting that the carbon nanotube induces a negative effect on the water–particle interaction. In fact, during optimization the initially proposed $\text{H}_2\text{O}/(\text{IrO}_2)_{1\text{a}}/\text{CNT}$ configuration in the "side" site derived to a system where both H_2O and IrO_2 were separately physisorbed when all involved atoms were kept free. Thus, in order to maintain the desired $(\text{IrO}_2)_{1\text{a}}/\text{CNT}$ adsorbed configuration, in this case the C and Ir atom positions were kept frozen during optimization, which is indicated by an asterisk symbol in Table 10.1. It is also worth noting, however, that the need to freeze atoms in order to avoid the IrO_2 desorption unveils the weakness of such systems in the event of a perturbation as the one induced by the presence of the water molecule. Moreover, the magnitude of the $(\text{IrO}_2)_{1\text{a}}/\text{CNT}$ adsorption energies also points to a similar stability of the water molecule in chemisorbed and physisorbed states.

10.2.2 Water molecule dissociation

To continue with, those $\text{H}_2\text{O}/(\text{IrO}_2)_n/\text{CNT}$ systems presenting stable water chemisorption were selected to study the dissociation step by means of the CI-NEB method. According to the results of the previous section, the **1a** and **3b** configurations with a water molecule adsorbed at the "top" sites were taken as the initial states (IS) of each reaction path. The H_2O dissociation was considered as an hydrogen atom being translocated from the molecule to the iridium oxide nanoparticle. Several final states (FS) were suggested for this purpose, which can be categorized into two types, depending on whether the dissociated H atom binds to an Ir atom (represented as $\text{H} \rightarrow \text{Ir}$) or an O atom (represented as $\text{H} \rightarrow \text{O}$) of the metal oxide. Previous to the CI-NEB calculation, the proposed final states geometries were optimized, in order to assert the energetic stability of the systems. The dissociation energy, defined as of eq. 10.2,

$$E_{\text{dis}} = E_{\text{ads}}^{\text{FS}} - E_{\text{ads}}^{\text{IS}} \quad (10.2)$$

where $E_{\text{ads}}^{\text{FS}}$ and $E_{\text{ads}}^{\text{IS}}$ are the adsorption energies (see eq. 10.1) of the final and initial states, respectively, was computed for each path. The results are summarized in Table 10.2, where it can be observed that the formation of Ir-H bonds requires very large energies, in the order of 1 eV, whilst considerably more negative dissociation energies were found for those systems involving the formation of new O-H bonds. Therefore, the CI-NEB was only considered at $\text{H} \rightarrow \text{O}$ reaction paths. This dissociation mechanism can also be predicted in terms of electrostatic interactions, as the H regions in the water molecule presents a high EP (see Fig. 9.2), whereas the O atoms in the iridium oxide clusters lie within low EP zones (see Table 5.6).

Table 10.3 lists the adsorption energy differences results for each dissociation path and image after convergence, obtained as in eq.10.3,

$$\Delta E_{\text{ads}}^i = E_{\text{ads}}^i - E_{\text{ads}}^{\text{IS}} \quad (10.3)$$

where the superscript i indicates the image number in the reaction path. In addition, the transition states generated by this methodology were subjected to vibrational analysis and proven to have a single imaginary frequency in the new O-H bond direction, which magnitudes are also shown in Table 10.3. Values in boldface correspond to activation energies, computed as of eq. 10.4,

$$E_{\text{act}} = E_{\text{ads}}^{\text{TS}} - E_{\text{ads}}^{\text{IS}} \quad (10.4)$$

where $E_{\text{ads}}^{\text{TS}}$ correspond to the transition states adsorption energies. The activation energy values obtained for the different paths are quite small, given between 0.3 eV and 0.5 eV, which suggests that the $\text{H} \rightarrow \text{O}$ dissociation is kinetically favored in such systems. The order of these activation energies is accompanied with the corresponding stabilities of the initial and final states in the considered pathways, which can be asserted by means of the Bell-Evans-Polanyi (BEP) lineal relationship (eq. 10.5),

$$E_{\text{act}} = E_0 + \alpha E_{\text{dis}} \quad (10.5)$$

with E_0 and α being the line intercept and slope, respectively [1, 2]. Fig. 10.2b presents the summarized results of activation and dissociation energies, with the corresponding linear fit. These

Substrate	Site	Path	E_{dis}/eV
(IrO ₂) _{1a} /CNT	"top"	H→Ir	0.82
(IrO ₂) _{1a} /CNT	"top"	H→O	−0.04
(IrO ₂) _{3b} /CNT	"top"	H→Ir ¹	1.26
(IrO ₂) _{3b} /CNT	"top"	H→Ir ²	1.12
(IrO ₂) _{3b} /CNT	"top"	H→O ^{oxo}	−0.37
(IrO ₂) _{3b} /CNT	"top"	H→O ^{brg}	0.21

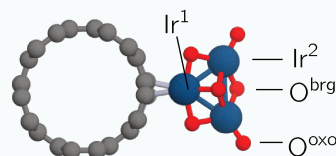


Table 10.2: Dissociation energy (E_{dis}) results of dissociated states for the selected H₂O/(IrO₂)_n/CNT dissociation paths. Different sites Ir¹, Ir², O^{oxo}, O^{brg} are also illustrated in the figure next to the table.

Image	(IrO ₂) _{1a} , H→O		(IrO ₂) _{3b} , H→O ^{oxo}		(IrO ₂) _{3b} , H→O ^{brg}	
	$\Delta E_{\text{ads}}/\text{eV}$	$\nu^{\text{O-H}}/i$	$\Delta E_{\text{ads}}/\text{eV}$	$\nu^{\text{O-H}}/i$	$\Delta E_{\text{ads}}/\text{eV}$	$\nu^{\text{O-H}}/i$
IS	0.000		0.000		0.000	
01	0.003		0.026		0.048	
02	0.073		0.330	1288 cm ^{−1}	0.195	
03	0.452	1256 cm ^{−1}	−0.006		0.493	874 cm ^{−1}
04	0.136		−0.217		0.357	
05	−0.027		−0.337		0.265	
FS	−0.038		−0.367		0.212	

Table 10.3: CI-NEB results corresponding to water dissociation paths on the studied systems. Adsorption energy differences (ΔE_{ads}^i) for each image are shown. The activation energies are indicated in boldface, and the O–H vibrational modes frequencies at the corresponding transition states ($\nu^{\text{O-H}}$) are listed.

results seem to be well described by the BEP relation, in the form given in eq. 10.6,

$$E_{\text{act}} = 0.4434 + 0.2861E_{\text{dis}} \quad , \quad R^2 = 0.9602. \quad (10.6)$$

The agreement with the BEP relationship can be explained by the chemical similitude of the reaction paths. Assuming that the validity of eq. 10.6 can be extended to the water dissociation on larger (but still comparable) CNT-supported iridium oxide nanoparticles, this would imply that H→O pathways would become kinetically favored in sites where stronger dissociation energies are promoted, i.e. by stabilizing the newly formed Ir–OH group and/or destabilizing the water molecule adsorption. The second mechanism would be preferred, however, taking into account the Sabatier's principle, as the increased stability of hydroxyl groups would also reduce their reactivity in further steps.

In addition, the atomic bond order (b.o.) values of the receiving O atoms in the initial states also seem to be well correlated with the corresponding activation energies in each path (see Fig. 10.2c), suggesting that oxygen species with lower b.o. values might present more energetically favorable transition states. This can be explained by the ability of the less bound O atoms to form new bonds.

Fig. 10.3 presents the electronic charge density difference plots of transition states, computed here

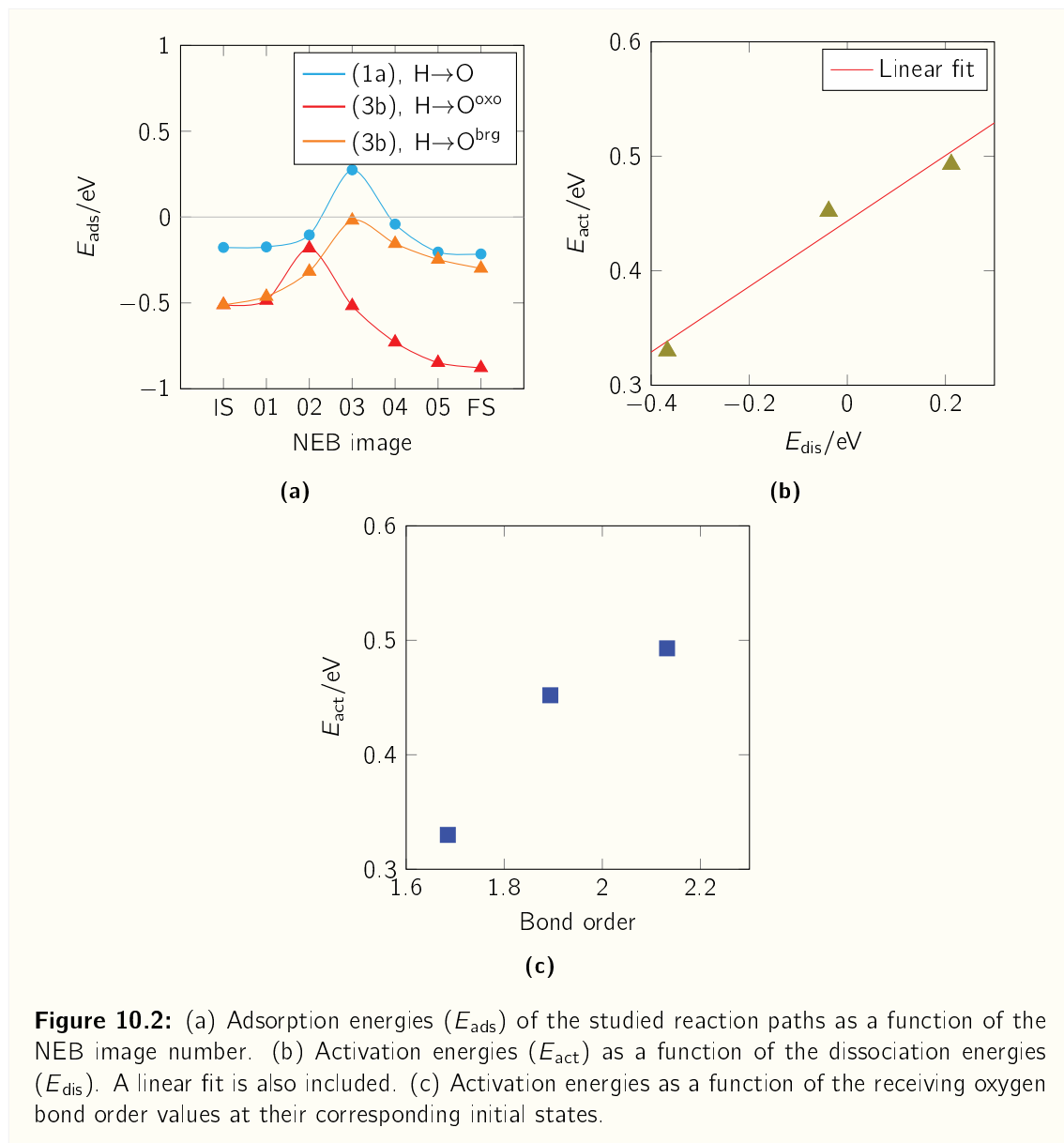
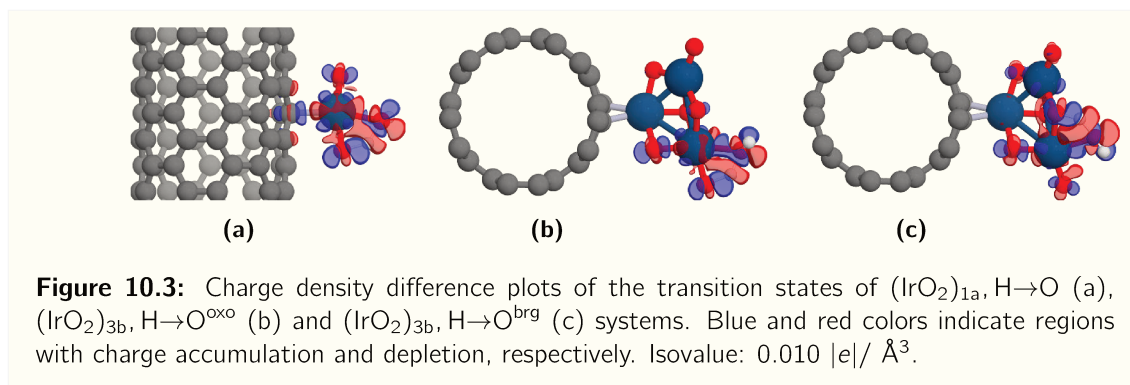


Figure 10.2: (a) Adsorption energies (E_{ads}) of the studied reaction paths as a function of the NEB image number. (b) Activation energies (E_{act}) as a function of the dissociation energies (E_{dis}). A linear fit is also included. (c) Activation energies as a function of the receiving oxygen bond order values at their corresponding initial states.



according to eq. 10.7

$$\Delta\rho(\mathbf{r}) = \rho_{\text{H}_2\text{O}/(\text{IrO}_2)_n/\text{CNT}}(\mathbf{r}) - \rho_{(\text{IrO}_2)_n/\text{CNT}}(\mathbf{r}) - \rho_{\text{H}_2\text{O}}(\mathbf{r}) \quad (10.7)$$

where $\rho_{\text{H}_2\text{O}/(\text{IrO}_2)_n/\text{CNT}}$, $\rho_{(\text{IrO}_2)_n/\text{CNT}}$ and $\rho_{\text{H}_2\text{O}}$ are the electronic charge densities corresponding to the total system, the iridium oxide–modified CNT, and the water molecule in gas phase, respectively. The last two systems were frozen at their corresponding transition state configurations. From Fig. 10.3, a strong charge relocalization is observed in the area where the water dissociation is taking place. Charge accumulation and depletion on the O–H bond regions undergoing the processes of formation and breaking, respectively, are evident in all systems. In addition, the presence of the water molecule induces electronic relocalization on the binding Ir atom and its first neighbors, i.e. O and C atoms for $(\text{IrO}_2)_{1a}/\text{CNT}$, and O and Ir atoms for $(\text{IrO}_2)_{3b}/\text{CNT}$. The charge relocalization is not accompanied of a noteworthy change of the atomic net charges of the $(\text{IrO}_2)_n/\text{CNT}$ species.

It has been reported that the water molecule binds strongly on penta–coordinated Ir sites of the IrO_2 rutile most stable (110) facet, and that the adsorbed water tends to dissociate spontaneously following a $\text{H} \rightarrow \text{O}^{\text{brg}}$ pathway [3]. In comparison, the results presented here for CNT supported iridium oxide nanoparticles suggest, on the one hand, moderated water binding (with adsorption energies between -0.2 eV and -0.5 eV) –which is in agreement with a good catalyst material according to Sabatier's principle– and, on the other hand, somewhat disfavored kinetics for the water dissociation paths (i.e. with activation energies between 0.3 eV and 0.5 eV). Nonetheless, a novel $\text{H} \rightarrow \text{O}^{\text{oxo}}$ path is described here, which is derived from the intrinsic chemical structure of such small particles, and whose least bound oxygen atom is suggested to provide the most stable transition and dissociated states for the considered reaction.

Therefore, it is worth noting that the analyzed pathways are kinetically favored with small activation energy barriers, which would put the iridium oxide–modified CNTs in a catalytic activity comparable to that of the rutile IrO_2 surface regarding water dissociation [3, 4], but with a much lower proportion of the precious metal oxide. In addition, considering the low particle–surface interaction (in terms of interaction energies and in charge relocalization) and the similarity of the presented activation energy values, it is possible to deduce that the CNT acts purely as a supporting material (i.e. with no synergic effect) by stabilization of the deposited nanoparticles.

10.3 Summary

In this chapter, water adsorption on the most stable $(\text{IrO}_2)_n^{\text{rutile}}/\text{CNT}$ systems has been studied, as well as different pathways for the dissociation step of adsorbed water. In particular, the migration of a H atom from the water molecule to both an Ir atom and an O atom of the metal oxide has been considered for each adsorption site. Very low energy barriers were found for the water dissociation on the rutile-derived $(\text{IrO}_2)_n$ deposited particles following $\text{H} \rightarrow \text{O}$ pathways. Considering what has been described in the previous chapter for $\text{H}_2\text{O}/\text{Pt}_n/\text{CNT}$, and that the H_2O adsorption and further H migration can be explained in terms of the particle electrostatic potential, it can be thought that the intrinsic charge polarization of the iridium oxide favors the water dissociation process. Moreover, the nanoparticles are able to maintain stable, covalent interactions with the carbon nanotube surface during the water dissociation.

References for Chapter 10

- [1] R. P. Bell, "The theory of reactions involving proton transfers," *Proceedings of the Royal Society of London. Series A-Mathematical and Physical Sciences*, vol. 154, no. 882, p. 414, 1936.
- [2] M. Mäkinen and K. Laasonen, "Density functional theory study of trends in water dissociation on oxygen-preadsorbed and pure transition metal surfaces," *Surface Science*, vol. 734, p. 122 305, 2023.
- [3] D. Gonzalez *et al.*, "Water adsorption on MO₂ (M=Ti, Ru, and Ir) surfaces. importance of octahedral distortion and cooperative effects," *ACS Omega*, vol. 4, no. 2, p. 2989, 2019.
- [4] M.-A. Ha and R. E. Larsen, "Multiple reaction pathways for the oxygen evolution reaction may contribute to IrO₂ (110)'s high activity," *Journal of The Electrochemical Society*, vol. 168, no. 2, p. 024 506, 2021.

Study of monometallic M_{13} nanoparticles

11.1 Introduction

Following the successful analysis and corroboration of the catalytic role of platinum and iridium oxide particles on carbon surfaces, it presents an interesting opportunity to extend the analysis to other types of nanoparticles. To begin with, it is essential to gain an understanding of the behaviour of gas-phase nanoparticles. A noteworthy line of research in this field is the one developed by Profs. Tielens and Bazin. This approach utilizes simple molecules, such as NO, N_2 , and O_2 , to analyze and comprehend the reactivity of metal clusters. In line with this objective, this thesis further examines M_{13} monometallic nanoparticles and their reactivity, with the aim of developing a comparable analysis in the future for M_{13} clusters on carbon-based surfaces.

As underlined by S.W. Chee et al. [1], the chemical conversion of small molecules on the surface of heterogeneous catalysts forms the backbone of many industrial processes in the modern chemical industry, such as electrocatalysis [2], photocatalysis [3] or the Fischer–Tropsch synthesis [4]. The intelligent design of heterogeneous catalysts needs a deep understanding of adsorption processes of different kinds of molecules at the surface of various supports [5] and in the case of DeNOx (a process aimed at reducing emissions of nitrogen oxides, NOx), it is clear that the interaction between molecules such as NO, O_2 and N_2 , and nanometer scale metallic clusters has to be investigated in detail [6, 7].

Regarding the adsorption of NO on nanometer scale metallic cluster, it is worth emphasizing that the validity of the d -band center has been assessed by Nanba et al. [8] and by Piotrowski et al. [9]. Nanba et al. have investigated the NO adsorption on $4d$ and $5d$ transition metal (Rh, Pd, Ag, Ir and Pt) NSMC (nanometer scale metallic cluster) through density functional theory (DFT) and supervised learning and noticed that the band center did not correlate well with the NO adsorption energy. Piotrowski et al. highlight that the general relationship based on the d -band model between

adsorption energy and the centroid of the occupied d -states does not hold for the studied transition metal M_{13} clusters, in particular, for clusters with low symmetry. Indeed, different papers underline the fact that the d -band center theory may not be efficient in the case of metallic clusters at nanometer scale [10, 11]. Such limitations regarding the interaction between NO and NSMC call for an original approach.

Following an approach defined and discussed by Boudart [12], a model based on experimental data is considered here, which establishes a relationship between the interaction mode of NO (non-dissociative or dissociative adsorption) and the behavior of nanometer scale metallic cluster (sintering or disruption) in response to this interaction [13, 14]. Such relationship is in line with the fact that, as underlined by several authors, catalysts restructure in response to changes in their reaction environment [15, 16]. Recent DFT studies on unsupported monometallic [17–19] and supported bimetallic [20] clusters have validated this relationship.

At this point, it is worth to underline that this relationship can be related to the Sabatier principle [21]. Such principle, widely used today as a key criterion in catalyst design, states that the binding energy between the catalyst and the reactant should be neither too strong nor too weak. More precisely, the catalyst and the reactant will hardly interact with each other if the bond is too weak. In the second configuration, the reactant will not desorb from the catalyst surface, if the bond is too strong, leading to an inhibition of further chemical reactions [22]. Thus, this second configuration can be related to the dissociative adsorption of NO on rhodium nanoparticles supported on alumina which leads to an oxidation of the metallic particle and finally to a definitive loss of the catalytic reaction. From an experimental point of view, it corresponds exactly to the results obtained by Campbell et al. [23].

Regarding the adsorption of N_2 or O_2 on nanometer scale metallic clusters, it is worth underlining that several publications which are associated with very exciting results and which are based on DFT calculations have already been published. For example, M. Boronat and A. Corma [24] have studied the adsorption and dissociation of molecular O_2 on extended gold surfaces, isolated gold nanoparticles of different size and shape, and small gold clusters supported on TiO_2 by means of DFT calculations. In some publications, a small number of metals namely Cu, Ag and Au have been selected [25]. Unfortunately, it is quite difficult to assess the fact that the reactivity of metal clusters for N_2 or O_2 depends on the position of the element in the periodic table if the number of selected metals is small. All these publications based on experimental data as well as on DFT simulations on a quite large number of metals (O_2 , $M = Ni, Cu, Ru, Rh, Pd, Ir$ and Pt for Oguz et al. 2019 [17]; M_{13} and M_{55} , $M = Ru, Rh, Pd$ and Ag for Takagi et al., 2019 [18]; M_{55} , $M = Fe, Co, Ni$ and Cu for Takagi et al., 2021 [19]; $Pt_{12}M$, $M = Ir, Ru$ or Rh for Vekeman et al., 2022 [20]) indicate that the reactivity of metal cluster for NO is determined by the energy and type ($4d$ or $5s$) of the valence band top, which both depend on the position of the element in the periodic table.

This chapter focuses in M_{13} nanometer scale metallic clusters of a large number of elements namely $M = Ag, Au, Co, Cu, Fe, Ir, Ni, Os, Pd, Pt, Rh$ and Ru to gain a deeper insight into their physical and chemical characteristics. To evaluate their reactivity, two small molecules such as O_2 and N_2 have been considered. In this context, a systematic investigation from the theoretical view point is presented here, where different adsorption configurations, interatomic distances as well as the

adsorption energies for both O₂ and N₂ on M₁₃ clusters are reported.

This chapter is organized as follows. First, the results of DFT calculations for each M₁₃ nanoparticle are presented: cohesive energies, metal–metal distances and *d*–band centers are estimated and analyzed following the periodic table. Finally, the particle chemistry for the adsorption of O₂ and N₂ is investigated by thermodynamics and fundamental chemical concepts such as overlap interaction, charge distribution and bond order. Concluding remarks are reported in the last section.

11.2 Results and discussion

11.2.1 M₁₃ nanoparticles: energetic and geometric considerations

In order to be able to systematically compare the behavior of the different metals when subjected to the same geometry, as well as their role in the interaction with O₂ and N₂ molecules, the structure of the monometallic M₁₃ nanoparticles (M = Ag, Au, Co, Cu, Fe, Ir, Ni, Os, Pt, Pd, Rh and Ru) was calculated from the Pt₁₃ most stable cluster as a starting point. The latter, shown in Fig. 11.1, was obtained from combining genetic algorithm methods and the VASP code. For all the M₁₃ clusters, cell parameters and bond lengths were proportionally relaxed from the Pt₁₃ structure in order to reach minimum–energy systems geometrically equivalent (i.e. the same shape) to the reference platinum particle. It should be noted that these M₁₃ structures are unlikely the most stable ones for any system different from Pt₁₃ which, in turn, is in great agreement with the literature [26]. The most stable structures of metallic M₁₃ particles are properly discussed elsewhere [26]. However, it is worth noting that the cohesive energies of the Ag₁₃, Au₁₃, Cu₁₃, Ir₁₃, Ni₁₃, Pd₁₃, Pt₁₃ and Rh₁₃ systems presented here do not present substantially large differences (≤ 166 meV) from those of global minima M₁₃ particles reported in ref. [26].

The Table 11.2 lists the cohesive energies, computed as shown in eq. 11.1

$$E_{\text{coh}} = (E_{\text{M}_{13}} - 13 \cdot E_{\text{M}}) / 13 \quad (11.1)$$

where $E_{\text{M}_{13}}$ and E_{M} are the total electronic energies of the M₁₃ nanoparticles and single M atoms in vacuum, respectively. Fig. 11.2 present the M₁₃ cohesive energies as well, including also the respective values reported for bulk systems [27]. These are systematically more negative than that of the M₁₃, as should be expected considering the chemical stability of the bulk systems. The cohesive energy difference between bulk and clusters decreases with the increasing electron number on the valence orbitals in each group of metals.

In addition, Table 11.1 includes the *d*–band centers values of the M₁₃ systems, evaluated according to eq. 11.2,

$$\epsilon^d = \frac{\int_{-\infty}^{E_{\text{Fermi}}} \rho^d(E) E \, dE}{\int_{-\infty}^{E_{\text{Fermi}}} \rho^d(E) \, dE} \quad (11.2)$$

where $\rho^d(E)$ is the electronic density of *d* states as a function of the total energy *E*.

Fig. 11.4 allows the comparison of the *d*–band centers values of the M₁₃ clusters presented in this thesis and the reported values corresponding to bulk [27] and surface [28] systems. While both bulk and surface *d*–band centers tend to decrease from left to right, for the M₁₃ particles the first three

elements within each group show increasing ϵ^d values, followed by a significant drop for the so-called "coin-metals" (Cu, Ag, Au), which, in turn, present closer values to bulk and surface systems. In addition, it is interesting to note the lower d -band centers found for Fe, Co, Ru, Os particles with respect to the reported values. This may be related to a structural aspect, considering that these are the only non-*fcc* metals of the investigated set in their bulk form. For the rest of the metals (excepting Ir), d -band centers shifted towards the Fermi level are found for M_{13} . This is an expected behavior for the particles, considering that the localization of the electronic states should increase as the system size decreases and becomes both less periodic and with less coordinated atoms [29, 30].

All the analyzed structures belong to the C_s point group, thus presenting a symmetry plane which reduces the number of non-equivalent sites on its surface. In this sense, each particle exhibits several possible interaction sites with small molecules like O_2 and N_2 , namely, 9 non-equivalent top sites, 14 non-equivalent bridges sites and 10 non-equivalent 3-atom hollow sites. Effective coordination numbers for each atom i (ECN^i) were computed for the Pt_{13} cluster according to eq. 11.3,

$$ECN^i = \sum_j \exp \left[1 - \left(\frac{d_{ij}}{d_{av}^i} \right)^4 \right] \quad (11.3)$$

where the sum runs over all neighboring atoms j which are at a distance d_{ij} from the atom i , and d_{av}^i is the average bond distance for the i atom, which was obtained by iteration using the expression of eq. 11.4 [31, 32].

$$d_{av}^i = \frac{\sum_j d_{ij} \exp \left[1 - \left(\frac{d_{ij}}{d_{av}^i} \right)^4 \right]}{\sum_j \exp \left[1 - \left(\frac{d_{ij}}{d_{av}^i} \right)^4 \right]} \quad (11.4)$$

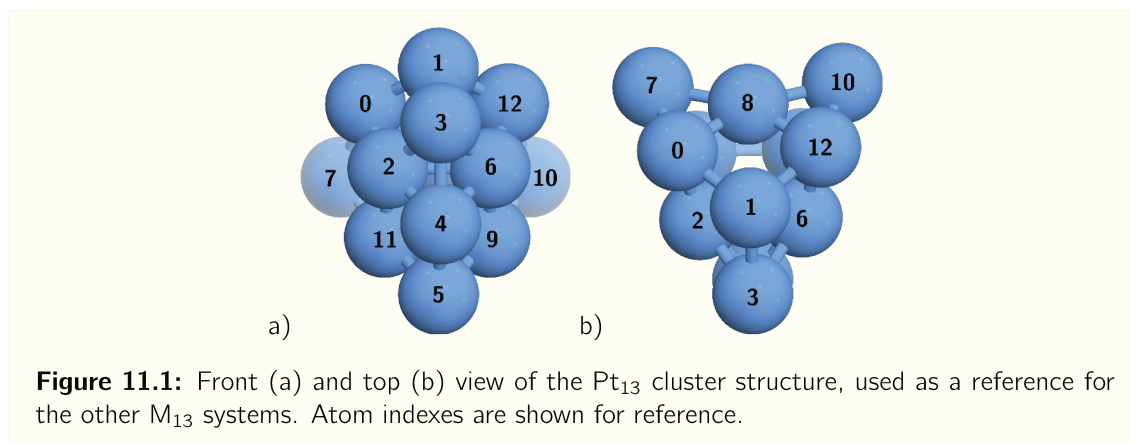
Mean ECN and d_{av} values for the total systems were also calculated according to eq. 11.5 and eq. 11.6, respectively.

$$d_{av} = \frac{1}{13} \sum_i d_{av}^i \quad (11.5)$$

$$ECN = \frac{1}{13} \sum_i ECN^i \quad (11.6)$$

The ECN^i values for non-equivalent atoms of Pt_{13} are listed in Table 11.2, where it can be noted that the most coordinated atoms are those with indexes 2 and 8, which are located at the center of the "facets" of the nanoparticle. In contrast, lower ECN^i values are found for the rest of the atoms due to their "edge" positions, with the least coordinated ones being those located at the "vertices" of the particles (indexed 3, 5, 7). As the other M_{13} clusters have an equivalent geometry, the description above is shared with the other systems as well.

It is interesting to note another aspect of the structural difference between the nanoparticles and their respective bulk systems. With the exception of Fe, all the investigated metals present, in their bulk form, close-packed structures (*fcc* for Ni, Cu, Rh, Pd, Ag, Ir, Pt and Au, and *hcp* for Co, Ru and Os) with each atom coordinating with 12 neighbors. For the excepted metal, even though it presents a non-close-packed bulk structure (*bcc*), a coordination number of 8 is found for each atom. Therefore, when compared to their respective bulk systems, all of the ECN^i values of the M_{13}



particles result considerably low, as expected due to their larger surface area and lower coordination of their atoms.

In contrast with the ECN values, the average bond distance changes for each metal cluster, as they present a more expanded or contracted configuration with respect to the Pt₁₃ system. The d_{av} values are listed in Table 11.1, and shown in Fig. 11.3. An increasing trend is observed for the average bond distance values when moving to the right in the periodic table inside each group of metals, in the same fashion as the cohesive energy, unveiling an increasing repulsion between the atoms which is most likely caused by the progressive filling of the d orbitals. Fig. 11.3 also presents, for comparison, the reported atomic metallic radius for each metal (r_{met}) [33]. It can be seen that the M₁₃ structures systematically present stronger bondings (i.e. shorter bond distances) when compared to their bulk states. As suggested by Chou et al. [26], this effect could be related to the lack of coordination in such small systems, as described above.

The following sections will explore the chemical behavior of the M₁₃ particles with respect to the O₂ and N₂ molecules. In this sense, their adsorption will be studied in order to quantitatively describe the reactivity on the surfaces of the metal clusters. This information would be of great interest for the analysis of periodic trends for small metal systems.

11.2.2 O₂ on M₁₃ nanoparticles

In order to study the O₂ adsorption on the metal nanoparticles, a first set of calculations was made to search the most stable site and mode of interaction between the oxygen molecule and the M₁₃ particle surfaces. The adsorption was initially considered in those geometries, which resemble the most frequently found ones in the literature [34–36]. As an example, the adsorption configurations for the Pt₁₃ nanoparticle are depicted in Fig. 11.5. Only the systems where the oxygen molecule has shown a chemisorbed state are presented. A similar criterion is applied to the nitrogen molecule on M₁₃.

The adsorption energies of the most stable systems corresponding to each adsorption mode (**e/tp**, **s/tp**, **e/hw**, **s/hw** and **br**) and M₁₃ cluster are shown in Fig. 11.6. These energies were calculated according to eq. 11.7,

$$E_{ads\ O_2} = E_{O_2/M_{13}} - E_{O_2} - E_{M_{13}} \quad (11.7)$$

Z	M	E_{coh}/eV	$d_{\text{av}}/\text{\AA}$	ϵ^d/eV
26	Fe	-2.89	2.399	-2.07
27	Co	-3.31	2.337	-1.99
28	Ni	-3.10	2.460	-1.54
29	Cu	-2.21	2.543	-2.22
44	Ru	-4.56	2.557	-2.36
45	Rh	-3.99	2.653	-2.14
46	Pd	-2.43	2.844	-1.74
47	Ag	-1.58	2.539	-3.96
76	Os	-5.33	2.524	-2.91
77	Ir	-4.98	2.562	-2.18
78	Pt	-3.99	2.642	-2.40
79	Au	-2.10	2.818	-3.05

Table 11.1: Atomic numbers (Z), element symbols (M), cohesive energies (E_{coh}), average bond distances (d_{av}) and d -band centers (ϵ^d) for each M_{13} metal cluster.

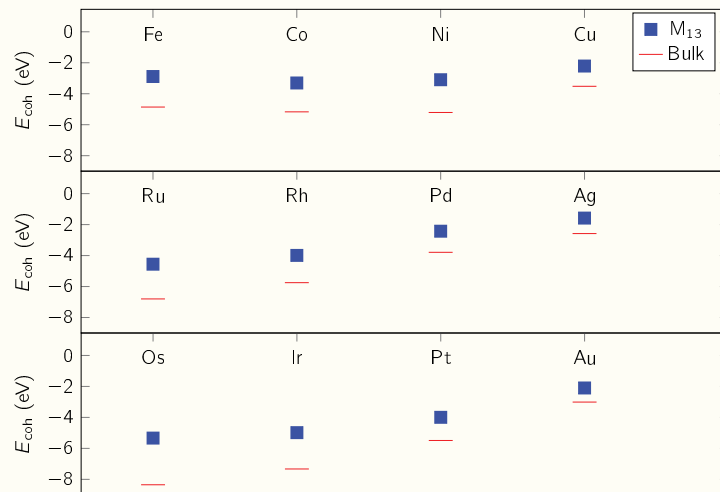


Figure 11.2: Cohesive energies (E_{coh}) of M_{13} clusters (blue) and bulk systems (red dash).

Atom	ECN ⁱ
0	4.36
1	5.18
2	7.02
3	4.03
4	4.24
5	3.44
7	3.13
8	7.28
11	4.35

Table 11.2: Effective coordination numbers for non-equivalent atoms of the Pt_{13} cluster. The atom indexes correspond to those shown in Fig. 11.1.

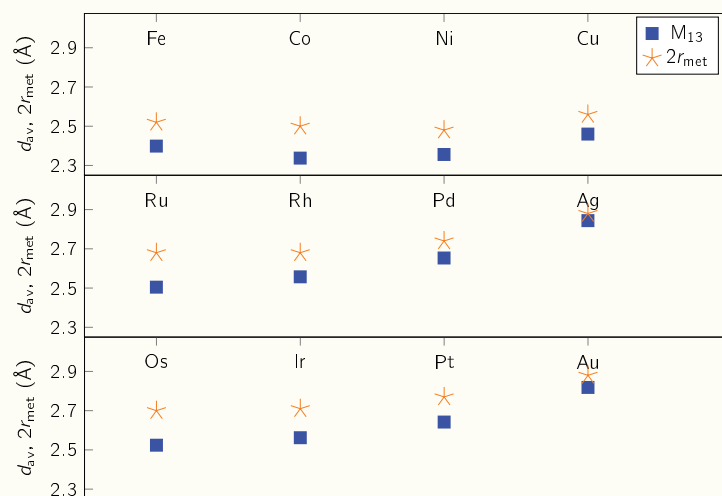


Figure 11.3: Average bond distance values (d_{av}) of the studied M_{13} nanoparticles. The reported metallic radius of each metal (r_{met}) is also shown, affected by a factor of 2.

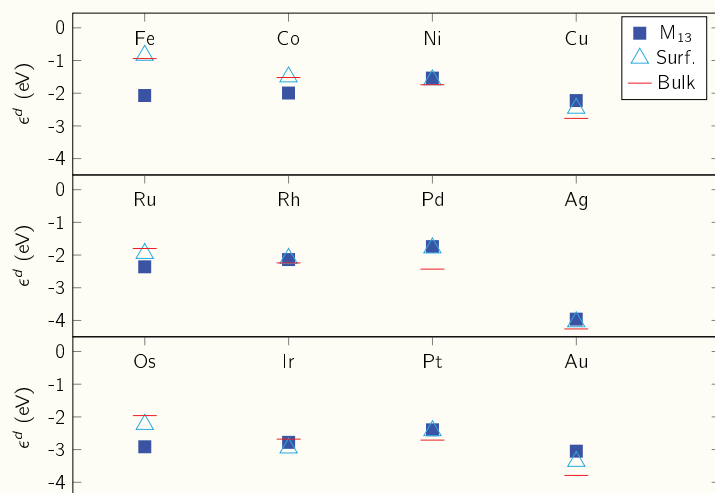


Figure 11.4: Total d -band centers (ϵ^d) corresponding to the investigated M_{13} nanoparticles (blue). Reported d -band centers values for surfaces (cyan triangles) and bulk (red dash) systems are also shown.

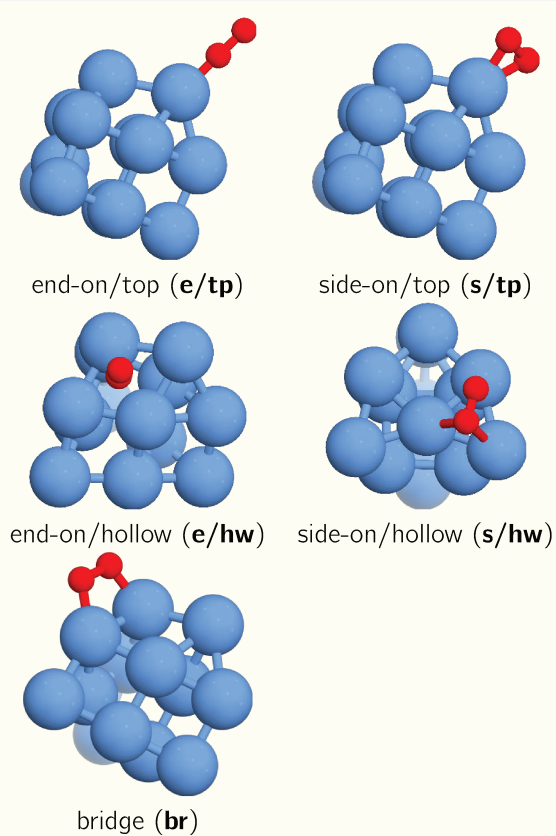


Figure 11.5: Examples of each of the adsorption configurations for $\text{O}_2/\text{Pt}_{13}$. Oxygen and platinum atoms are shown in red and blue colors, respectively.

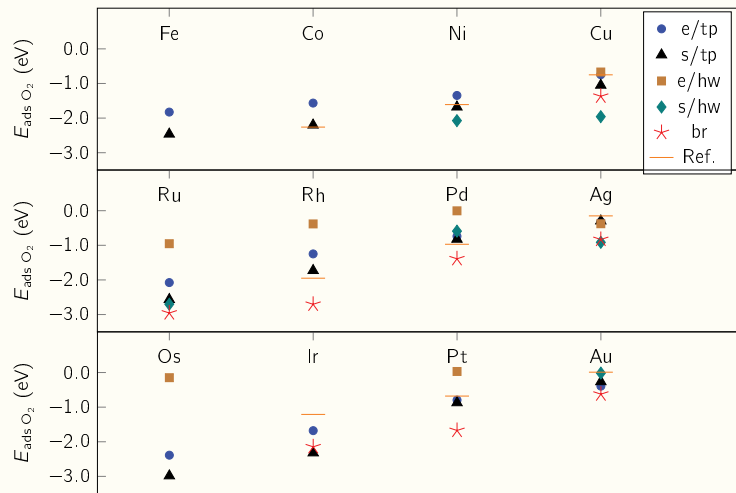


Figure 11.6: Oxygen adsorption on M_{13} energies of the most stable modes of adsorption for each metal cluster (M_{13}). Numeric values are also provided in Table A.1. Reference values (in orange dashes) were taken from Montemore et al. [34], and correspond to average DFT adsorption energies found in literature for O_2 on the *fcc*(111) and *hcp*(0001) surfaces.

where $E_{O_2/M_{13}}$, E_{O_2} and $E_{M_{13}}$ are the total electronic energies of the O_2/M_{13} , O_2 and M_{13} systems, respectively.

From a thermodynamic perspective, there is an increasing energy trend for O_2 adsorption in **e/tp** and **s/tp** modes with the latter exhibiting predominantly more negative values in nearly all cases. For Fe, Co, Ni, Ir and Au, in turn, no stable O_2 adsorptions on **e/hw** modes were found. This situation is repeated for Fe, Co, Ni and Os for **br** modes. In these systems, the initially proposed adsorbed configuration evolved to a physisorbed or a dissociated state during structural optimization. This behavior is different from what has been reported for metallic surfaces in Co, Ni, where "bridge" and "hollow" are preferred for O_2 adsorption [34]. It agrees, however, partially in the case of O_2 adsorption on Ir_{13} in the **br** configuration.

In addition, the stronger O_2 adsorption energies found in most of the M_{13} systems with respect to the reported values for metallic surfaces can be attributed to the lower coordination of the atoms in the nanoparticles. This is particularly interesting, especially for the "*coin-metals*", which are known for their weak reactivity towards O_2 .

The O_2 bond length for the adsorbed configurations are shown in Fig. 11.7. As it can be seen, the adsorption induces a notable elongation of the O–O bond in all cases with respect to the O_2 bond in gas phase (experimental value 1.208 Å [37], theoretical value in this work 1.233 Å). Independently of the metal type, a clear trend in the bond length can be established for each adsorption mode: **e/tp** < **e/hw** < **s/tp** < **br** \lesssim **s/hw**. The most elongated adsorbed states in **br** and **s/hw** can be explained by a geometric effect, considering that in these configurations the oxygen molecule has to adopt the distance between the metallic atoms in the surface of the particle. Oxygen molecule bond length also unveils the different oxidation states of its atoms. The least affected states are found in "end-on" cases, with bond distances between the molecular (O_2) and the superoxo (O_2^- , length: 1.35Å) states, followed by "side-on" and "bridge" systems, with bond lengths between the

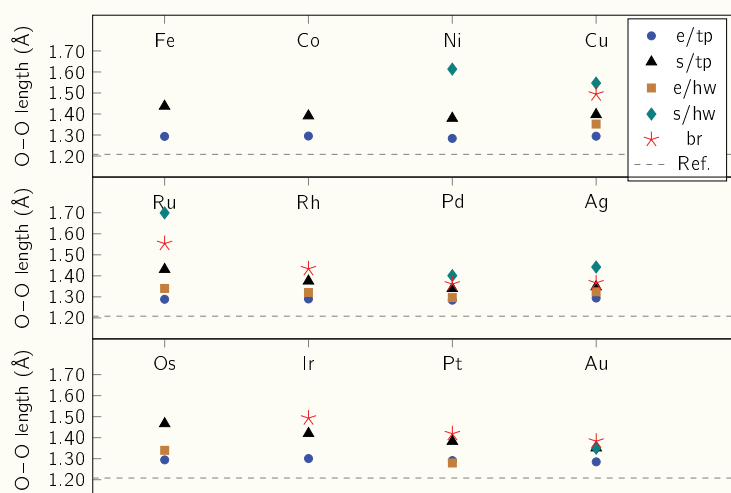


Figure 11.7: O₂ bond lengths of the most stable modes of adsorption on each metal cluster. Numeric values are given as well in Table A.1. Experimental bond length value for the oxygen molecule in gas phase is shown in dashed line as a reference.

superoxo and the peroxo (O₂⁻²) states. Length values were taken from ref. [34]. As expected, and in agreement with previous research [34], "side-on" adsorption on "bridge" and "hollow" sites show the most elongated (and therefore oxidized) O₂ states of each group, when present.

The minimum M–O₂ distances of the adsorbed configurations are depicted in Fig. 11.8. A consistent trend is evident for the oxygen–particle distance, regardless of the metal type: **e/tp** < **br** \lesssim **s/tp** \lesssim **s/hw** < **e/hw**. Taking as a reference the sum of the metallic and covalent radius for each species (M and O, respectively) (shown in orange-colored lines, Fig. 11.8) [33, 38], it can be observed that the last metals of each period promote oxygen adsorption at M–O₂ distances notably greater than the expected covalent radius, while the first metals usually present lower ones. The latter observation can be associated with the stronger adsorption energies found for the first metals.

It is also interesting to analyze the plots of the O₂ bond length and that of the M–O₂ distances as a function of the adsorption energy for each stable system, as shown in Fig. 11.9. For the O₂ bond length (Fig. 11.9, left side), a general trend is observed for each adsorption mode. While the O₂ bond lengths of **e/tp** sites present rather constant values, irrespective of the adsorption energy, the other sites (**s/tp**, **e/hw** and **br**) show an increasing bond distance with stronger adsorption energies. The latter trend is pronounced in **s/tp** and **e/hw** and **s/hw** modes, and more scattered for **br** configurations. As previously observed, the greater elongations of O₂ occur at bridge sites within the same range of adsorption energy as that obtained for the side-on and hollow sites.

Furthermore, metal–oxygen distances for adsorbed states (Fig. 11.9, right side) display a subtle overall pattern with respect to the adsorption energy, showing more negative energies for shorter M–O₂ distances, regardless of adsorption site and metal type. This behavior indicates a general stabilization of both, O₂ and M₁₃ systems when the interaction occurs at closer distances.

Fig. 11.10a) shows the amount of charge transferred from the M₁₃ particle to the adsorbed O₂ molecule for the most stable systems. In these models, O₂ charge relocalizations between $-0.5 |e|$ and $-0.1 |e|$ are found, meaning that a charge transfer from the metal particle to the oxygen molecule is

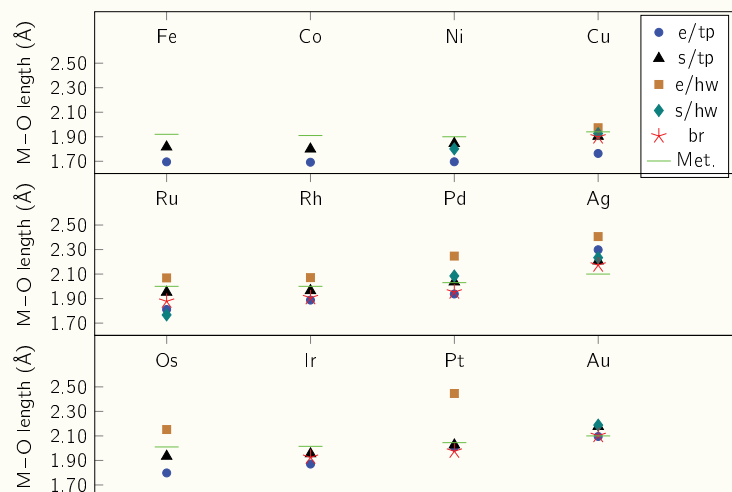
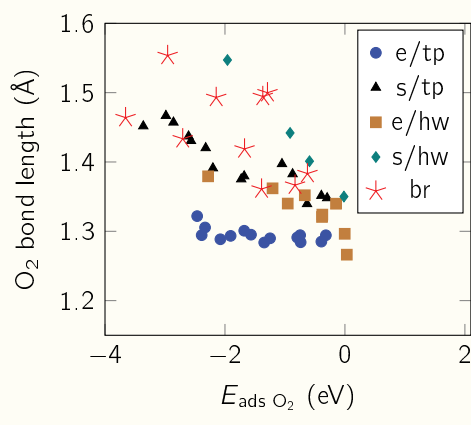
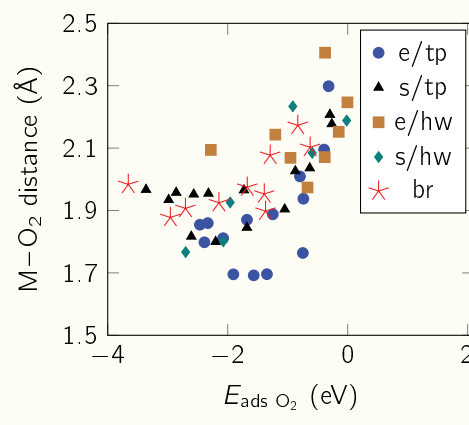


Figure 11.8: M–O₂ distances of the most stable modes of adsorption for each metal cluster, plotted as a function of the atomic number. The sums of the metallic and covalent radius for each species (M and O, respectively) are shown in green-colored dashes as a reference.



a)



b)

Figure 11.9: O₂ bond (a) and M–O₂ (b) distances of the most stable modes of adsorption for each metal cluster, plotted as a function of the adsorption energy.

found in every case. As a rule, "end-on" adsorptions (**e/tp**, **e/hw**) present the least charge transfers, while "side-on" and "bridge" modes show the greatest ones. This observation is somehow expected, as there is a single O–M interaction in the first group, and two in the second one. In addition, the Pauling's electronegativity values for each metal [39] also follow closely the charge transfer trends as observed in Fig. 11.10a). In Fig. 11.10b), in turn, the net atomic charge differences between O¹ and O² atoms (the superscripts distinguish the two atoms in the oxygen molecule, where O¹ is the closest one to the metallic particle) is shown for each adsorbed mode. Again, "end-on" adsorptions show a contrasting behavior. In these modes a larger atomic charge accumulation, up to $-0.25 |e|$, is found for the outermost O atoms. This charge polarization, which is to be expected in "end-on" adsorptions, decreases considerably with the atomic number. On the other hand, none or little polarization is observed in the more symmetric adsorption modes ("side-on" and "bridge").

Another interesting parameters obtained from the atomic population analysis are the O–O and M–O overlap populations, as well as the oxygen bond orders in the O₂ molecule. These can give an insight into the strength of the newly formed O₂–M₁₃ and the existing O₂ chemical bonds in the adsorbed systems. From Fig. 11.11, it can be observed that there is a reduction in the O–O overlap in all studied cases with respect to the O₂ in gas phase. Moreover, O–O bond strength in the **s/hw**, **br** and **s/tp** adsorption modes are considerably weaker than in "end-on" adsorptions. This observation encompasses the O₂ charge results described above, suggesting that a larger charge transfer to the oxygen molecule induces a greater loss in the O–O strength.

The sum of M₁₃–O¹ and M₁₃–O² overlaps, presented in Fig. 11.12, helps characterizing the strength of the O₂–M₁₃ interaction. From these results, an opposite effect with respect to O–O overlap is observed for each metal and adsorption site, meaning that a stronger M–O overlapping can be associated with a weaker O–O interaction. In other words, the metal nanoparticle destabilizes the O–O bond by forming stronger M–O bonds. The metal–oxygen overlap also shows a slight decreasing trend with the atomic number within each group in the periodic table.

The atoms in the O₂ also suffer a variation in their bond orders when adsorbing to the M₁₃ particle. The bond order value computed for gas-phase O₂ atoms (1.8, shown in black dashed line as a reference) is conserved in systems comprising "side-on" and "bridge" adsorption modes for both O¹ and O² atoms. This can be related to the formation of new M–O bonds, which is given in a more or less symmetric fashion for the two atoms of the oxygen molecule. In this sense, both M–O and O–O are suggested to be a single-bond each. Differences arise for the "end-on" adsorption modes in this regard, in concordance with O–O and M–O overlap population analysis. In these adsorption states, the outermost oxygen atoms (O², see Fig. 11.13b)) show a small decrease in their bond order (1.5 – 1.6, approximately) with respect to the gas-phase molecule, while the O atoms directly interacting with the metal particle (O¹, see Fig. 11.13a)) increase their bond orders to values comprised between 2.2 and 2.9. For these O¹ atoms, in addition, the bond orders are observed to decrease with the increasing atomic number of the metal. The higher bond order values of O¹ in "end-on" adsorptions can be related to their relatively larger M–O overlaps, as described above, and therefore to stronger O₂–M₁₃ bonds. These effects are originated from the asymmetric location of the oxygen atoms in comparison with "side-on" and "bridge" modes.

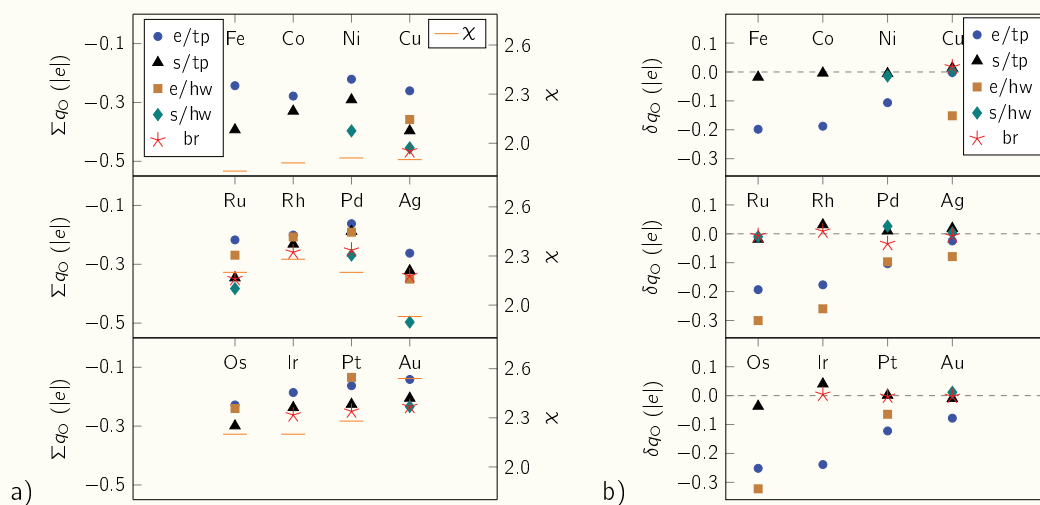


Figure 11.10: a) Sum of the net atomic charges (DDEC6 method) in the O_2 molecule (Σq_O) for the most stable modes of adsorption for each metal. Pauling's electronegativity (χ) values of each metal are also shown as a reference. b) Difference of O^2 and O^1 net atomic charge values (δq_O) of the most stable modes of adsorption for each metal. The O^1 atom is the closest one to the metal particle.

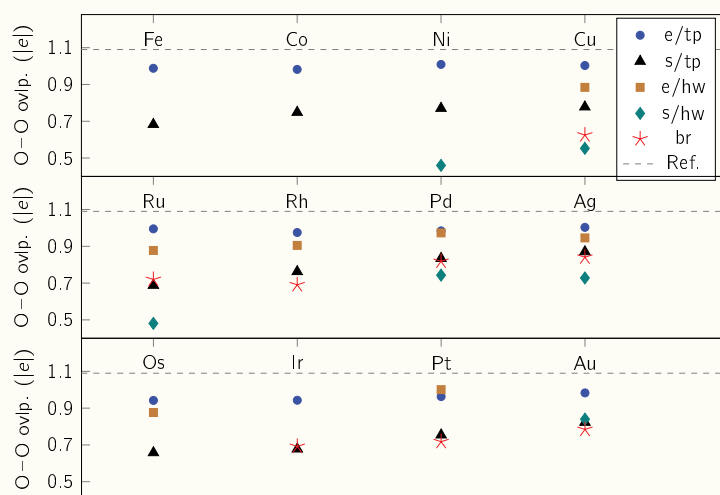


Figure 11.11: O–O overlap (DDEC6 method) of the most stable modes of adsorption for each metal. O–O overlap of the isolated O_2 molecule is shown as well in dashed line as a reference.

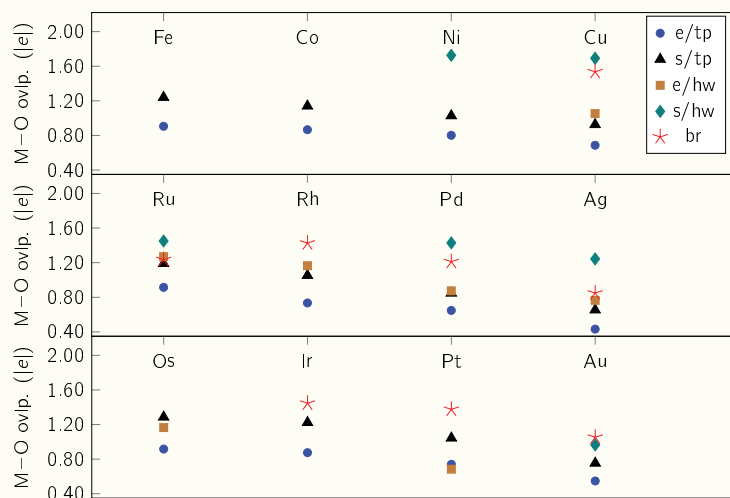


Figure 11.12: Sum of M–O overlaps (DDEC6 method) of the most stable modes of adsorption for each metal.

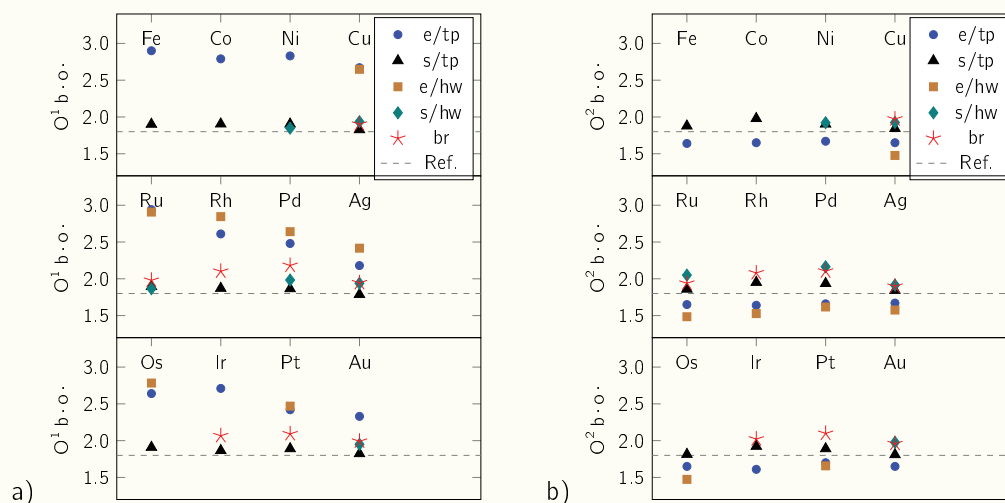


Figure 11.13: O^1 (a) and O^2 (b) bond orders (DDEC6 method) of the most stable modes of adsorption for each metal. The computed bond order of oxygen atoms in gas-phase O_2 is shown in black dashed line as a reference.

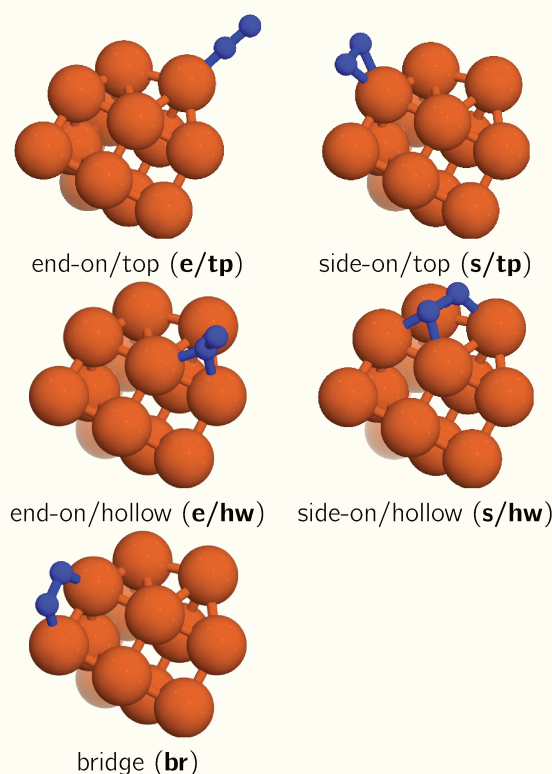


Figure 11.14: Examples of each of the adsorption configurations for $\text{N}_2/\text{Fe}_{13}$. Nitrogen and iron atoms are shown in red and orange colors, respectively.

11.2.3 N_2 on M_{13} nanoparticles

The study of N_2 adsorption on the metal nanoparticles follows the same methodology as that used for the O_2 molecule. Therefore, similar geometries were considered, namely **e/tp**, **s/tp**, **e/hw**, **s/hw**, **br**. As an example, adsorption geometries are illustrated for the Fe_{13} particle (Fig. 11.14). The results pertaining solely to chemisorption processes will be described below.

The adsorption energies of the most stable systems corresponding to each adsorption mode (**e/tp**, **s/tp**, **e/hw**, **s/hw** and **br**) and M_{13} particles are shown in Fig. 11.15. The corresponding energies were calculated by eq. 11.8 as follows:

$$E_{\text{ads N}_2} = E_{\text{N}_2/\text{M}_{13}} - E_{\text{N}_2} - E_{\text{M}_{13}} \quad (11.8)$$

where $E_{\text{N}_2/\text{M}_{13}}$, $E_{\text{M}_{13}}$ and E_{N_2} are the total electronic energies of the N_2/M_{13} , M_{13} and N_2 systems, respectively.

According to the results shown in Fig. 11.15, tendencies are observed for each group, although no clear trend can be detected in comparison with O_2 adsorption. In general terms, **e/tp** and **br** configurations present similar adsorption energies, irrespective of the metal type, with more negative values compared to **e/hw**, **s/hw** and **s/tp** modes. In addition, the N_2 adsorption is found to be weaker as the atomic number increases within each metal group.

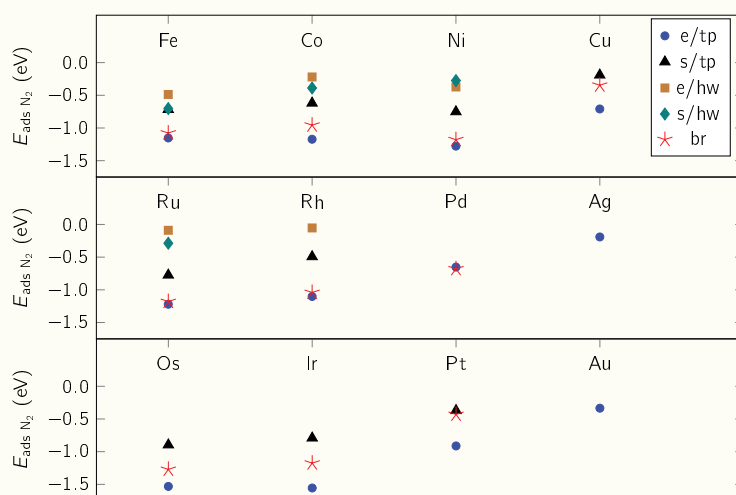


Figure 11.15: Nitrogen adsorption on M_{13} energies of the most stable modes of adsorption for each metal cluster (M_{13}). Numeric values are also provided in Table A.2.

The N_2 bond length for the adsorbed configurations are depicted in Fig. 11.16. Similar to the O_2 adsorption, there is a notable elongation of the N–N bond in all adsorbed systems compared to N_2 in gas phase (experimental: 1.098 Å [40] ; theoretical, this work: 1.118 Å). Results show a clear periodic trend in the elongation length for each adsorption mode, irrespective of the metal nature of the particle: $\mathbf{e/tp} \lesssim \mathbf{e/hw} \lesssim \mathbf{s/tp} < \mathbf{br} < \mathbf{s/hw}$. These findings indicate that the geometric effect described in the case of O_2 adsorption in **br** and **s/hw** configurations is observed as well for N_2 .

The minimum M– N_2 distances of the adsorbed configurations are shown in Fig. 11.17. As previously, a trend is observed concerning the different adsorption modes, and regardless of the metal nature: $\mathbf{e/tp} < \mathbf{s/hw} \lesssim \mathbf{br} < \mathbf{s/tp} < \mathbf{e/hw}$. Taking as a reference the sum of the covalent and metallic radius of N and M species, respectively, it can be seen that the adsorbed systems usually display M– N_2 interactions at distances that are lower than the reference.

Similarly to the study on O_2 , the relationship between the N_2 bond and M– N_2 distances as a function of the adsorption energy for each stable system is depicted in Fig. 11.18. Regarding the N_2 bond length (Fig. 11.18, left side), a pattern is observed for each adsorption mode, except for **s/hw**. The **s/tp** and **br** modes exhibit a comparable correlation between N–N lengths and adsorption energies, although the latter displays a broader energy span. The correlations of both adsorption modes are stronger than the observed for end-on modes (**e/tp** and **e/hw**), which show rather constant values of N–N lengths for different adsorption energy values. However, while the points associated with **s/hw** configurations are more dispersed, they also exhibit larger N_2 bond lengths compared to the previous systems, and they fall within a more positive and compact range of adsorption energies. On the other hand, as can be seen in Fig. 11.18a, no correlation was detected between the adsorption energy with the metal–nitrogen distances.

DDEC6 atomic population analysis results are presented for N_2/M_{13} systems as well. Fig. 11.19a) presents the total charge of N_2 after adsorption. An increasing trend is clearly observed in this case regardless of the metal type and adsorption mode which, in contrast with O_2 , ends up with nearly-zero or positive values for the last metals of each group. An inter-site relationship can also

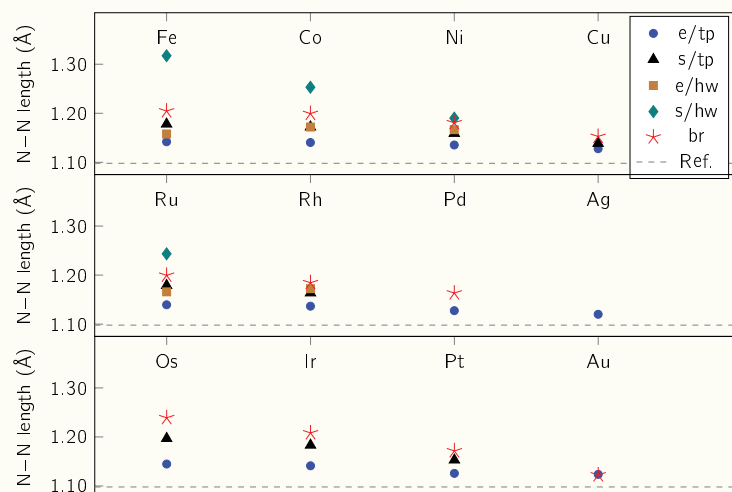


Figure 11.16: O₂ bond lengths of the most stable modes of adsorption on each metal cluster. Numeric values are given as well in Table A.2. Experimental bond length value for the nitrogen molecule in gas phase is shown in dashed line as a reference.

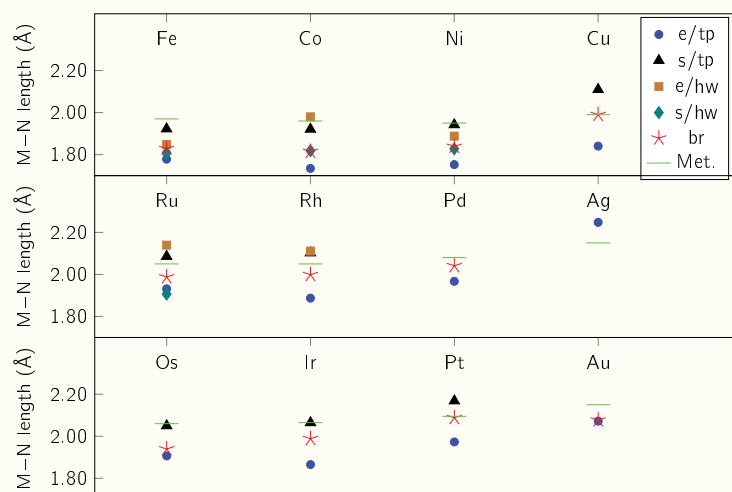
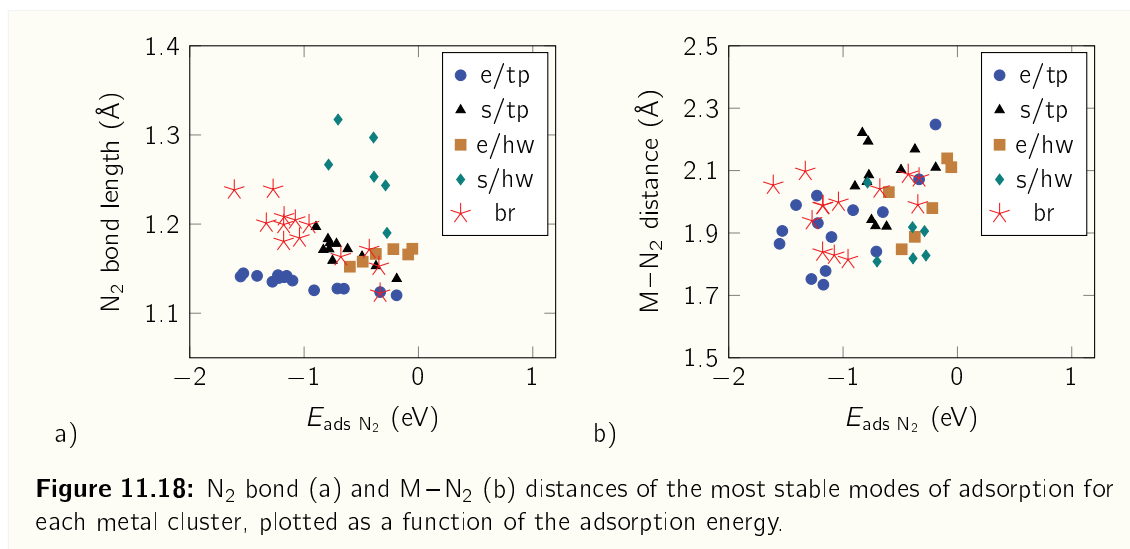


Figure 11.17: M-N₂ distances of the most stable modes of adsorption for each metal cluster, plotted as a function of the atomic number. The sums of the metallic and covalent radius for each species (M and N, respectively) are shown in green-colored lines as a reference.



be easily established regarding total charge transfer values: $s/hw < br < s/tp < e/hw \lesssim e/tp$. Differently from O_2/M_{13} , the electronegativity of each metal does not follow the same trend as the total charge transfer values shown in Fig. 11.19a). On the other hand, the charge difference between N^2 and N^1 atoms (the superscripts have the same meaning as in the case of O_2), shown in Fig. 11.19b), unveils a polarization of the N_2 adsorbed molecule in "end-on" systems, which decreases from left to right in the periodic table.

The $N-N$ overlap population (Fig. 11.20) presents larger values as the atomic number increases within each group of metals. These values suffer a variation with the adsorption mode as well, which are given in the same order as the one described above for charge transfer. Conversely, $M-N$ overlaps (Fig. 11.21) decrease showing an inverse order with respect to both the atomic number and the adsorption site with respect to the $N-N$ overlaps. Therefore, as in the case of O_2 , a stronger $M-N$ overlap involves a weaker $N-N$ interaction.

With respect to N atoms bond orders (Fig. 11.22), a behavior similar to the O_2 adsorption case is observed. The adsorption of N_2 on "side-on" and "bridge" modes induces a slight increase of the nitrogen atoms bond orders (from 2.8, computed for gas-phase N_2 , to approximately 3.0) for both N^1 and N^2 atoms. In turn, in "end-on" adsorption modes a split is observed in bond order values: approximately 2.6 for the outermost N atom (N^2), and 3.3 – 4.0 for the N^1 atom. In the latter, a range of values is observed due to the asymmetry of the "end-on" adsorption modes.

From these results, it can be observed that a larger charge transfer from the metal particle to the adsorbed N_2 molecule is accompanied by an elongation of the $N-N$ bond length, a stronger $M-N$ overlap and a weakening of the $N-N$ interaction.

11.2.4 Discussion

Based on literature data, it is known that transition metal nanoparticles are appropriate as catalysts for the adsorption or dissociation of different molecules such as CO , NO , N_2 , O_2 , and H_2 [20, 41–45]. Transition metal surfaces [46–48], or transition metals supported on graphene [49–51], or germanene [52], or on surfaces [13, 53], or as sites within organic molecules [54, 55] were evaluated as well, with

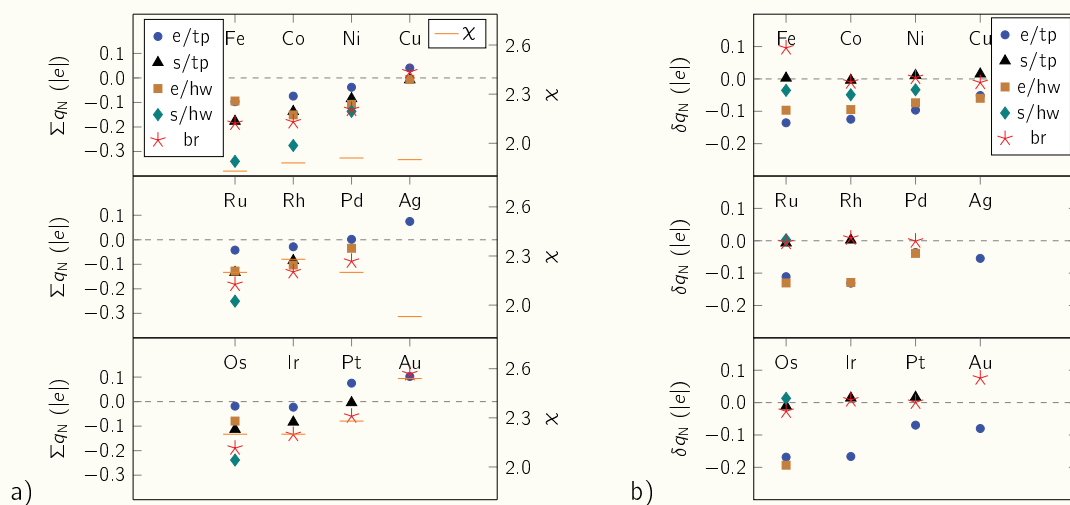


Figure 11.19: a) Sum of the net atomic charges (DDEC6 method) in the N_2 molecule (Σq_N) for the most stable modes of adsorption for each metal. Pauling's electronegativity (χ) values of each metal are also shown as a reference. b) Difference of N^2 and N^1 net atomic charge values (δq_N) of the most stable modes of adsorption for each metal. The O^1 atom is the closest one to the metal particle.

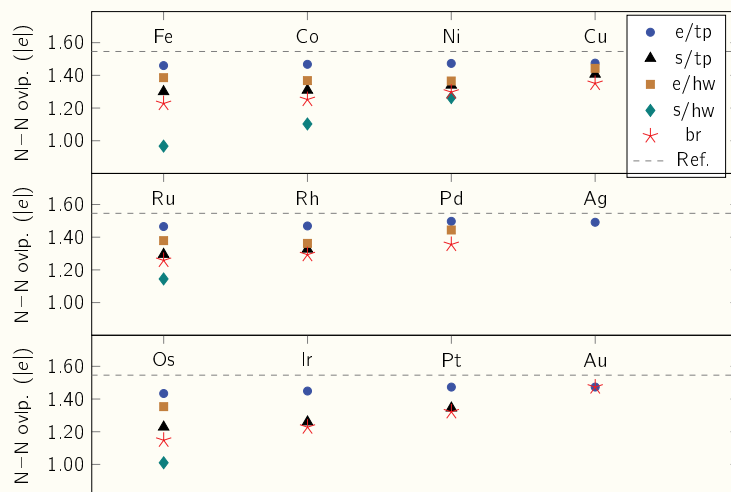


Figure 11.20: N–N overlap (DDEC6 method) of the most stable modes of adsorption for each metal. N–N overlap of the isolated N_2 molecule is shown as well in dashed line as a reference.

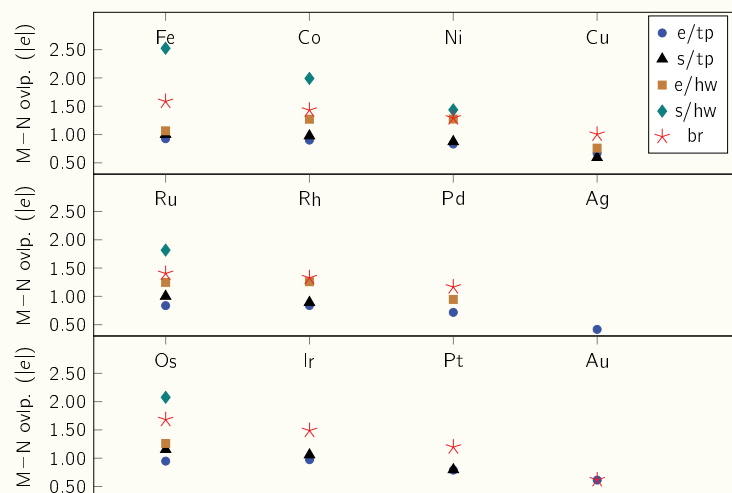


Figure 11.21: Sum of M–N overlaps (DDEC6 method) of the most stable modes of adsorption for each metal.

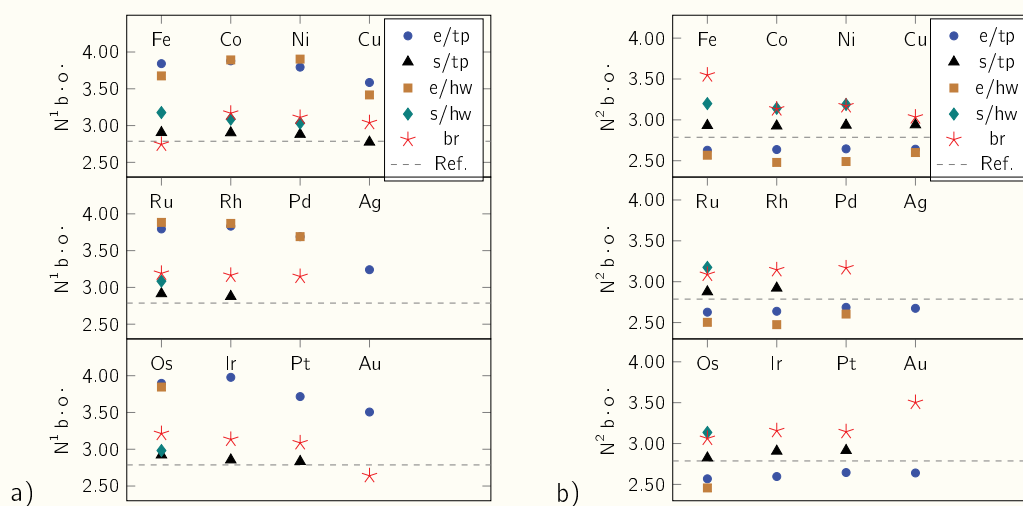


Figure 11.22: N^1 (a) and N^2 (b) bond orders (DDEC6 method) of the most stable modes of adsorption for each metal. The computed bond order of oxygen atoms in gas-phase N_2 is shown in black dashed line as a reference.

encouraging results. For this reason, a more systematic approach was employed to investigate the behavior of these nanoparticles, with the objective of identifying periodic trends. Particularly, 13-atom nanoparticles were selected since in previous studies they were shown to be more effective than surfaces, with even greater effectiveness in low coordination sites [25, 36, 41, 43, 44, 56–59].

To understand the nanoparticle reactivity, strain and chemical factors have been evaluated, which affect the catalytic properties of the clusters as well as different processes. For years, several studies have focused on the *d*-band center as a reactivity descriptor [60]. The success of the *d*-band model is based on the well-established dependency of the binding energy of an adsorbate to a metal surface on the electronic structure of the surface itself. In spite of its favorable outcome, some discrepancies have been found [10, 11, 61]. In most of the cases the lack of correlation can be explained by an insufficient description of the electronic structure of the substrate, e.g. the density of states of the *d*-band at the Fermi level, the contribution of the *sp*-band, or the repulsive interaction between states of the adsorbate and the surface. The *d*-band center for each nanoparticle and the adsorption energies for both molecules (O₂ and N₂) are shown in Fig 11.23. At first glance, no direct trend is found for the different adsorption sites with the *d*-band center, which corroborates the need for a more in-depth study of each system.

In this context, the *d*-band states were qualitatively analyzed to elucidate a "tentative" trend in the reactivity of the studied particles (Fig 11.24).

It is well known that one of the requirements for a material to be a good catalyst generally involves *d*-bands with energies close to the Fermi level. The projected density of states is explained in terms of the position of the *d*-bands, therefore, from Fig 11.24, the following metal particles are expected to be a potential good catalyst: Ru, Rh, Pd, Os, Ir and Pt. Mainly these metals have a *d*-band, which is narrower, has more structure and whose position passes the Fermi level. The other metals present difficulties such as important magnetization effects, among others, which require further studies (Fig. 11.24). Obviously, to have a complete scenario, the mere presence of a *d*-band is not enough to ensure good catalytic properties. In this context, the adsorption of O₂ and N₂ has been considered, as part of a reaction path for the molecule dissociation. The non-dissociative adsorption can be considered as the first step for the dissociation mechanism, while the molecule bond breaking is the second step and it is investigated separately in another study. Taking into account Sabatier's principle, for a good catalyst the adsorption energy of intermediates should be close to equilibrium. The thermodynamic analysis of the average adsorption energies of O₂ and N₂, obtained from eq. 11.9,

$$\bar{E}_{\text{ads}} = \frac{\sum_k E_{\text{ads}}^k}{\sum_k k} \quad (11.9)$$

(where *k* refers to each stable adsorption mode) for the metal clusters (Fig. 11.25) conclude that promising nanoparticles for the dissociation of oxygen and nitrogen are the following (adsorption energies and *d*-band centers are respectively given in parenthesis, both expressed in eV): for O₂: Pd (−0.67/−1.76), Pt (−0.80/−2.40), and for N₂: Pd (−0.39/−1.76), Pt (−0.57/−2.40), Os (−0.58/−2.90). A correction between +0.2 eV and +0.6 eV is estimated to obtain free energies of Gibbs for the different metals studied. It should be noted that for the coin metals (Cu, Ag, Au), since their *d*-band lies below the Fermi level, the interaction has no catalytic consequences. The effect is mostly caused by the interaction with the *sp*-band.

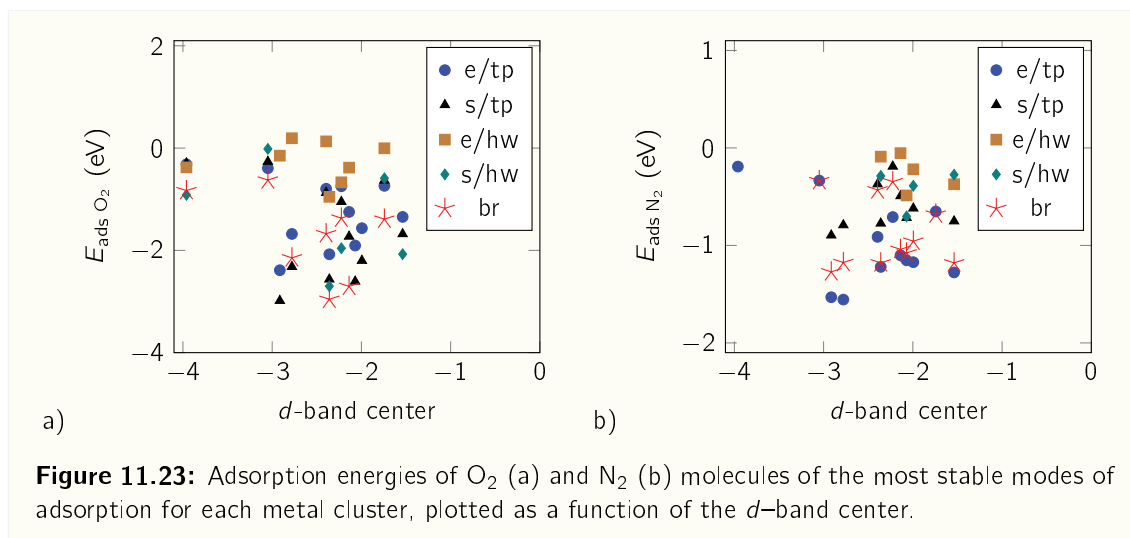


Figure 11.23: Adsorption energies of O₂ (a) and N₂ (b) molecules of the most stable modes of adsorption for each metal cluster, plotted as a function of the *d*-band center.

Finally, as seen in Figs. 11.6 and 11.15, the adsorption of both O₂ and N₂ molecules on M₁₃ particles is predicted to be energetically feasible. At this point of the discussion, it is worth recalling that within each transition metal series (namely 3*d*, 4*d* and 5*d*), it is expected that the stability of the adsorbed states will decrease with the increasing atomic number, for the considered metal elements, which is in accordance with the available literature on metallic surfaces that indicates the ability of transition metals to dissociate simple molecules (N₂, O₂, NO, CO, etc.) decreases across the transition series [62, 63]. In the case of monometallic clusters, several papers focused on the adsorption of NO indicate some similarities [17–19]. In this new investigation, the results seem to be coherent with previous results obtained on the adsorption of NO.

Additionally, in general terms the adsorption states of the oxygen molecule show an increased stability with respect to the nitrogen molecule, considering that the adsorption energies for O₂ are more negative than the values observed for N₂. This difference, computed as described by eq. 11.10,

$$\Delta E_{\text{ads}} = E_{\text{ads N}_2} - E_{\text{ads O}_2} \quad (11.10)$$

decreases with the increase of the atomic number within each period. This behavior can be observed in Fig. 11.26, which shows the difference between the corresponding minimum adsorption energies (i.e. considering all adsorption modes) of N₂ and O₂ for each metal. In this context, the adsorption of O₂ on the nanoparticles could be up to 2.3 eV more stable than the adsorption of the N₂ molecule, with the most notable differences found for the first elements considered on each period, which may be important in terms of molecule selectivity. Similar studies were carried out on different transition metals, observing, for example, the selectivity of Au₁₃ nanoparticles towards the adsorption of O₂ in relation to the adsorption of CO [64], or the selectivity of Au surfaces towards the adsorption of O₂ in relation to H₂ [65].

Both oxygen and nitrogen molecules show the shortest molecular bond lengths when adsorbed in **e/tp** configurations, regardless of the metal type. In all cases, an increase in the bond distance, compared to the experimental value, is observed, being more noteworthy for O₂ (~ 7.6%) than for N₂ (~ 3.8%). Maximum molecular bond lengths are also present for both molecules when adsorbed

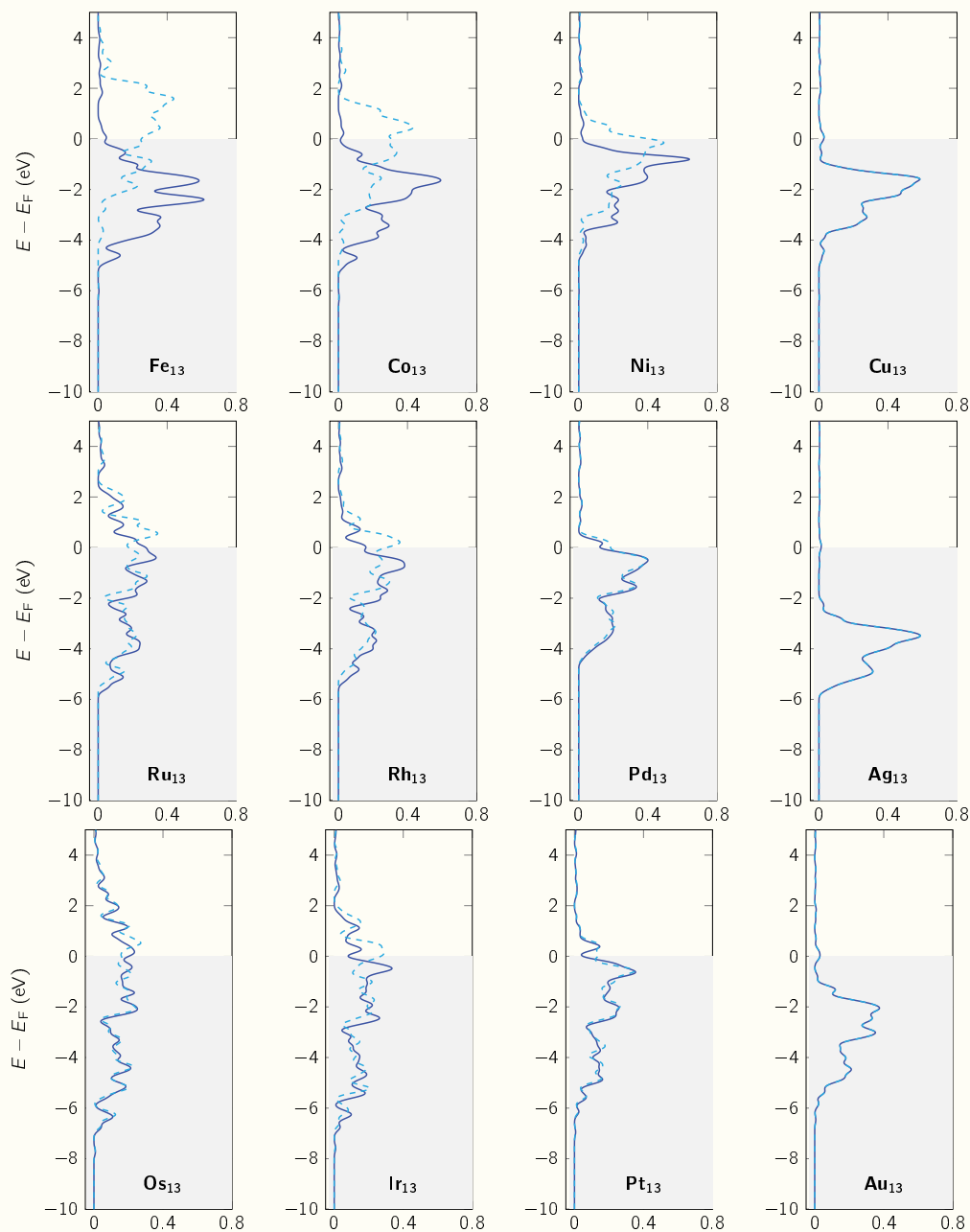


Figure 11.24: Projected density of states for d orbitals of the studied nanoparticles. Spin up (blue line) and down (cyan, dashed line). E_F represents the Fermi energy.

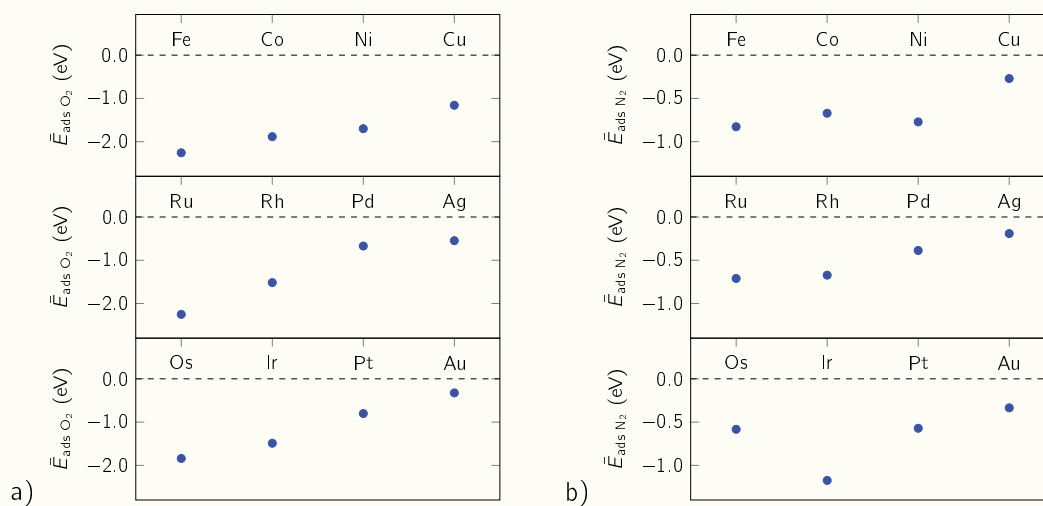


Figure 11.25: Averaged adsorption energies (\bar{E}_{ads}) for both molecules, O₂ (a) and N₂ (b).

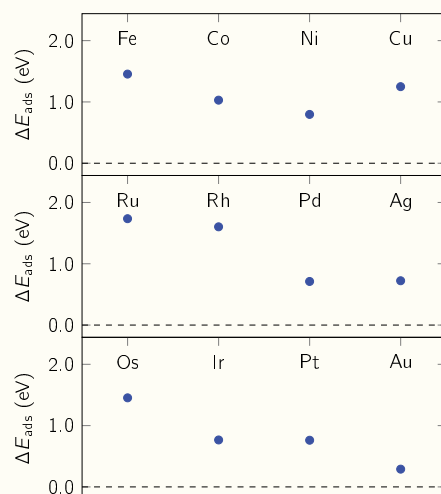


Figure 11.26: Difference of N₂ and O₂ adsorption energies (ΔE_{ads}).

in **br** or **s/hw** modes, with their values depending on the metal of the particle. These values show an increase, as well, with respect to the experimental bond length in gas phase (16% to 24% for O–O, and 2% to 18% for N–N). The larger increase of the O₂ bond with respect to the N₂ molecule suggests that the first is more effectively activated when adsorbed on the metal nanoparticles. In addition, minimum and maximum molecule–particle distances are given similarly for O₂ and N₂. In both cases, the minimum distances are found on **e/tp** configurations, with distances values between 1.7 Å and 2.1 Å. On the other hand, the maximum distances are observed for **br** and **e/hw** modes, taking values between 1.8 Å and 2.4 Å. These results are accompanied by an increasing ("end-on") or decreasing ("side-on" and "bridges") in the overlap populations of the atoms in the adsorbed molecule. Simultaneously, an opposite effect is observed in the overlap between the metal particle and the molecule.

As seen in Figs. 11.9b and 11.18b, clear correlations between the adsorption energies and the molecular bond lengths are observed for **s/tp** and **br** modes of adsorption, for both O₂ and N₂ cases, as well as rather constant bond lengths values for **e/tp** configurations. For **e/hw** modes, however, a differential behavior is shown, with correlated values for O₂, and constant lengths for N₂. The **br** and **s/hw** adsorption modes, on the other hand, present the highest molecular bond lengths for both nitrogen and oxygen adsorbed systems.

With respect to adsorption energies and molecule–particle distances, only a weak overall trend is observed for O₂, exposing an overall stabilization of both O₂ and M₁₃ systems when interacting at shorter distances (see Fig. 11.9b).

11.3 Summary

This chapter investigates the reactivity of transition metal clusters for the adsorption of O₂ and N₂ molecules using DFT. It is found that the stability of the adsorbed states decreases with the increasing atomic number of the considered metal elements, in line with the available literature. The adsorption energies for O₂ are generally more negative than those for N₂, with the difference decreasing with the increasing atomic number within each period. The study also identifies potential catalysts for the dissociation of oxygen and nitrogen, such as Pd, Pt, and Os for O₂, and Os for N₂. Nevertheless, Ru and Rh are also found to be high potential nanocluster metal catalysts. Additionally, the study highlights the correlation between the adsorption energies and the molecular bond lengths, providing valuable insights into the reactivity of metal clusters for O₂ and N₂ adsorption. Overall, the findings suggest that the adsorption of O₂ on the nanoparticles could be up to 2.3 eV more stable than the adsorption of the N₂ molecule, with important differences found for the first elements considered in each period, which may be important in terms of molecule selectivity. Thus, this work clarifies how the reaction behavior of the adsorbing molecules depends on the position of the metal element in the Periodic Table. This understanding is based on the *d*-band energy and the shape of the HOMO (band top), which are determined by the type of valence orbital (4*d* or 5*s* orbital).

Furthermore, the next planned stage of this investigation will involve examining the adsorptive dissociation of O₂ and N₂ molecules on selected sites of the M₁₃ metallic nanoparticles. Additionally, Ab-Initio Molecular Dynamics (AIMD) is expected to provide information about the melting points of such metallic nanoparticles which, together with the activation energies of O₂ and N₂ dissociation

studies, would provide valuable insight into related experimental observations of metallic nanoparticle catalysts, as outlined in the research line of Profs. Tielens and Bazin [14, 45].

References for Chapter 11

- [1] S. Chee, T. Lunkenbein, R. Schlögl, and B. Cuenya, "Operando electron microscopy of catalysts: The missing cornerstone in heterogeneous catalysis research?" *Chemical Reviews*, vol. 123, 23, p. 13 374, 2023.
- [2] F. Lin, M. Li, L. Zeng, M. Luo, and S. Guo, "Intermetallic nanocrystals for fuel-cells-based electrocatalysis," *Chemical Reviews*, vol. 123, 22, p. 12 507, 2023.
- [3] B. Ran *et al.*, "Photocatalytic antimicrobials: Principles, design strategies and applications," *Chemical Reviews*, vol. 123, 22, p. 12 371, 2023.
- [4] K. Rommens and M. Saeys, "Molecular views on Fischer–Tropsch synthesis," *Chemical Reviews*, vol. 123, 9, p. 5798, 2023.
- [5] L. Liu and C. A., "Metal catalysts for heterogeneous catalysis: From single atoms to nanoclusters and nanoparticles," *Chemical Review*, vol. 118, 10, p. 4981, 2018.
- [6] F. Garin, "Environmental catalysis," *Catalysis Today*, vol. 89, 3, p. 255, 2004.
- [7] Z. Liu and S. Woo, "Recent advances in catalytic DeNOX science and technology," *Catalysis Reviews*, vol. 48, 1, p. 43, 2006.
- [8] Y. Nanba and M. Koyama, "NO adsorption on 4d and 5d transition-metal (Rh, Pd, Ag, Ir, and Pt) nanoparticles: Density functional theory study and supervised learning," *Journal of Physical Chemistry C*, vol. 123, 46, p. 28 114, 2019.
- [9] M. J. Piotrowski, P. Piquini, Z. Zeng, and J. L. F. Da Silva, "Adsorption of NO on the Rh₁₃, Pd₁₃, Pd₁₃, Ir₁₃, and Pt₁₃ clusters: A density functional theory investigation," *Journal of Physical Chemistry C*, vol. 116, 38, p. 20 540, 2012.
- [10] H. Xin and S. Linic, "Communications: Exceptions to the d-band model of chemisorption on metal surfaces: The dominant role of repulsion between adsorbate states and metal d-states," *Journal of Chemical Physics*, vol. 32, p. 221 101, 2010.
- [11] M. Gorzkowski and A. Lewera, "Probing the limits of d-band center theory: Electronic and electrocatalytic properties of Pd-shell–Pt-core nanoparticles," *Journal of Physical Chemistry C*, vol. 119, 32, p. 18 389, 2015.
- [12] M. Boudart, "Model catalysts: Reductionism for understanding," *Topics in Catalysis*, vol. 13, p. 147, 2000.
- [13] F. Tielens and D. Bazin, "Operando characterization and DFT modelling of nanospinels: Some examples showing the relationship with catalytic activity," *Applied Catalysis A: General*, vol. 504, p. 631, 2015.

- [14] D. Bazin *et al.*, "Nanostructured materials and heterogeneous catalysis: A succinct review regarding DeNox catalysis," *Comptes Rendus. Chimie*, vol. 25, 3, p. 237, 2022.
- [15] Z. Zhang, A. B. Zandkarimi, and A. Alexandrova, "Ensembles of metastable states govern heterogeneous catalysis on dynamic interfaces," *Accounts of Chemical Research*, vol. 53, 2, p. 447, 2020.
- [16] K. Reuter and M. Scheffler, "First-principles atomistic thermodynamics for oxidation catalysis: Surface phase diagrams and catalytically interesting regions," *Physical Review Letters*, vol. 90, 4, p. 046 103, 2003.
- [17] I. Ouz, H. Guesmi, D. Bazin, and F. Tielens, "Predicting the activity of nano-transition-metal denox catalysts," *Journal of Physical Chemistry C*, vol. 123, p. 20 314, 2019.
- [18] N. Takagi, K. Ishimura, R. Fukuda, M. Ehara, and S. Sakaki, "Reaction behavior of the NO molecule on the surface of an M_n particle ($M = \text{Ru, Rh, Pd, and Ag}$; $n = 13$ and 55): Theoretical study of its dependence on transition-metal element," *Journal of Physical Chemistry A*, vol. 123, 32, p. 7021, 2019.
- [19] N. Takagi, M. Ehara, and S. Sakaki, "Theoretical study of NO dissociative adsorption onto 3d metal particles M_{55} ($M = \text{Fe, Co, Ni, and Cu}$): Relation between the reactivity and position of the metal element in the periodic table," *ACS Omega*, vol. 6, 7, p. 4888, 2021.
- [20] J. Vekeman *et al.*, "Synergistic effects in the activity of nano-transition-metal clusters Pt_{12}M ($M = \text{Ir, Ru or Rh}$) for NO dissociation," *ChemPhysChem*, vol. 23, 21, e202200374, 2022.
- [21] H. Ooka, J. Huang, and K. S. Exner, "The Sabatier Principle in Electrocatalysis: Basics, limitations, and extensions," *Frontiers in Energy Research*, vol. 9, 2021.
- [22] J. Védrine, "Revisiting active sites in heterogeneous catalysis: Their structure and their dynamic behaviour," *Applied Catalysis A: General*, vol. 474, p. 40, 2014.
- [23] T. Campbell *et al.*, "Susceptibility of a heterogeneous catalyst, Rh/ γ -alumina, to rapid structural change by exposure to NO," *Chemical Communications*, p. 304, 4 2002.
- [24] M. Boronat and A. Corma, "Oxygen activation on gold nanoparticles: Separating the influence of particle size, particle shape and support interaction," *Dalton Transactions*, vol. 39, p. 8538, 2010.
- [25] A. Hakimioun *et al.*, "Theoretical investigation of the size effect on the oxygen adsorption energy of coinage metal nanoparticles," *Catalysis Letters*, vol. 151, p. 3165, 2021.
- [26] J. P. Chou, C. R. Hsing, C. M. Wei, C. Cheng, and C. M. Chang, "Ab initio random structure search for 13-atom clusters of fcc elements," *Journal of Physics: Condensed Matter*, vol. 25, no. 12, p. 125 305, 2013.
- [27] R. A. van Santen and I. Tranca, "Basic Quantum-Chemical concepts, the chemical bond revisited (jointly written with I. Tranca)," in *Modern Heterogeneous Catalysis*. John Wiley & Sons, Ltd, 2017, ch. 6, p. 173, ISBN: 9783527810253.
- [28] B. Hammer and J. K. Nørskov, "Theoretical surface science and catalysis—calculations and concepts," in *Impact of Surface Science on Catalysis*, ser. Advances in Catalysis, vol. 45, 2000, p. 71.
- [29] M.-S. Miao, J. A. Kurzman, N. Mammen, S. Narasimhan, and R. Seshadri, "Trends in the electronic structure of extended gold compounds: Implications for use of gold in heterogeneous catalysis," *Inorganic Chemistry*, vol. 51, no. 14, p. 7569, 2012.

- [30] G. J. Soldano, P. Quaino, E. Santos, and W. Schmickler, "Stability of gold and platinum nanowires on graphite edges," *ChemPhysChem*, vol. 11, no. 11, p. 2361,
- [31] R. Hoppe, "Effective coordination numbers (ECoN) and mean fictive ionic radii (MEFIR)," *Zeitschrift für Kristallographie – Crystalline Materials*, vol. 150, p. 23, 1979.
- [32] M. Piotrowski, P. Piquini, and J. Da Silva, "Density functional theory investigation of 3d, 4d, and 5d 13-atom metal clusters," *Physical Review B*, vol. 81, p. 155446, 2010.
- [33] N. N. Greenwood and A. Earnshaw, *Chemistry of the Elements 2nd Edition*: 1997, ISBN: 9780080379418.
- [34] M. Montemore, M. Spronsen, R. Madix, and C. Friend, "O₂ activation by metal surfaces: Implications for bonding and reactivity on heterogeneous catalysts," *Chemical Reviews*, vol. 118, 5, p. 2816, 2018.
- [35] E. Schulte, G. Belletti, M. Arce, and P. Quaino, "Oxygen reduction reaction (orr) on bimetallic AuPt and AuPd (1 0 0)-electrodes: Effects of the heteroatomic junction on the reaction paths," *Applied Surface Sciences*, vol. 441, p. 663, 2018.
- [36] F. Tielens, J. Andrés, M. Van Brussel, C. Buess-Hermann, and P. Geerlings, "DFT study of oxygen adsorption on modified nanostructured gold pyramids," *Journal of Physical Chemistry B*, vol. 109, no. 16, p. 7624, 2005.
- [37] *Experimental data for O₂ (Oxygen diatomic)*. CCCBDB-NIST. [Online]. Available: <https://cccbdb.nist.gov/exp2x.asp?casno=7782447&charge=0>.
- [38] B. Cordero *et al.*, "Covalent radii revisited," *Dalton Transactions*, no. 21, p. 2832, 2008.
- [39] J. Speight, *Lange's Handbook of Chemistry, 70th Anniversary Edition*, 16th ed. McGraw-Hill Professional, 2004, ISBN: 0071432205.
- [40] *Experimental data for N₂ (Nitrogen diatomic)*. CCCBDB-NIST. [Online]. Available: <https://cccbdb.nist.gov/exp2x.asp?casno=7727379>.
- [41] N. Lopez *et al.*, "On the origin of the catalytic activity of gold nanoparticles for low-temperature CO oxidation," *Journal of Catalysis*, vol. 223, 1, p. 223, 2004.
- [42] L. Barrio, P. Liu, J. A. Rodríguez, J. M. Campos-Martín, and J. L. G. Fierro, "A density functional theory study of the dissociation of H₂ on gold clusters: Importance of fluxionality and ensemble effects," *Journal of Chemical Physics*, vol. 125, p. 164715, 2006.
- [43] B. H. Morrow, D. E. Resasco, A. Striolo, and M. Buongiorno Nardelli, "CO adsorption on noble metal clusters: Local environment effects," *Journal of Physical Chemistry C*, vol. 115, 13, p. 5637, 2011.
- [44] A. Nabi, A. -ur-Rehman, A. Hussain, and D. Di Tommaso, "Ab initio random structure searching and catalytic properties of copper-based nanocluster with earth-abundant metals for the electrocatalytic CO₂-to-CO conversion," *Molecular Catalysis*, vol. 527, p. 112406, 2022.
- [45] F. Tielens and D. Bazin, "On the way of understanding the behavior of nanometer-scale metallic particles toward the adsorption of CO and NO molecules," *Comptes Rendus Chimie*, vol. 21, 3-4, p. 174, 2018.
- [46] Y. Zhang *et al.*, "Dual-metal sites boosting polarization of nitrogen molecules for efficient nitrogen photofixation," *Advanced Science*, vol. 8, 13, p. 2100302, 2021.
- [47] C. N. R. Rao and G. R. Rao, "Nature of nitrogen adsorbed on transition metal surfaces as revealed by electron spectroscopy and cognate techniques," *Surface Science Reports*, vol. 13, 7, p. 223, 1991.

- [48] I. Toyoshima and G. A. Somorjai, "Heats of chemisorption of O₂, H₂, CO, CO₂, and N₂ on polycrystalline and single crystal transition metal surfaces," *Catalysis Reviews*, vol. 19, 1, p. 105, 1979.
- [49] B. K. Das, A. Banerjee, A. Das, and K. K. Chattopadhyay, "Graphyne supported Co₁₃, Fe₁₃ and Ni₁₃ nano-cluster as efficient electrocatalysts for nitrogen reduction reaction: A first principles study," *Catalysis Today*, vol. 423, p. 113 906, 2023.
- [50] F. Montejo-Alvaro, J. Oliva, A. Zarate, M. Herrera-Trejo, H. Hdz-García, and A. I. Mtz-Enriquez, "Icosahedral transition metal clusters (M₁₃, M = Fe, Ni, and Cu) adsorbed on graphene quantum dots, a DFT study," *Physica E: Low-dimensional Systems and Nanostructures*, vol. 110, p. 52, 2019.
- [51] J. A. Martínez-Espinosa, H. Cruz-Martínez, P. Calaminici, and D. I. Medina, "Structures and properties of Co_{13-x}Cu_x (x = 0 – 13) nanoclusters and their interaction with pyridinic N₃-doped graphene nanoflake," *Physica E: Low-dimensional Systems and Nanostructures*, vol. 134, p. 114 858, 2021.
- [52] A. N. Sosa, J. E. Santana, A. Miranda, L. A. Pérez, R. Rurali, and M. Cruz-Irisson, "Transition metal-decorated germanene for NO, N₂ and O₂ sensing: A DFT study," *Surfaces and Interfaces*, vol. 30, p. 101 886, 2022.
- [53] W. Song *et al.*, "Density functional theory study of N₂ adsorption and dissociation on 3d transition metal atoms doped Ir(100) surface," *Applied Surface Science*, vol. 597, p. 153678, 2022.
- [54] M. Khalif *et al.*, "Adsorption of O₂ molecule on the transition metals (TM(II) = Sc²⁺, Ti²⁺, V²⁺, Cr²⁺, Mn²⁺, Fe²⁺, Co²⁺, Ni²⁺, Cu²⁺ and Zn²⁺) porphyrins induced carbon nanocone (TM(II)PCNC)," *Journal of Molecular Graphics and Modeling*, vol. 119, p. 108 362, 2023.
- [55] J. Yoon, H. Chang, S. Lee, and et al., "Selective nitrogen capture by porous hybrid materials containing accessible transition metal ion sites," *Nature Materials*, vol. 16, p. 526, 2017.
- [56] F. Tielens, J. Andrés, T. D. Chau, T. Visart de Bocarmé, N. Kruse, and P. Geerlings, "Molecular oxygen adsorption on electropositive nano gold tips," *Chemical Physics Letters*, vol. 421, 4-6, p. 433, 2006.
- [57] T. Visart de Bocarmé *et al.*, "Oxygen adsorption on gold nanofacets and model clusters," *Journal of Chemical Physics*, vol. 125, p. 054 703, 2006.
- [58] Y. Xu and M. Mavrikakis, "Adsorption and dissociation of O₂ on gold surfaces: Effect of steps and strain," *Journal of Physical Chemistry B*, vol. 107, 35, p. 9298, 2003.
- [59] M. Xue¹, J. Jia¹, and H. Wu, "Theoretical study of oxygen adsorption on a metal (Ni, Rh, Pd, Pt)-doped Au(111) surface," *International Journal of Electrochemical Science*, vol. 17, 7, p. 220 717, 2022.
- [60] J. K. Nørskov, F. Abild-Pedersen, F. Studt, and T. Bligaard, "Density functional theory in surface chemistry and catalysis," *Proceedings of the National Academy of Sciences*, vol. 108, no. 3, p. 937, 2011.
- [61] P. Quaino, F. Juarez, E. Santos, and S. W., "Volcano plots in hydrogen electrocatalysis – uses and abuses," *Beilstein Journal of Nanotechnology*, vol. 5, p. 846, 2014.
- [62] W. A. Brown and D. A. King, "NO chemisorption and reactions on metal surfaces: A new perspective," *Physical Chemistry B*, vol. 104, 12, p. 2578, 2000.

- [63] G. Brodén, T. N. Rhodin, and C. Brucker, "Synchrotron radiation study of chemisorptive bonding of CO on transition metals – Polarization effect on Ir(100)," *Surface Science*, vol. 59, 2, p. 593, 1976.
- [64] M. Okumura, Y. Kitagawa, M. Haruta, and K. Yamaguchi, "The interaction of neutral and charged Au clusters with O₂, CO and H₂," *Applied Catalysis A: General*, vol. 291, 1-2, p. 37, 2005.
- [65] A. Chmielewski *et al.*, "Reshaping dynamics of gold nanoparticles under H₂ and O₂ at atmospheric pressure," *ACS Nano*, vol. 13, 2, p. 2024, 2019.

Concluding remarks

In this thesis, computational methods were used to model and study surfaces of carbon nanotubes (CNT) and graphene oxide (GO) modified with platinum and iridium oxide nanoparticles. The study of such hybrid materials was developed by means of *ab-initio* DFT calculations, which allowed the acquisition of their optimized geometries, as well as the changes in their electronic properties and the energetic governing the interaction of the different components of the systems.

More specifically, periodic models corresponding to an *armchair* (5, 5) carbon nanotube and a graphene oxide surface were created using the available software. After geometry optimization, surface symmetry, electrostatic potential maps (EP) and Fermi softness analysis (FS) of the surfaces were instrumental in providing qualitative information on the potential anchoring configurations.

Different geometries of Pt_n ($n = 1 - 10, 13$) and $(\text{IrO}_2)_n$ ($n = 1 - 6$) systems were investigated next. In the one hand, the formation platinum nanoparticles was found to be thermodynamically favored, resulting in considerable differences with the *fcc* crystal structure in terms of energy, bond lengths, and coordination numbers. Furthermore, the analysis of EP and FS surfaces indicates that such Pt_n systems are more likely to form covalent bonds with substances that exhibit similar chemical properties. On the other hand, with regard to the iridium oxide nanoparticles, particular attention has been paid to the generation and characterization of the particle models—obtained by means of Genetic Algorithm (GA) methods—and the comparison with those found in literature. The results suggested that the formation of "core-shell-like" patterns (particles with interacting Ir atoms, and surrounded by Ir species) are preferred in such small oxide systems. Moreover, while the structures of the IrO_2 and Ir_2O_4 nanoparticles described here have been previously reported, the remaining Ir_3O_6 , Ir_4O_8 , Ir_5O_{10} and Ir_6O_{12} configurations are, to the best of our knowledge, introduced for the first time in this thesis. The analysis of platinum and iridium oxide particles was essential for further investigation of their interaction with carbon surfaces.

The analysis of the deposition of small Pt_n ($n = 1 - 10$) particles on the CNT surface revealed the most stable sites for Pt–CNT interaction. A comprehensive analysis has been conducted to elucidate the thermodynamic principles underlying nanoparticle adsorption. Particularly, a noteworthy stabilization effect of the nanoparticles at the carbon surface is observed. However, the stability gain is less evident with the increasing size. This can be attributed to the fact that the small diameter of the carbon nanotube imposes a limitation on the number of Pt atoms that can directly interact with the support, owing to structural incompatibility between the nanoparticle and the CNT.

The analysis of Pt_n/CNT systems was followed by a similar study of the deposition of iridium oxide nanoparticles, $(\text{IrO}_2)_n$ ($n = 1, 2, 3$), on the CNT surface. For this matter, structures derived from both rutile systems and Genetic Algorithm (GA) methods have been employed. Contrary to what was found for Pt clusters, the iridium oxide particles showed a weaker interaction with the pristine carbon surface. GA-derived clusters on the CNT exhibited exclusively physisorbed configurations. The reduced reactivity of the Ir atoms of the GA-derived particles toward covalent surfaces as that of the CNT can be justified by both their greater stability in gas-phase and their "core-shell-like" structures. Instead, the stabilization of such physisorbed states can be attributed to a charge polarization induced by the particle-surface interaction. On the other hand, covalent Ir-C bonding resulted from the interaction of the IrO_2 monomer and the rutile-derived $(\text{IrO}_2)_3$ particle with the CNT. These findings correlate well with the regions of reactive electronic orbitals obtained by means of FS analysis. It is worth noting, however, that larger iridium oxide particles do not seem to improve their stability on the carbon nanotube surface, as in the case of the Pt_n clusters. This can be considered of practical interest, considering that small-sized supporting materials such as the (5, 5)-CNTs could be carrying platinum or iridium oxide particles at the nanoscale, thus reducing the amount of precious catalyst used.

Considering that GA-derived iridium oxide nanoparticles could better interact with a polar surface, their deposition on a GO surface was also studied. As a result of the research, the most stable adsorption configurations of $(\text{IrO}_2)_n$ ($n = 1 - 6$) on the graphene oxide surface have been determined. In all cases, the formation of a new Ir-O bond was found to proceed via the rupture of an "epoxy" oxygen of GO, irrespective of the particle size.

To continue with, the catalytic capabilities of selected Pt_n/CNT and $(\text{IrO}_2)_n/\text{CNT}$ materials have been evaluated by using key test reactions, namely water adsorption and further dissociation pathways. For the evaluated Pt_n/CNT systems, the platinum-surface interface presented a notable impact on the kinetics of the water dissociation, leading to lower activation energies with respect to the pristine Pt(111) surface. This phenomenon can be attributed to the polarization of metal particles resulting from their interaction with the carbon surface. In the case of the $(\text{IrO}_2)_n/\text{CNT}$ materials, very low energy barriers were also found for the water dissociation on the rutile-derived deposited particles. The intrinsic charge polarization of iridium oxide has been suggested to be a key factor in favoring this process within such systems.

The final chapter of the thesis includes a thorough examination of the adsorption of O_2 and N_2 molecules on monometallic transition metal nanoclusters. Overall, the findings suggest that the adsorption of O_2 on the nanoparticles could be up to 2.3 eV more stable than the adsorption of the N_2 molecule, with important differences found for the first elements considered in each period, which may be important in terms of molecule selectivity. In addition, the study also identifies potential catalysts for the dissociation of oxygen and nitrogen, such as Pd, Pt, and Os for O_2 , and Os for N_2 . This part of the work establishes a preliminary foundation for further study of O_2 and N_2 dissociation on such metallic nanoclusters, both in a vacuum and supported on carbon surfaces.

Annexes

A.I Molecular adsorption of O₂ and N₂ on M₁₃: energies and bond lenght values

Z	M	$E_{\text{ads O}_2}/\text{eV}$					O ₂ bond lenght/Å				
		e/tp	s/tp	e/hw	s/hw	br	e/tp	s/tp	e/hw	s/hw	br
47	Ag	-0.32	-0.30	-0.38	-0.91	-0.83	1.29	1.35	1.32	1.44	1.37
79	Au	-0.39	-0.26		-0.02	-0.62	1.29	1.35		1.35	1.38
27	Co	-1.57	-2.20				1.30	1.39			
29	Cu	-0.75	-1.05	-0.67	-1.96	-1.37	1.29	1.40	1.35	1.55	1.49
26	Fe	-1.91	-2.61				1.29	1.44			
77	Ir	-1.68	-2.32			-2.15	1.30	1.42			1.49
28	Ni	-1.35	-1.68		-2.07		1.28	1.38		1.61	
76	Os	-2.39	-2.98	-0.15			1.29	1.47	1.34		
46	Pd	-0.74	-0.63	0.00	-0.59	-1.39	1.28	1.34	1.30	1.40	1.36
78	Pt	-0.80	-0.87	0.03		-1.67	1.29	1.38	1.27		1.42
45	Rh	-1.25	-1.73	-0.38		-2.70	1.29	1.38	1.32		1.43
44	Ru	-2.08	-2.57	-0.95	-2.70	-2.96	1.29	1.43	1.34	1.70	1.55

Table A.1: Adsorption energies and molecular bond lengths for O₂ on M₁₃.

Z	M	$E_{\text{ads N}_2}/\text{eV}$					N ₂ bond lenght/ \AA				
		e/tp	s/tp	e/hw	s/hw	br	e/tp	s/tp	e/hw	s/hw	br
47	Ag	-0.19					1.12				
79	Au	-0.34				-0.34	1.12				1.12
27	Co	-1.17	-0.62	-0.22	-0.39	-0.96	1.14	1.17	1.17	1.25	1.20
29	Cu	-0.71	-0.19			-0.35	1.13	1.14			1.15
26	Fe	-1.15	-0.72	-0.49	-0.70	-1.08	1.14	1.18	1.16	1.32	1.20
77	Ir	-1.56	-0.79			-1.18	1.14	1.18			1.21
28	Ni	-1.28	-0.75	-0.37	-0.28	-1.18	1.14	1.16	1.17	1.19	1.18
76	Os	-1.53	-0.90			-1.27	1.14	1.20			1.24
46	Pd	-0.65				-0.68	1.13				1.16
78	Pt	-0.91	-0.37			-0.43	1.13	1.15			1.17
45	Rh	-1.10	-0.49	-0.05		-1.04	1.14	1.16	1.17		1.18
44	Ru	-1.22	-0.77	-0.09	-0.29	-1.18	1.14	1.18	1.17	1.24	1.20

Table A.2: Adsorption energies and molecular bond lengths for N₂ on M₁₃.

A.II Hubbard correction on Ir-related systems

Linear response

Following the work of Cococcioni & Girancoli [1] and procedures that are specific to VASP software [2], a linear response approach to the determination of a proper Hubbard's U parameter for iridate compounds has been carried out. In short, the U parameter for the DFT+ U treatment of Ir- d electrons can be estimated by

$$U = \chi^{-1} - \chi_0^{-1} \quad (11)$$

where

$$\chi = \frac{\partial N^{\text{SCF}}}{\partial \alpha}, \quad \chi_0 = \frac{\partial N^{\text{NSCF}}}{\partial \alpha}. \quad (12)$$

The quantity N represents the population of d electrons of a single Ir site following an electronic self-consistent (SCF) and non-self-consistent (NSCF) calculations. In addition, α is the spherical potential added on the Ir site, quantifying the effective on-site Coulomb interaction of d -states.

To start with, and in order to obtain information which would be comparable with existing literature, this procedure has been applied to a rutile IrO₂ bulk¹. Fig. A.27 presents the results of the SCF and NSCF calculations for α values between -0.20 and 0.20 eV. Linear regressions have been performed with the outputs of both types of calculations, and the corresponding results are presented in eqs. 14 and 13.

$$N^{\text{NSCF}} = 0.93467\alpha + 6.86787, \quad R^2 = 0.99957, \quad (13)$$

$$N^{\text{SCF}} = 0.33700\alpha + 6.87215, \quad R^2 = 0.99991. \quad (14)$$

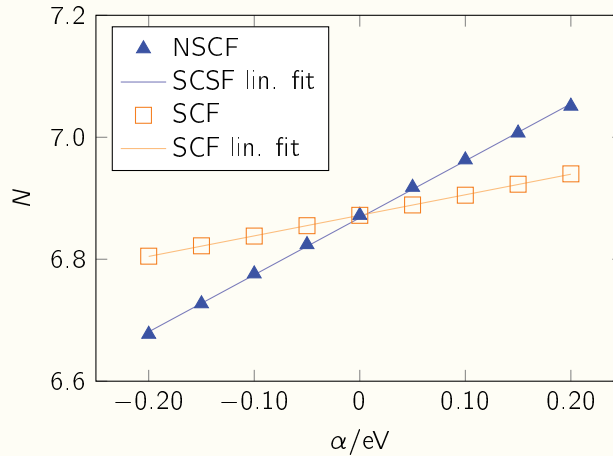


Figure A.27: Populations of d -states (N) for both SCF and NSCF calculations, as a function of the potential representing the Coulomb interaction (α). Linear fits for each group are also included.

The slope of both linear regressions can be introduced in eq. 11 to estimate the value of U for this

¹($2 \times 2 \times 2$) supercell ($a = b = 9.02979$ Å, $c = 6.33684$ Å), and a ($3 \times 3 \times 3$) grid of k -points.

system:

$$U = \left(\frac{\partial N^{\text{SCF}}}{\partial \alpha} \right)^{-1} - \left(\frac{\partial N^{\text{NSCF}}}{\partial \alpha} \right)^{-1} = \frac{1}{0.33700 \text{ eV}^{-1}} - \frac{1}{0.93647 \text{ eV}^{-1}} = 1.89746 \text{ eV}. \quad (15)$$

This result is very close to the 2 eV value reportedly used to model bulks and surfaces of iridium oxide-related materials [3, 4].

A similar procedure has been applied to all Ir sites of the $(\text{IrO}_2)_6$ nanoparticle structure derived from GA (see chapter 5). Table A.3 lists the estimated U values for each species following the above methodology. As a result, a smaller U correction, compared with the rutile IrO_2 bulk, in the range of 0.7 to 1.8 eV should be adequate for such nanostructures.

Ir site	Estimated U/eV
Ir ¹	1.74593
Ir ²	0.67665
Ir ³	0.67832
Ir ⁴	0.96877
Ir ⁵	1.59113
Ir ⁶	0.96494

Table A.3: Hubbard's U estimated values using linear regression approach for the $(\text{IrO}_2)_6^{\text{GA}}$ nanoparticle. Linear regression coefficients R^2 were greater than 0.999 in all cases.

Relative energies

Having into consideration the U values estimated in the above section for both nanoparticles and bulk systems, their impact on relative energies representing the adsorption processes is evaluated next.

For this matter, the most stable adsorptions modes of $(\text{IrO}_2)_2^{\text{GA}}$ and $(\text{IrO}_2)_6^{\text{GA}}$ nanoparticles on a graphene oxide surface (see chapter 8) were chosen as model systems. Particle-surface interaction energies were computed according to eq. 8.1, including different U values in the Ir site in direct contact with the surface. Table A.4 lists the resulting interaction energies for each U , from which it can be observed that no notable differences arouse in these systems from the variation of U between 0 and 4 eV.

U/eV	$(\text{IrO}_2)_2/\text{GO}$		$(\text{IrO}_2)_6/\text{GO}$	
	mag/ μ_B	E_{int}/eV	mag/ μ_B	E_{int}/eV
0	2.0	−0.14	2.1	−0.30
2	2.0	−0.14	2.1	−0.31
4	2.0	−0.15	2.2	−0.33
6	3.8	+0.49	2.6	−0.37

Table A.4: Variation of total magnetization (mag) and particle-surface interaction energy (E_{int}) for the most stable $(\text{IrO}_2)_2/\text{GO}$ and $(\text{IrO}_2)_6/\text{GO}$ adsorption modes.

Comparison with HSE06 functional

In addition, projected densities of electronic states (PDOS) corresponding to the d -electrons of a $(\text{IrO}_2)_6^{\text{GA}}$ model system have been obtained with both DFT+ U and HSE06 hybrid functional approximations, the latter being considered among the best available methods to compute electronic properties of materials [5]. The results are shown in Fig. A.28, where it is possible to observe that the different U values are unable to properly reproduce the band-gap (and the electronic distribution, in general terms) predicted with the HSE06 functional.

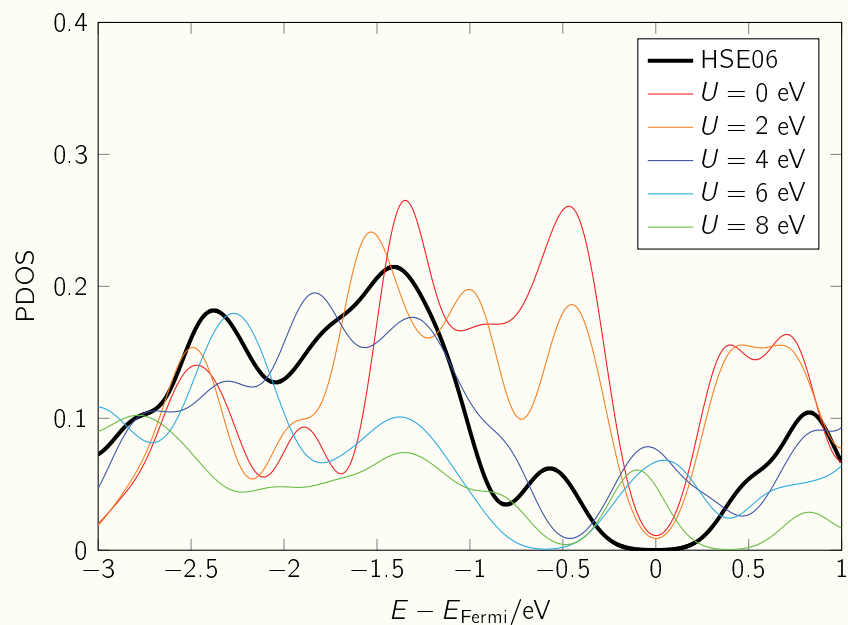


Figure A.28: PDOS of Ir- d states from $(\text{IrO}_2)_6^{\text{GA}}$ nanoparticles, computed by using HSE06 and DFT+ U approximations.

References for Annexes

- [1] M. Cococcioni and S. De Gironcoli, "Linear response approach to the calculation of the effective interaction parameters in the LDA+U method," *Physical Review B*, vol. 71, no. 3, p. 035 105, 2005.
- [2] [Online]. Available: https://www.vasp.at/wiki/index.php/Calculate_U_for_LSDA%2B.
- [3] S. K. Panda, S. Bhowal, A. Delin, O. Eriksson, and I. Dasgupta, "Effect of spin orbit coupling and Hubbard U on the electronic structure of IrO_2 ," *Physical Review B*, vol. 89, p. 155 102, 15 2014.
- [4] X. Ming, K. Yamauchi, T. Oguchi, and S. Picozzi, "Metal–insulator transition and $J_{\text{eff}}=1/2$ spin–orbit insulating state in rutile–based $\text{IrO}_2/\text{TiO}_2$ superlattices," *arXiv:1702.04408 [cond-mat.str-el]*, 2017.
- [5] P. Borlido, T. Aull, A. W. Huran, F. Tran, M. A. Marques, and S. Botti, "Large-scale benchmark of exchange–correlation functionals for the determination of electronic band gaps of solids," *Journal of Chemical Theory and Computation*, vol. 15, no. 9, p. 5069, 2019.